DETECTION AND ESTIMATION IN QUANTUM ILLUMINATION

DETECTION AND ESTIMATION IN QUANTUM ILLUMINATION

By JINGXIN WANG, M.Sc

A Thesis Submitted to the School of Graduate Studies in Partial Fulfillment of the Requirements for the Degree Doctor of Philosophy

McMaster University

DOCTOR OF PHILOSOPHY (2024)

Hamilton, Ontario, Canada (Electrical and Computer Engineering)

TITLE:	Detection and Estimation in Quantum Illumination
AUTHOR:	Jingxin Wang Master of Science (Electrical and Computer Engineering), Bristol University, Bristol, UK
SUPERVISOR:	Dr. Kon Max Wong
NUMBER OF PAGES:	xix, 192

Lay Abstract

Quantum radar systems as extensions to classical radar systems employ certain quantum phenomena to improve the target detection and parameter estimation performance. This thesis studies the quantum illumination system that exploits the quantum entanglement (correlation). This thesis provides descriptions of the detection and estimation problems in a quantum system. For the detection section, the upper bound on the probability of error in determining the presence or absence of a target is shown. Two practically implementable detection methods in quantum illumination systems are proposed and numerically analyzed. This thesis also contributes to the quantum estimation problems by firstly analyzing the accuracy limit in the simultaneous estimation of two system parameters. Finally, we develop solutions of the two-parameter estimation problem.

Abstract

Quantum radar exploits the properties of quantum entanglement to enhance its performance over classical radar. Quantum illumination, being one special type of quantum radar, generates a pair of highly entangled beams called the *signal* and *idler* beams, transmits the signal beam for target exploration, and examines the returned signal beam using the quantum entanglement to improve the target detection and estimation performance.

In this thesis, the role of the optical parametric amplifier (OPA) in target detection of the QI system is first studied. We propose a dual-OPA design of the detector so that an optimum combination of intensities of inputs can be achieved, yielding a marked improvement in the detector performance. The information of the entanglement contained in the covariance matrix (CM) between the returned signal and idler beams is then considered. Here, we propose a technique that exploits the entanglement to a higher degree. This detection method employs the metric of Riemannian distances (RD) between the reconstructed CMs as the test statistic to assess the probabilities of "target" or "no target". Numerical experiments confirm that the CM detector is far superior in detection performance to the OPA detectors.

We then turn our attention to the study of multi-parameter estimation problem in QI. Here, we focus our consideration on the simultaneous estimation of the target range and target velocity the information of which is embedded in the arrival time and frequency of the returned signal. The Quantum Cramer-Rao bound (QCRB) for the estimation of such parameters of the signal photon propagated through a random environment is derived. To facilitate the simultaneous estimation of the two parameters, we propose two methods. The first is a modified application of the classical ambiguity function in classical radar systems to the QI system. Analysis shows direct application of the classical ambiguity function may lead to multiple estimates of the desired parameters. Thus, we try to reconstruct the temporal wavefunctions of the returned signal and idler photons using interferometric measurement. The correlation of the wavefunctions with the reference signal at different time delays provides an estimate of the average arrival time of the return signal. In addition, the phase slopes yield an estimate of the central frequencies, thus completing the joint estimation of the two parameters. Seeing that the reconstruction of the wavefuctions requires a large amount of measurement data, we develop a second estimation method which applies a unitary operator at one end, and its inverse at the other end, of the QI system. The re-entangled returned signal beam and the idler beam both contain information of the two parameters and their estimation is carried out by measurements on the signal beam and on the idler beam respectively. Numerical experiments verify the validity and accuracy of these methods.

This thesis is dedicated to the people who have supported me throughout my education.

Thanks for making me see this adventure through to this end.

Acknowledgements

I would like to acknowledge and give my warmest thanks to my supervisor, Dr. Kon Max Wong, who made this work possible. His patient guidance and valuable advice carried me through all the stages of writing my project. And he generously provided knowledge and expertise throughout my entire research journey. Additionally, this endeavor would not have been possible without the generous support from Dr. Kon Max Wong, who financed my research.

I am also grateful to my committee members, Dr. Xun Li, Dr. Jun Chen and Dr. Tim Davidson for their support throughout my study.

Lastly, I would be remiss in not mentioning my parents and sister. Their belief in me has kept my spirits and motivation high during this process. I would also like to thank my cat, Niuniu, for all the entertainment and emotional support.

Table of Contents

List of Figures

List of Tables

Abbreviations

CI	Classical Illumination
OPA	Optical Parametric Amplifier
QCB	Quantum Chernoff Bound
QCRB	Quantum Cramer-Rao Bound
QI	Quantum Illumination
SLD	Symmetric Logarithmic Derivative
SPDC	Spontaneous Parametric Down Conversion

Chapter 1

Introduction

In a conventional radar system [1], an electromagnetic pulse signal is transmitted towards a region, and, from the returned signal, the radar receiver performs the analysis for the purpose of detection (deciding whether a target is present) and parameter (e.g. target range, velocity) estimation. In comparison to classical radar systems, *quantum radars* [2]–[6] exploit certain quantum phenomena to enhance the performance of such functions.

In particular, in this thesis, our interest is centered around *quantum illumination* (QI) [2], [7]–[13], which is a technology used in quantum radars to improve target detection, especially in a lossy and noisy environment, utilizing the phenomenon of *quantum entanglement* [14]–[20].

Proposed by Lloyd [7] in 2008, and later extended to a Gaussian-state scenario in [8], [9], the idea of QI is to generate two beams of entangled photons, called the *signal*

and the *idler* beams respectively. While the signal beam is transmitted to detect the possible target in the interested region, the idler beam is saved in the radar system for a joint measurement with the received signal. Using such a technique, the joint measurement on the entangled beams may well enhance the radar performance. Indeed, Tan et. al. [8] showed that using a series of identical maximally entangled Gaussian states obtained from the continuous wave (cw) *spontaneous parametric down conversion* (SPDC) [14], a theoretical advantage of 6 dB in the detection error exponent (*quantum Chernoff bound* (QCB)) can be achieved over the classical illumination (CI) scheme employing coherent beams.

There are few studies on quantum detectors for QI which can outperform CI. Guha and Erkma [9] proposed the *optical parametric amplifier* (OPA) and the *phase conjugate* (PC) receivers. Both these methods relied on *photon counting* and can achieve 3 dB improvement in the error exponent compared with that of CI. Both OPA and PC detectors have been successfully demonstrated [16], [19] in both the optical and microwave frequency ranges. A scheme of *feed-forward sum-frequency generation* (FF-SFG) [17] has been proposed and could asymptotically approach the 6 dB enhancement. However, this design has not been verified due to the complexity of implementation.

In this thesis, we firstly address the detection problem of quantum illumination in a quantum radar. We re-examine the OPA detector by giving it a more comprehensive analysis, and propose a detector using two OPAs which facilitates the optimization of its gains, yielding an improved performance. We further propose a quantum detector which capitalizes on the structure of the returned signal covariance matrix (CM),

thus exploiting the multi-dimensional information on the returned beam. We show how these parameters of the CM can be measured from the returned signal, and we introduce the *Riemannian distance* and its weighted version [21], [22] between CMs as a detection metric. Numerical experiments show that such a method lowers the probability of detection error to below the QCB, and substantially enhances the detection performance of the receiver.

The quantum illumination system also improves the accuracy of the parameter estimation due to the quantum entanglement. [23] derived the *quantum Cramer-Rao bound* (QCRB) of the simultaneous estimation of time and frequency that is smaller than corresponding Cramer-Rao bound in classical systems. Moreover, they proposed the estimation method that used the *Symmetric Logarithmic Operator* (SLD) on the returned signal and idler beams. However, the practical implementation of the SLD operators still remains as a problem to be solved. In this thesis, two estimation methods are proposed. One relies on the wavefunction reconstruction of the return signal and idler beams, including both the reconstruction of the amplitude and phase of the wavefunction. The second method introduces the unitary operator that is applied on both the generated SPDC pair and the received signal pair. Numerical results of these two estimation methods are included and analysed.

The thesis consists of the following chapters:

Chapter 2: Quantum Entanglement and Quantum Radar. This chapter introduces the notations and fundamental concepts of quantum mechanics required for understanding of the remainder of this thesis. The concept of quantum entanglement is introduced.

Chapter 3: Quantum Radar. This chapter shows the advantages of quantum radar systems and describes different categories of quantum radar systems. The development of quantum illumination is included from the discrete quantum illumination to the continuous quantum illumination. This chapter also describes the experimental realization of quantum illumination systems.

Chapter 4: Quantum Detection Methods in QI. This chapter extends classical detection problems to quantum detection problems firstly. Then, the corresponding Quantum Chernoff bound is introduced and derived for QI systems. This section includes the description of two detection methods, *dual-OPA* detection design and the *CM* detectors as well as their numerical results.

Chapter 5: Quantum Estimation in QI. This chapter provides an introduction to the quantum estimation, which includes the statement of quantum estimation problems in radar systems and the Quantum Cramer-Rao bound. The estimation method using the ambiguity function based on the wavefunction reconstruction is proposed with numerical results. The second joint estimation method using the unitary transformation is described with numerical results.

Chapter 2

Quantum Entanglement and Quantum Radar

Explanation of Basic Notations

The notation throughout this thesis employs the *bra* and *ket* notation developed by P.A.M. Dirac [24], which is different from the notation typically used in engineering. In quantum mechanics, the *state* of a system is described by a ket vector in the form $|x\rangle$. $|x\rangle$ is a complex-valued column vector mathematically whose dimension depends on the chosen basis representation. This state ket is postulated to contain complete information about the physical state. The transpose and complex conjugate of the ket vector gives its corresponding bra vector, $\langle x|$.

The *quantum operator* that acts on a particular state is represented by the notation, $\hat{\mathbf{A}}$, which mathematically takes a form of a matrix.

2.1 Basics of Quantum Systems

2.1.1 Bosonic/Quadrature Operators

A *quantum mechanical system* can be described by its Hamiltonian as defined as [25]

$$\hat{\mathbf{H}} = \hbar\omega(\hat{\mathbf{a}}^\dagger\hat{\mathbf{a}} + \frac{1}{2}\hat{\mathbf{I}}) \tag{2.1}$$

where $\hat{\mathbf{a}}$ and $\hat{\mathbf{a}}^\dagger$ represent the *annihilation* and *creation operators* respectively. Here, † representing the Hermitian conjugate transpose. $\hbar$ is the Planck's constant and ω is the angular frequency, thus $\hbar\omega$ represents the single-photon quantisation energy, and $\hat{\mathbf{n}} \triangleq \hat{\mathbf{a}}^\dagger\hat{\mathbf{a}}$ is the *photon number* operator, and the additional 1/2 arises from the zero-point energy fluctuations associated with the vacuum. The state of the system, represented by the density operator, $\boldsymbol{\rho}$, resides in a separable, infinite-dimensional space $\mathcal{H}$ spanned by the Fock number basis $\{|n\rangle\}_{n=0}^{\infty}$ also called *the number state representation*. The space spanned by $\{|n\rangle\}_{n=0}^{\infty}$ is called the *Fock space*. The basic state $|1\rangle$ represents the Hilbert space of one photon number $\mathcal{H}_1$. Correspondingly, $|2\rangle$ describes the joint state of two photons, which lie on the symmetric tensor product of two Hilbert spaces $\mathcal{H}_2 = \mathcal{H}_1 \otimes_s \mathcal{H}_1$. Then, it can be deduced that $|n\rangle$ represents the presence of n photons in the interested mode and lies in the Hilbert space $\mathcal{H}_n = \mathcal{H}_1 \otimes_s (\mathcal{H}_1 \otimes_s (\mathcal{H}_1 \cdots))$. The Fock space is defined as $\mathcal{H}_1 \oplus \mathcal{H}_2 \oplus \cdots \oplus \mathcal{H}_n \oplus \cdots$.

The set of number states, $\{|n\rangle\}_{n=0}^{\infty}$ are associated by bosonic annihilation and creation

operators, defined by

$$\hat{\mathbf{a}}\,|0\rangle = 0\,|0\rangle\,, \quad \hat{\mathbf{a}}\,|n\rangle = \sqrt{n}\,|n-1\rangle\,, \quad \hat{\mathbf{a}}^{\dagger}\,|n\rangle = \sqrt{n+1}\,|n+1\rangle \tag{2.2}$$

These definitions illustrate exactly how two operators act on the system: an annihilation operator removes one photon while a creation operator adds one. Creation and annihilation operators of a single-mode system obey the usual bosonic commutation relation, namely

$$[\hat{\mathbf{a}}, \hat{\mathbf{a}}^{\dagger}] = \hat{\mathbf{a}}\hat{\mathbf{a}}^{\dagger} - \hat{\mathbf{a}}^{\dagger}\hat{\mathbf{a}} = \hat{\mathbf{I}} \tag{2.3}$$

A *single-mode system* or *mode* refers to one system whose properties are single-valued. The concerned properties can be single or multiple. For example, if only the frequency of the system is concerned, the system with one frequency is said to be a single-mode system. Then, if the bandwidth of the system includes more than one frequency, the system becomes *multi-mode*. The number of frequencies included determines the number of modes of this system. This single-mode formalism can be extended to describe an N-mode bosonic system residing in the Hilbert space $\mathcal{H}^{\otimes N} = \otimes_{k=1}^{N}\mathcal{H}_{sk}$. This Hilbert space of the N-mode bosonic system is a tensor product of the individual Fock spaces $\{\mathcal{H}_{sk}\}_{k=1}^{N}$ of constituent, non-interacting modes with corresponding bosonic operators given by the set $\{\hat{\mathbf{a}}_k, \hat{\mathbf{a}}_k^{\dagger}\}_{k=1}^{N}$. Other properties such as time or phase of the system can be used to define the number of modes.

The canonical operators of a one-mode system form a vector: $\hat{\mathbf{x}} = (\hat{\mathbf{a}}, \hat{\mathbf{a}}^{\dagger})^T$. Following

the commutation relation in Eq.2.3, the commutation relations of the vector $\hat{\mathbf{x}}$ is[1]

$$[\hat{\mathbf{x}}_m, \hat{\mathbf{x}}_n] \triangleq \omega_{mn}\hat{\mathbf{I}}, \quad m, n = 1, 2 \tag{2.4}$$

where $\hat{\mathbf{x}}_{m/n}$ refers to the $m^{\text{th}}/n^{\text{th}}$ element in $\hat{\mathbf{x}}$. ω_{mn} is the mn^{th} element of the matrix, $\boldsymbol{\omega}$ which is

$$\boldsymbol{\omega} = \begin{bmatrix} 0 & 1 \\ -1 & 0 \end{bmatrix} \tag{2.5}$$

Within this multi-mode setting, all these field operators can be arranged into a single vectorial form $\hat{\mathbf{x}} \triangleq (\hat{\mathbf{a}}_1, \hat{\mathbf{a}}_1^\dagger, ..., \hat{\mathbf{a}}_N, \hat{\mathbf{a}}_N^\dagger)^T$, satisfying the same bosonic commutation relations

$$[\hat{\mathbf{x}}_m, \hat{\mathbf{x}}_n] = \Omega_{mn}\hat{\mathbf{I}}, m, n = 1, ..., 2N \tag{2.6}$$

where Ω_{mn} is an element within the $2N \times 2N$ matrix, $\boldsymbol{\Omega}$, known as the symplectic form, given by the direct sum of N identical 2×2 blocks $\boldsymbol{\omega}$

$$\boldsymbol{\Omega} \triangleq \bigoplus_{k=1}^{N} \boldsymbol{\omega} = \text{diag}(\boldsymbol{\omega}, ..., \boldsymbol{\omega}) \tag{2.7}$$

The *phase-space quadrature operators* $\{\hat{\mathbf{x}}_k, \hat{\mathbf{p}}_k\}_{k=1}^N$ of an N-mode quantum system can be defined in terms of corresponding creation and annihilation operators as

$$\hat{\mathbf{x}}_k = \frac{\hat{\mathbf{a}}_k + \hat{\mathbf{a}}_k^\dagger}{\sqrt{2}}, \quad \hat{\mathbf{p}}_k = -\frac{i(\hat{\mathbf{a}}_k - \hat{\mathbf{a}}_k^\dagger)}{\sqrt{2}} \tag{2.8}$$

Similarly, all quadrature operators can be arranged into a vector: $\hat{\mathbf{y}} \triangleq (\hat{\mathbf{x}}_1, \hat{\mathbf{p}}_1, ..., \hat{\mathbf{x}}_N, \hat{\mathbf{p}}_N)^T$

[1] Many authors write Eq. (2.4) as $[\hat{\mathbf{x}}_m, \hat{\mathbf{x}}_n] = \omega_{mn}$ which, strictly speaking, is an abuse of notation. What they really mean (cf. Eq. (2.12)) is $\langle[\hat{\mathbf{x}}_m, \hat{\mathbf{x}}_n]\rangle \triangleq \text{tr}(\boldsymbol{\rho}[\hat{\mathbf{x}}_m, \hat{\mathbf{x}}_n]) = \omega_{mn}$.

and the commutation relation in Eq.2.6 becomes $\langle[\hat{\mathbf{y}}_i, \hat{\mathbf{y}}_j]\rangle = i\boldsymbol{\Omega}_{ij}$.

2.1.2 Pure and Mixed States

The quantum state of a single-mode system contains all of its physical information and is presented by the *density operator*, $\boldsymbol{\rho}$. This is a positive operator with unity trace, i.e., $\mathrm{tr}(\boldsymbol{\rho}) = 1$. Mathematically, the density operator $\boldsymbol{\rho}$ is represented as a matrix and hence, it is also called as a density matrix. A quantum system is in a *pure state* if its density operator can be written as $\boldsymbol{\rho} = |x\rangle \langle x|$, where $|x\rangle$ represents one possible state of the quantum system. If the density operator is written as a probabilistic mixture of more than one density operators as $\boldsymbol{\rho} = \sum_n P_n \boldsymbol{\rho}_n$, it is called a *mixed state*. P_n denotes the probability of being in the state $|x_n\rangle$ with $\boldsymbol{\rho}_n = |x_n\rangle \langle x_n|$. To maintain $\mathrm{tr}(\boldsymbol{\rho}) = 1$, $\sum_n P_n = 1$.

2.1.3 State Wavefunction and Gaussian States

The density operator $\boldsymbol{\rho}$ of an N-mode system in the Hilbert space has an equivalent representation in terms of the Wigner distribution over a real phase space.

The Weyl operator, which provides us with a mapping between the Hilbert space and the phase space is

$$\hat{\mathbf{D}}_{\mathrm{w}}(\boldsymbol{\xi}) \triangleq \exp(i\hat{\mathbf{y}}^T \boldsymbol{\Omega} \boldsymbol{\xi}) \tag{2.9}$$

where $\boldsymbol{\xi} \in \mathcal{R}^{2N}$. $\hat{\mathbf{y}}$ is the vector consisting of quadrature operators of N modes. $\boldsymbol{\Omega}$ is defined in Eq.2.7.

The Weyl operator is applied on the density operator $\boldsymbol{\rho}$ and its expected output gives the Wigner characteristic function, $\chi(\boldsymbol{\xi})$ as

$$\chi(\boldsymbol{\xi}) \triangleq \mathrm{tr}[\boldsymbol{\rho}\hat{\mathbf{D}}_{\mathrm{w}}(\boldsymbol{\xi})] \tag{2.10}$$

Thus, the density operator $\boldsymbol{\rho}$ can always be expressed in terms of the Fourier transform of the characteristic function, giving the Wigner function $W_{\mathrm{wg}}(\mathbf{y})$.

$$W_{\mathrm{wg}}(\mathbf{y}) = \frac{1}{(2\pi)^{2N}} \int_{\mathbb{R}^{2N}} \exp(-i\mathbf{y}^T \boldsymbol{\Omega}\boldsymbol{\xi})\chi(\boldsymbol{\xi}) d^{2N}\boldsymbol{\xi} \tag{2.11}$$

defined on the symplectic phase space $\mathcal{K} := (\mathbb{R}^{2N}, \boldsymbol{\Omega})$, spanned by the real, continuous variable, $\mathbf{y} = (x_1, p_1, ..., x_N, p_N)$. This is referred to as the quadrature coordinates of any quantum state in the phase space. For example, x_1 is the coordinate corresponding to the quadrature operator $\hat{\mathbf{x}}_1 \triangleq \int x_1 \left|x_1\right\rangle \left\langle x_1\right| dx_1$. Applying this operator $\hat{\mathbf{x}}_1$ gives the mean value of x_1 of the system state $\boldsymbol{\rho}$.

In the Wigner distribution of quantum states, the first two statistical moments of the quantum states, ($\bar{\mathbf{y}}$, $\boldsymbol{\Gamma}$), are the most important quantities. The first moment, $\bar{\mathbf{y}}$, is the displacement vector or mean value whose ith element is given as

$$\bar{y_i} \triangleq \langle \hat{\mathbf{y}}_i \rangle = \mathrm{tr}[\boldsymbol{\rho}\hat{\mathbf{y}}_i] \tag{2.12}$$

where $\langle \hat{\mathbf{y}}_i \rangle$ represents the expected measurement result of the operator $\hat{\mathbf{y}}_i$ on the system operator $\boldsymbol{\rho}$. $\hat{\mathbf{y}}_i$ refers to the ith operator in $\hat{\mathbf{y}}$. This result is given by the trace of the product of the quadrature operator and the system density operator.

The second moment is the covariance of quadrature operators as given by the covariance matrix (CM), $\mathbf{\Gamma}$ whose ijth element is given by

$$\Gamma_{ij} \triangleq \frac{1}{2}\mathrm{tr}[\{\hat{\mathbf{y}}_i - \bar{y}_i\mathbf{I}, \hat{\mathbf{y}}_j - \bar{y}_j\mathbf{I}\}\boldsymbol{\rho}], \quad i,j = 1,...,2N \tag{2.13}$$

where $\{,\}$ is the anticommutator: $\{\hat{\mathbf{y}}_i, \hat{\mathbf{y}}_j\} = \hat{\mathbf{y}}_i\hat{\mathbf{y}}_j + \hat{\mathbf{y}}_j\hat{\mathbf{y}}_i$. Any CM should always be semi-positive definite and symmetric: $\mathbf{\Gamma} \geq \mathbf{0}$. This implies that all eigenvalues of $\mathbf{\Gamma}$ are equal to or larger to 0. The covariance matrix of any physical state must also obey the following uncertainty relationship [26]

$$\mathbf{\Gamma} + i\mathbf{\Omega} \geq \mathbf{0} \tag{2.14}$$

Therefore, the covariance matrix of any physical state must be positive-definite such that $\mathbf{\Gamma} > \mathbf{0}$.

2.1.4 Gaussian States

The quantum Gaussian state is one special type of quantum states, which can be fully described by its first and second moments. This is also the focus of this thesis. A Gaussian state is, in general, denoted as $\boldsymbol{\rho}(\bar{y}, \mathbf{\Gamma})$. Moreover, its corresponding wave function takes a form of Gaussian distribution.

Examples of Gaussian states

There are three most common Gaussian states:

- **Vacuum State**

  The vacuum state, denoted as $|0\rangle$ with its density operator $\boldsymbol{\rho}_{\text{vac}} = |0\rangle\langle 0|$, is the eigenstate of the number operator $\hat{\mathbf{n}}$ with eigenvalue 0: $\hat{\mathbf{n}}|0\rangle = 0|0\rangle$. Its mean vector is $\bar{\mathbf{y}} = (0,0)^T$ and CM is

$$\boldsymbol{\Gamma} = \begin{bmatrix} 1 & 0 \\ 0 & 1 \end{bmatrix} = \mathbf{I_2} \tag{2.15}$$

  The quantum vacuum state is the quantum state with the lowest possible energy (zero energy). Generally, it contains no physical particles.

- **Thermal State**

  The thermal state is defined using the Fock state representation:

$$\boldsymbol{\rho}_{\text{th}} = \sum_{n=0}^{\infty} \frac{\bar{n}^n}{(\bar{n}+1)^{n+1}} |n\rangle\langle n| \tag{2.16}$$

  where $\bar{n}$ is the average number of photons in the system. The mean vector is zero and the CM takes the form of

$$\boldsymbol{\Gamma} = (2\bar{n}+1)\mathbf{I}_2 \tag{2.17}$$

  Thermal states are arguably the most relevant class of states in nature. They provide an efficient description of the equilibrium state for most systems.

- **Coherent State**

  The *displacement operator*, $\hat{\mathbf{D}}(\alpha)$, is a unitary operator which applies a magnitude displacement α to the applied state. The coherent state is obtained by

applying the displacement operator $\hat{\mathbf{D}}(\alpha)$ on the vacuum state

$$|\alpha\rangle = \hat{\mathbf{D}}(\alpha)\,|0\rangle = \exp(\alpha\hat{\mathbf{a}}^\dagger - \alpha^*\hat{\mathbf{a}})\,|0\rangle \tag{2.18}$$

where α^* is the complex conjugate of α.

The Fock state representation for the coherent state is given by

$$|\alpha\rangle = \exp\left(-\frac{1}{2}|\alpha|^2\right)\sum_{n=0}^{\infty}\frac{\alpha^n}{\sqrt{n!}}\,|n\rangle \tag{2.19}$$

Then, the density operator of the coherent state is given as $\boldsymbol{\rho}_{\text{coh}} = |\alpha\rangle\,\langle\alpha|$.

In quantum mechanics, a coherent state is the specific quantum state of the quantum harmonic oscillator, often described as a state which has the dynamics most closely resembling the oscillatory behavior of a classical harmonic oscillator.

Symplectic Transformation of Gaussian States

A major role in the theoretical and experimental manipulation of Gaussian states is played by the unitary operations which preserve the Gaussian characteristics of the states on which they act. Any such unitary operation $\hat{\mathbf{U}}$, together with its Hermitian conjugate transpose $\hat{\mathbf{U}}^\dagger$, acting on the density operator $\boldsymbol{\rho}$ in the Hilbert space corresponds to a symplectic transformation on the mean and covariance matrix in the phase space.

$$\boldsymbol{\rho}' = \hat{\mathbf{U}}\boldsymbol{\rho}\hat{\mathbf{U}}^\dagger \rightarrow \bar{\mathbf{y}}' = \mathbf{S}\bar{\mathbf{y}}, \boldsymbol{\Gamma}' = \mathbf{S}\boldsymbol{\Gamma}\mathbf{S}^T \tag{2.20}$$

where $\mathbf{S}$ is a symplectic matrix corresponding to the action of $\hat{\mathbf{U}}$ on the system density operator $\boldsymbol{\rho}$. The symplectric matrix is defined such that

$$\boldsymbol{\Omega} = \mathbf{S}^T \boldsymbol{\Omega} \mathbf{S} \tag{2.21}$$

where $\boldsymbol{\Omega}$ is the symplectic form and given in eq.2.7. Symplectic matrices are always square, invertible with unit determinant.

Williamson [27] showed a theorem that any symmetric positive-definite matrix can be put into a diagonal form via a symplectic transformation. The proof of the Williamson Theorem can be found in [28]. In this thesis, we focus our attention on the symplectic transformation of the covariance matrix of the Gaussian state $\boldsymbol{\Gamma}$. An important application of this theorem is in finding the symplectic eigenvalues of a Gaussian state, which amounts physically to a *normal mode decomposition* of the system density operator. Then, given the covariance matrix, $\boldsymbol{\Gamma}$, there exists a symplectic matrix $\mathbf{S}$ that diagonalises $\boldsymbol{\Gamma}$ into

$$\boldsymbol{\Gamma} = \mathbf{S}^T \mathbf{V} \mathbf{S} \tag{2.22}$$

where $\mathbf{V}$ is defined as

$$\mathbf{V} = \mathrm{diag}\{v_1, v_1, ..., v_N, v_N\} \tag{2.23}$$

and $\{v_n\}_{n=1}^N$ are *symplectic eigenvalues* of $\boldsymbol{\Gamma}$ and form the *symplectic spectrum* of the CM. We note that the sympletic eigenvalues of $\boldsymbol{\Gamma}$ are pairwise equal. These symplectic eigenvalues can be calculated as the eigenvalues of the matrix $|i\boldsymbol{\Omega}\boldsymbol{\Gamma}|$.

The symplectic eigenvalues are invariant under the action of the symplectic transformations on the covariance matrix, which corresponds to the unitary transformation on

the system density operator. Therefore, the symplectic eigenvalues encode essential information on the Gaussian state and provide powerful ways to express its fundamental properties, which will be explained in the qualification and quantification of entanglement.

2.1.5 Quantum Measurement

The quantum measurement is described by a set of operators $\{\hat{\mathbf{M}}_n\}$ acting on the state space of the system. When the state $|\psi\rangle$ is measured, the probability P_n of a measurement result n occurring is

$$P_n = \langle\psi|\hat{\mathbf{M}}_n^\dagger\hat{\mathbf{M}}_n|\psi\rangle \tag{2.24}$$

where $\hat{\mathbf{M}}_n^\dagger$ denotes the Hermitian conjugate transpose of $\hat{\mathbf{M}}_n$. The state of this system after the measurement becomes

$$|\psi'\rangle = \frac{\hat{\mathbf{M}}_n\,|\psi\rangle}{\sqrt{P_n}} \tag{2.25}$$

where $\frac{1}{\sqrt{P_n}}$ is added such that $\langle\psi'|\psi'\rangle = 1$.

For the completeness of measurements, the sum over all measurement outcomes has to be unity

$$\sum_n P_n = \sum_n \langle\psi|\hat{\mathbf{M}}_n^\dagger\hat{\mathbf{M}}_n|\psi\rangle = \langle\psi|\sum_n \hat{\mathbf{M}}_n^\dagger\hat{\mathbf{M}}_n|\psi\rangle = 1 \tag{2.26}$$

Hence, $\sum_n \hat{\mathbf{M}}_n^\dagger\hat{\mathbf{M}}_n = \hat{\mathbf{I}}$, which shows the completeness of the measurement operators.

For example, if we apply the measurement to the coherent state, $|\alpha\rangle = \exp(-\frac{|\alpha|^2}{2}) \sum_{n=0}^{\infty} \frac{\alpha^n}{\sqrt{n!}} |n\rangle \triangleq \sum_{n=0}^{\infty} a_n |n\rangle$ where $a_n \triangleq \exp(-\frac{|\alpha|^2}{2}) \frac{\alpha^n}{\sqrt{n!}}$. Since the coherent state is defined in terms of Fock number states $\{|n\rangle\}_{n=0}^{\infty}$, the measurement operators of the coherent states can be defined as

$$\hat{\mathbf{M}}_n = |n\rangle \langle n| , \quad n = 0, ..., \infty \tag{2.27}$$

Thus the measurement probability of measuring the coherent state in the number state $|n\rangle$ is given by applying the projective operator $\hat{\mathbf{M}}_n$ onto the coherent state $|\alpha\rangle$

$$P_n = \langle \alpha | \hat{\mathbf{M}}_n^{\dagger} \hat{\mathbf{M}}_n | \alpha \rangle = (\sum_n a_m^* \langle m|) |n\rangle \langle n| (\sum_{m'} a_{m'} |m'\rangle) = |a_n|^2 \tag{2.28}$$

Therefore, the modulus squared of the superposition coefficient gives the probability of the state being in one particular basis state.

2.2 Quantum Entanglement

In the influential 1935 paper [29], results from the experiment conducted by Einsten, Podolsky and Rosen (EPR) showed the incompleteness of quantum mechanics and led to the study of an important property of quantum systems - entanglement. Historically, the continuous-wave entanglement was the first form of entanglement ever defined.

2.2.1 Introduction to Quantum Entanglement

The phenomenon of quantum entanglement lies at the heart of quantum mechanics and may lie at the heart of future quantum technologies. The quantum entanglement is phenomenon that describes the correlation behavior of two quantum systems whose correlation is beyond the classical limit.

Joint State - Bipartite System

For two Hilbert spaces, $\mathcal{H}_A, \mathcal{H}_B$ and one state $|\psi\rangle \in \mathcal{H}_A \otimes \mathcal{H}_B$, this state $|\psi\rangle$ is a product state in the joint Hilbert space if there are pure states $|\psi_A\rangle_A \in \mathcal{H}_A$ and $|\psi_B\rangle_B \in \mathcal{H}_B$ such that

$$|\psi\rangle = |\psi_A\rangle_A \otimes |\psi_B\rangle_B \triangleq |\psi_A\rangle_A |\psi_B\rangle_B \tag{2.29}$$

where $\otimes$ is the tensor product to connect two subsystems, which mathematically stands for the Kronecker product. Then, the state of the bipartite system is called the *joint state* of systems A, B.

Quantum Entanglement

A bipartite pure quantum state, $|\psi\rangle$ is called *entangled* when it cannot be written as a direct product of states of two subsystems as :

$$|\psi\rangle = \left(\sum_n p_n^A |\psi_A^n\rangle_A\right) \otimes \left(\sum_m p_m^B |\psi_B^m\rangle_B\right) \tag{2.30}$$

If the state $|\psi\rangle$ can be written in this form, this state is called *separable*. In this equation, $\{(p_n^A)^2, (p_m^B)^2\}$ are probabilities and $\sum_n (p_n^A)^2 = 1$, $\sum_m (p_m^B)^2 = 1$.

An example of the entangled bipartite states is the $N00N$ state defined as

$$|N00N\rangle = \frac{1}{\sqrt{2}} |N\rangle_A |0\rangle_B + \frac{1}{\sqrt{2}} |0\rangle_A |N\rangle_B \tag{2.31}$$

where $|N\rangle_{A/B}$ denotes that there are N photons in the subsystem A/B. $|N\rangle_A |0\rangle_B$ represents that there are N photons in system A and 0 photon in system B. The other state $|0\rangle_A |N\rangle_B$ can be defined in the same way. The joint state $|\psi\rangle$ can be in the state $|N\rangle_A |0\rangle_B$ or $|0\rangle_A |N\rangle_B$ with an equal probability, 1/2. Then, two systems are entangled in the way that when the photon number of one system is known to be 0 or N , the photon number of the other system must be N or 0 correspondingly.

2.2.2 Bipartite Gaussian State

The qualification and quantification of the entanglement in any two-mode Gaussian state can be studied using the covariance matrix of the bipartite Gaussian state. The covariance matrix can be transformed by means of local unitary operation into a *standard form* [30]

$$\mathbf{\Gamma} = \begin{bmatrix} \boldsymbol{\alpha} & \boldsymbol{\gamma} \\ \boldsymbol{\gamma}^T & \boldsymbol{\beta} \end{bmatrix} \tag{2.32}$$

where

$$\boldsymbol{\alpha} = \begin{bmatrix} a & 0 \\ 0 & a \end{bmatrix}, \quad \boldsymbol{\beta} = \begin{bmatrix} b & 0 \\ 0 & b \end{bmatrix}, \quad \boldsymbol{\gamma} = \begin{bmatrix} c_+ & 0 \\ 0 & c_- \end{bmatrix} \tag{2.33}$$

where $a, b \geq 1$.

The symplectic eigenvalues, $v_{\pm}$, of a bipartite Gaussian state are given as the eigenvalues of the matrix $|i\mathbf{\Omega\Gamma}|$, which are

$$2v_{\pm}^2 = \Delta\mathbf{\Gamma} \pm \sqrt{\Delta\mathbf{\Gamma}^2 - 4\text{det}\mathbf{\Gamma}} \tag{2.34}$$

where $\Delta\mathbf{\Gamma}$ is the *invariant* of the covariance matrix $\mathbf{\Gamma}$ and is defined as $\Delta\mathbf{\Gamma} = \text{det}\boldsymbol{\alpha} + \text{det}\boldsymbol{\beta} + 2\text{det}\boldsymbol{\gamma} = a^2 + b^2 + 2c_+c_-$. The determinant of $\mathbf{\Gamma}$ can be defined in terms of a, b, c_-, c_+: $\text{det}\mathbf{\Gamma} = a^2b^2 - ab(c_+^2 + c_-^2) + c_+^2c_-^2$.

2.2.3 Qualification: PPT Criterion

A very strong necessary and sufficient condition for a state being separable has been proved by Peres [31] and is called the *positive partial transpose* (PPT) criterion. Given the density operator of any bipartite system as $\boldsymbol{\rho} = \sum p_i \boldsymbol{\rho}_{Ai} \otimes \boldsymbol{\rho}_{Bi}$, its partially transposed density matrix $\bar{\boldsymbol{\rho}}$ is obtained by performing transposition with respect to the degrees of freedom of one subsystem only such that $\bar{\boldsymbol{\rho}} = \sum p_i \boldsymbol{\rho}_{Ai}^T \otimes \boldsymbol{\rho}_{Bi}$ or $\bar{\boldsymbol{\rho}} = \sum p_i \boldsymbol{\rho}_{Ai} \otimes \boldsymbol{\rho}_{Bi}^T$. The action of partial transposition in the Hilbert space amounts to a mirror reflection of one of the four quadrature variables in the phase space [32]. The CM, $\mathbf{\Gamma}$ is then transformed into a new matrix $\bar{\mathbf{\Gamma}}$ which differs from $\mathbf{\Gamma}$ by a sign flip in $\text{det}\boldsymbol{\gamma}$. Therefore, the invariant $\Delta(\mathbf{\Gamma})$ is changed to $\Delta(\bar{\mathbf{\Gamma}}) = \text{det}\boldsymbol{\alpha} + \text{det}\boldsymbol{\beta} - 2\text{det}\boldsymbol{\gamma}$. The symplectic eigenvalues $\bar{v}_-, \bar{v}_+$ of $\bar{\mathbf{\Gamma}}$ can be obtained using $\Delta(\bar{\mathbf{\Gamma}})$ in Eq. (2.34).

The PPT criterion relies on the positivity of the partially transposed state. The PPT criterion stated that if a state $\boldsymbol{\rho}$ is separable, then its partial transpose is a

valid density matrix and in particular is positive semidefinite. Therefore, the PPT criterion for separability can be reduced to the inequality that must be satisfied by the smallest symplectic eigenvalue $\bar{v}_-$ of the partially transposed state

$$\bar{v}_- \geq 1 \tag{2.35}$$

which is equivalent to using the definition of $\bar{v}_-$ in Eq.2.34

$$\Delta(\bar{\mathbf{\Gamma}}) \leq \det\bar{\mathbf{\Gamma}} + 1 \tag{2.36}$$

Therefore, the smallest symplectic eigenvalye $\bar{v}_-$ can be used to determine whether a bipartite Gaussian system is separable or not.

2.2.4 Quantum Entanglement Quantification

Negativities

There are a number of useful entanglement measures for Gaussian states. Conventionally, two families of measures have been studied. One family encompasses so called *negativities*. From a quantitative point of view, a measure of entanglement which can be computed for general Gaussian states is provided by the *negativity*, $\mathcal{N}$. It was firstly introduced in [33] and later thoroughly discussed and extended in [34] to continuous variable systems. The negativity of a quantum state $\boldsymbol{\rho}$ is defined as

$$\mathcal{N}(\boldsymbol{\rho}) = \frac{\mathrm{tr}(|\bar{\boldsymbol{\rho}}|) - 1}{2} = \frac{\sum_i |\lambda_i| - \sum_i \lambda_i}{2} \tag{2.37}$$

where $\bar{\boldsymbol{\rho}}$ is the partially transposed density matrix and $\mathrm{tr}(|\bar{\boldsymbol{\rho}}|)$ stands for the trace of $|\bar{\boldsymbol{\rho}}| = \sqrt{\bar{\boldsymbol{\rho}}^H \bar{\boldsymbol{\rho}}}$. Here λ_i represents the eigenvalue of the partially transposed matrix $\bar{\boldsymbol{\rho}}$ and $\mathrm{tr}(\bar{\boldsymbol{\rho}}) = \sum_i \lambda_i = 1$.

The quantity $\mathcal{N}(\boldsymbol{\rho})$ is then equal to the modulus of the sum of the negative eigenvalues of $\bar{\boldsymbol{\rho}}$, $\mathcal{N}(\boldsymbol{\rho}) = |\sum_{i,\lambda_i<0} \lambda_i|$. Therefore, the negativity of the Gaussian state quantifies the extend to which $\bar{\boldsymbol{\rho}}$ fails to be positive because the system is said to be entangled if its partially transposed density operator is not positive semidefinite.

Strictly related to $\mathcal{N}$ is the *logarithmic negativity*, $\mathcal{E}_{\mathcal{N}}$

$$\mathcal{E}_{\mathcal{N}} = \log(\mathrm{tr}(\bar{\boldsymbol{\rho}})) \tag{2.38}$$

For any bipartite Gaussian state $\boldsymbol{\rho}$, both the negativity and the logarithmic negativity are related to $\bar{v}_-$ and are simple decreasing function of $\bar{v}_-$ [34]

$$\mathcal{N}(\boldsymbol{\rho}) = \max\left[0, \frac{1-\bar{v}_-}{2\bar{v}_-}\right] \tag{2.39}$$

$$\mathcal{E}_{\mathcal{N}}(\boldsymbol{\rho}) = \max[0, -\log \bar{v}_-] \tag{2.40}$$

where $\bar{v}_-$ is the smallest symplectic eigenvalue of $\bar{\boldsymbol{\rho}}$.

These two quantities directly quantify the amount by which the necessary and sufficient PPT condition for separability is violated. From these two equations, the symplectic eigenvalue of $\bar{v}_-$ completely quantifies the entanglement of a bipartite Gaussian state. When $\bar{v}_- \geq 1$, both the negativity and logarithmic negativity become zero and the state is separable; otherwise, the state is entangled.

Entanglement of Formation

Given a bipartite Gaussian state $\boldsymbol{\rho}$, the marginal state of A can be obtained by taking the partial trace over B,

$$\boldsymbol{\rho}_A = \mathrm{tr}_B(\boldsymbol{\rho}) \tag{2.41}$$

The marginal state of the system B can be defined in a similar way.

For a pure bipartite Gaussian state, the *entropy of entanglement* of the bipartite Gaussian state is given by the *von Neumann entropy* of its marginal states. Given that the bipartite system is symmetric, the von Neumann entropy of both systems is the same,

$$E(\boldsymbol{\rho}) = S(\boldsymbol{\rho}_A) = S(\boldsymbol{\rho}_B) \tag{2.42}$$

where $E(\boldsymbol{\rho})$ denotes the entropy of entanglement and $S(\boldsymbol{\rho}_{A/B})$ is the von Neumann entropy as defined

$$S(\boldsymbol{\rho}_{A/B}) = -\mathrm{tr}(\boldsymbol{\rho}_{A/B} \log \boldsymbol{\rho}_{A/B}) \tag{2.43}$$

Given the definition of entropy of entanglement, the *entanglement of formation* (EOF) [35] can be computed for the symmetric bipartite Gaussian state [36]

$$E_F(\boldsymbol{\rho}) = \min_{p_i, \boldsymbol{\rho}_i} \sum_i p_i E(\boldsymbol{\rho}_i) \tag{2.44}$$

where the minimisation is taken over all the decomposition of $\boldsymbol{\rho}$ into ensembles of states $\{|\psi_i\rangle\}$ with probabilities $\{p_i\}$: $\boldsymbol{\rho} = \sum_i p_i \boldsymbol{\rho}_i$ and $\boldsymbol{\rho}_i = |\psi_i\rangle \langle\psi_i|$. E is the *von Neumann entropy of entanglement* and defined in Eq.2.42. The entropy of entanglement is the canonical measure of bipartite entanglement in pure states.

The optimal convex decomposition of Eq.2.44 has been found for symmetric two-mode Gaussian states [36]

$$E_F = \max[0.h(\bar{v}_-)] \tag{2.45}$$

with

$$h(x) = \frac{(1+x)^2}{4x}\log\left[\frac{(1+x)^2}{4x}\right] - \frac{(1-x)^2}{4x}\log\left[\frac{(1-x)^2}{4x}\right] \tag{2.46}$$

We note that the EOF is a monotonically decreasing function of $\bar{v}_-$, thus providing a quantification of the entanglement of symmetric states equivalent to the one provided by the negativities.

2.2.5 Generation of Bipartite Entangled States: SPDC

The process of spontaneous parametric down-conversion (SPDC), alternatively known as parametric fluorescence, in a nonlinear crystal is one of the most versatile techniques for the generation of entangled pairs. An incident photon in SPDC is referred to as the *pump* photon with frequency ω_p while the output photons are called the *signal* and *idler* photons[2]. Inside the SPDC structure, the pump photon will split into one pair of photons in accordance with conservation laws of the energy and momentum

$$\omega_p = \omega_s + \omega_i \tag{2.47a}$$

$$\mathbf{k}_p = \mathbf{k}_s + \mathbf{k}_i \tag{2.47b}$$

[2]The pair of photons are so-called because when applied in a quantum radar, the 'signal' is sent out for probing and the 'idler' is retained in the system for measurement.

where ω_j and $\mathbf{k}_j$ are the frequency and wave vector of pump (j=p), signal (j=s), or idler (j=i).

However, as a typical spontaneous quantum nonlinear process, it suffers from extremely poor efficiency due to the very weak nature of nonlinear quantum optical processes. Recently, extensive efforts have been devoted to boost this effect by utilizing conventional design based on nonlinear crystals, waveguides, photonic crystals and ring resonators that are usually bulky or unsuitable for free-space applications. In contrast, metasurfaces are promising novel ultrathin designs to realise saleable and efficient SPDC sources. In [37], a plasomonic metasurface design based on silver nanostripes combined with a bulk lithium niobate ($LiNbO_3$) crystal to realise a scalable, ultrathin and efficient SPDC source. This can have very high photon-pair generation rates.

Chapter 3

Quantum Radar

The quantum radar is a promising technology that could have a strong impact on both the civilian and military applications. The traditional radar signal consists of a huge number of photons such that the particle properties of light cannot be observed because the beam behaves as classical light. Quantum radar generalizes the concept of classical radars, which operates with a relatively small number of photons and is theoretically described inside the context of *quantum electro-dynamics* (QED).

3.1 Motivations and History

The motivation behind the proposal of the quantum radar was the need to improve the sensitivity (lower the limits of indeterminacy in accordance with the number of photons used), as well as to further improve the capability to detect, identify and

resolve various targets of the detection system by taking advantages of quantum phenomena. This is mainly achieved via quantum entanglement [38], which also significantly reduces the unwanted jamming effects.

As nature is most aptly described by quantum mechanics, certain limits are imposed, via the *Heisenberg's uncertainty principle*, on our knowledge gained by various measurements. This uncertainty relationship is an intrinsic and completely unavoidable property of all quantum systems. In the case of a quantum system consisting of N photons and a quantum state to describe them of relative phase ϕ, the uncertainty in the simultaneous measurement of the photon number and phase must satisfy the Heisenberg's uncertainty principle [6] [1] such that

$$\Delta\phi\Delta N \geq 1/2 \tag{3.48}$$

where $\Delta\phi$ and ΔN are the standard deviation of the phase estimation and photon number estimation respectively.

If the monochromatic (single frequency) coherent state is employed, its photon number obeys a Poisson distribution and then the standard deviation in its photon number is $\Delta N = \sqrt{\langle\hat{\mathbf{N}}\rangle_\alpha}$ where $\hat{\mathbf{N}}$ is the photon number operator and $\langle\hat{\mathbf{N}}\rangle_\alpha$ represents the average photon number in the coherent state. The accuracy is limited by the *shot noise* or *Poisson noise*, which applies to photon counting in optical devices associated with the particle nature of light. It also appears as a type of electronic noise which

[1] This uncertainty principle is exact if the variance of the phase is $(|\langle e^{i\hat{\phi}}\rangle|^{-2} - 1)$ where $\hat{\phi}$ is the unbiased estimator of the phase [39]. This variance, named as Holevo variance coincides with the usual variance for a narrow distribution peaked well away from the phase cut (the range of phase being considered).

results from the discrete nature of electric charge. Given the shot noise in the photon number measurement, the uncertainty in the phase estimation is bounded by

$$\Delta\phi \geq \frac{1}{\sqrt{\langle \hat{\mathbf{N}} \rangle}} \tag{3.49}$$

This result is known as the *Standard Quantum Limit* [40] and comes as a consequence of the vacuum fluctuations that affect the measurement of the amplitude in the electromagnetic field as well as the Poissonian statistics of classical light and the discrete nature of the electromagnetic field [41].

However this bound can be in principle be overcome by the use of more optimal measurement techniques and restoring the true fundamental limit as

$$\Delta\phi \geq \frac{1}{\langle \hat{\mathbf{N}} \rangle} \tag{3.50}$$

This provides an improvement of $\sqrt{\langle \hat{\mathbf{N}} \rangle}$ and then the bound on the error in the phase estimation becomes smaller.

This fundamental limit can be achieved through various methods that share the same steps: perform the photon measurements multiple times and collect the results for the later processing [38]. States employed are mainly entangled photons.

3.2 Categories of Quantum Radar Systems

All quantum radar protocols are built to exploit some quantum phenomena. Based on the specific characteristics exploited, quantum radar systems can be generally categorised into 4 types. The first three types have been proposed and accepted for quite a long time while the last category was proposed recently.

Type 1 Quantum Radar: Quantum Transmitter and Classical Receiver

Type-1 quantum sensors transmit unentangled, non-coherent quantum states of light such as the squeezed state in [42]. This type includes *single photon quantum radar*.

The operation of the single photon quantum radar is similar to that in a classical radar system but the transmitted signal only includes one photon instead of a large number of photons as shown in Fig.3.1.

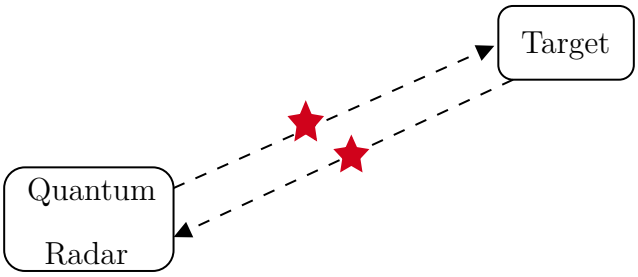

Figure 3.1: The schematic diagram of the single-photon quantum radar [2]

The main advantage in this type of quantum radar arises from the sidelobe structure of the quantum cross section coefficient of rectangular targets, which reaches its highest value at one single photon transmission. Therefore, the target appears bigger in the

quantum system compared with the classical radar systems[4].

Type 2 Quantum Radar: Classical Transmitter and Quantum Receiver

Type-2 quantum radar transmits coherent states of light and uses quantum photosensors to improve the performance of target detection. The *quantum-enhanced LADAR* (laser detection and ranging), which stands for the laser detection and ranging is one typical example. The quantum-enhanced LADAR operates in the visible and near-visible regions, which gives the advantage to such systems due to the shorter wavelengths. Therefore, quantum-enhanced LADAR can resolve smaller spatial information [43]. However, this also leads to the problem of strong attenuation and reflection by fog or cloud as photons at such frequencies propagate in free space In [44], a conceptual design of the Type-2 quantum sensors was introduced.

Type 3 Quantum Radar

Type-3 quantum radar transmits quantum entangled photons. It also employs the quantum receiver to perform the signal reception. One well-studied example is the *quantum illumination* (QI). This type of quantum radar is the main focus of this thesis and will be introduced and discussed in greater details later.

Type 4 Quantum Radar

In this new type of quantum radar systems, the transmitted signal consists of more than one entangled beam. The reference [4] is an example that transmits both the entangled signal and idler beams from the SPDC towards the interested region for parameter estimation.

Type-4 quantum radar may also be considered to include other design, which employs the quantum illumination protocol using multiple entangled photons [45]. Here, the transmitted signal beams includes two entangled beams and the third entangled beam is kept as the idler in the radar system. Then, the detection of two signal photons instead of one provided a higher sensitivity.

3.3 Quantum Illumination

Quantum illumination (QI) was first introduced and developed by Seth Lloyd at MIT [7] as a revolutionary technique which increases the sensitivity of the detection system via the use of entangled photons.

Quantum illumination has a general scheme such that entangled pairs of photons are generated. One, called the *signal*, is sent to detect or track a possible space region where a target could be located. The other, called the *idler*, is sent to the connected fiber and retained in the radar systems for further joint detection with the reflected signal. Here, the fiber provides the idler photon with a certain propagation delay without significant attenuation of the idler photon. In this thesis, we treated "quantum illumination" as a special type of quantum radar, which could enhance the performance of target detection and parameter estimation by exploiting a pair of

entangled signals.

The operation of the quantum illumination is shown in Fig. 3.2.

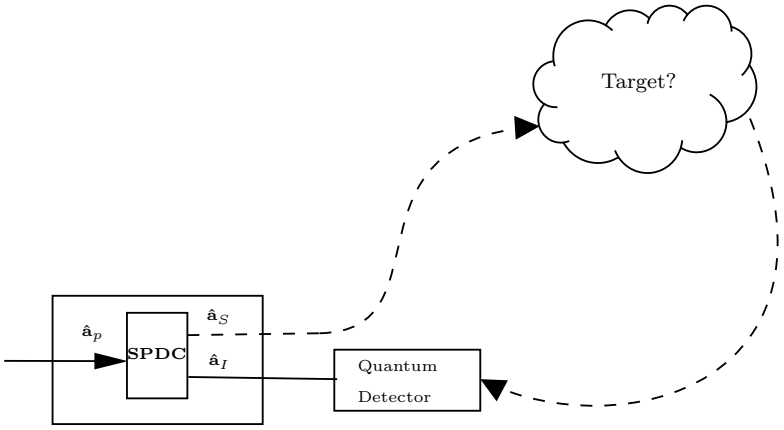

Figure 3.2: The schematic diagram of quantum illumination

Both the signal and the idler can be represented by their annihilation operators, $\hat{\mathbf{a}}_s$ (for the signal) and $\hat{\mathbf{a}}_i$ (for the idler). In addition, $\hat{\mathbf{a}}_p$ represents the incident pump photon.

3.3.1 Attenuation of Quantum Light

When a target is present, the transmitted signal will experience propagation loss and attenuation due to the free-space propagation and the target interaction. As well, any realistic description of quantum radar systems needs to account for the attenuation losses due to the atmosphere. There are two major contributions to atmospheric attenuation: absorption and scattering [46]. Absorption is the process when light is absorbed by the medium and its energy is dissipated as heat. Scattering is the

process when light is absorbed by the medium and re-emitted in some direction with minimal thermodynamic energy dissipation. The analysis of the electromagnetic field in an attenuating media is very complicated and too difficult for the current context. However, it is possible to obtain simplified equations if it is assumed that the medium is adequately described by a chain of beam splitters as shown in Fig. 3.3.

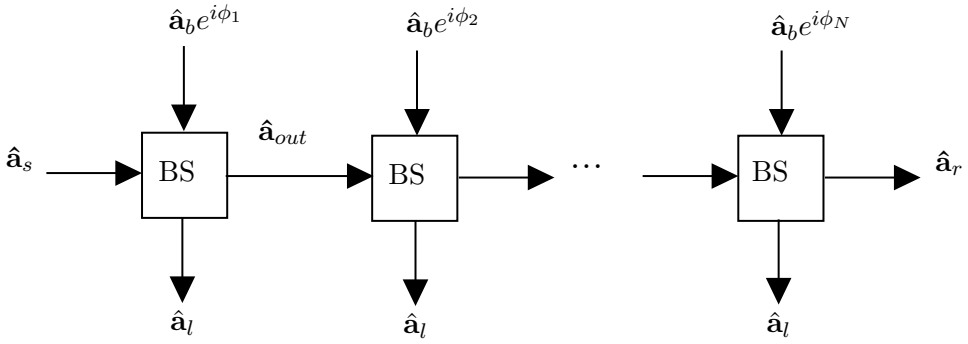

Figure 3.3: The attenuation of the light can be modeled using a chain of beamsplitters.

In this model, the whole propagation process over a total distance z is modelled by N beam splitters. Each beamsplitter shows the attenuation of the useful signal and the introduction of the background noise over a propagation segment Δz. The incident light in the first beam splitter is the transmitted signal from radar. The light that is scattered or absorbed by the medium is represented by $\hat{\mathbf{a}}_l$. Then, the remaining useful signal is $\eta_1 \hat{\mathbf{a}}_s$ where η_1 represents the transmissivity coefficient of the signal. The transmitted light experiences a propagation phase $\exp(i\omega\epsilon\Delta z/c) = \exp(ik\Delta z)$ where $k = \frac{\omega\epsilon(\omega)}{c}$ with $\epsilon(\omega)$ being the refraction index of the medium, and where ω is the frequency of the transmitted signal and c is the speed of light. Throughout this propagation segment, the background noise, denoted by $\hat{\mathbf{a}}_b e^{i\phi_n}$ in the above figure is added to the system. Here, $\hat{\mathbf{a}}_b$ represents the intensity of the background noise and is assumed to be constant. On the other hand, its phase at the nth beamsplitter

denoted by $e^{i\phi_n}$ is assumed random, having a uniform distribution over $[-\pi, \pi]$. The output of the first beamsplitter is given by $\hat{\mathbf{a}}_{\text{out}} = \eta_1 \exp(ik\Delta z)\hat{\mathbf{a}}_s + \hat{\mathbf{a}}_b e^{i\phi_1}$.

To maintain the commutation relation that $[\hat{\mathbf{a}}_{\text{out}}, \hat{\mathbf{a}}_{\text{out}}^\dagger] = 1$, $\hat{\mathbf{a}}_b e^{i\phi_1}$ becomes $\hat{\mathbf{a}}_b e^{i\phi_1}/\sqrt{1-\eta_1^2}$ and the output becomes $\hat{\mathbf{a}}_{\text{out}} = \eta_1 \exp(ik\Delta z)\hat{\mathbf{a}}_s + \eta_2 \hat{\mathbf{a}}_b e^{i\phi_1}$ with $\eta_2 \triangleq \sqrt{1-\eta_1^2}$. This output will be passed to the second beamsplitter and same analysis can be applied. Thus, after N segments, the final output is

$$\hat{\mathbf{a}}_r = \eta_1^N \exp(ikz)\hat{\mathbf{a}}_s + \left\{ \sum_{n=1}^{N} \eta_1^{N-n}\eta_2 \exp[ik(N-n)\Delta z + i\phi_n] \right\} \hat{\mathbf{a}}_b \tag{3.51}$$

The return signal described in Eq.3.51 can be simplified to be represented by

$$\hat{\mathbf{a}}_r = \sqrt{\eta}\hat{\mathbf{a}}_s + \sqrt{1-\eta}\hat{\mathbf{a}}_b \tag{3.52}$$

where η stands for the overall system transmissivity. It is related to the propagating medium, propagating environment, distance, and the target. $\hat{\mathbf{a}}_b$ is the annihilation operator of the background noise, with the average noise photon $N_b/(1-\eta)$. This equation has omitted the frequency dependence of the transmitted signal which it is explicitly shown in the above analysis because the central frequency of the signal is assumed. Furthermore, to maintain the necessary commutation relationship of operators $[\hat{\mathbf{a}}_r, \hat{\mathbf{a}}_r^\dagger] = 1$, a coefficient $\sqrt{1-\eta}$ is added to $\hat{\mathbf{a}}_b$.

3.3.2 Discrete Quantum Illumination

The idea of QI was firstly introduced in the discrete photon number case. At each detection event, the detector can distinguish between d modes per detection event. Here, the number of modes is defined as $d = WT$, where W is the bandwidth of the detector and T is the time duration of the detection window. Now, the signal and idler photons can only be of one of d modes. N_b represents the average number of noise photons per mode. The detection window is designed such that at most one noise photon is detected per detection event: $N_b \cdot d \ll 1$. The reference [7] studied the discrete quantum illumination using one pair of entangled photons in the form:

$$|\psi\rangle = \frac{1}{\sqrt{d}} \sum_{k=1}^{d} |k\rangle_s |k\rangle_i \tag{3.53}$$

where $|k\rangle_s$ means that the signal photon is in the k-th mode. The term $|k\rangle_s |k\rangle_i$ denotes the joint state of having one signal photon and one idler photon in the k-th mode simultaneously. The generated pair of photons can be in any system mode with the equal probability, $\frac{1}{d}$. The signal and idler photons are entangled because they are in the same mode. Given the measurement of the idler beam, the probability of false alarm can be reduced by a factor of d because the received signal will indicate the presence of the target only when it is in the same mode with the idler photon. The noise is in effect reduced by a factor of d. Then, the use of such entangled photons increases the signal to noise ratio SNR by a factor of d.

3.3.3 Continuous Quantum Illumination

The idea of the quantum illumination has been extended to continuous waves by Tan *et.al.* in [8]. They employed the continuous Gaussian states obtained from the SPDC process. Then, instead of transmitting discrete photons, two continuous beam of photons are used. In [8], the bound of minimum probability of error in state discrimination of the quantum illumination was derived. The result showed that quantum illumination with the optimal receiver can achieve 6 dB improvement in the error exponent compared with that of the classical illumination. Then, reference [47] proposed the first feasible detector design in the cw-QI using the optical parametric amplifier. The error exponent of this receiver achieves 3 dB enhancement compared with the *classical illumination* (CI); however, this receiver design is still suboptimal. Then, the second receiver was proposed in [9] using the phase-conjugate receiver, which also achieved 3 dB gain over CI. In [17], it has been shown that the sum-frequency generation (SFG) receiver can achieve the optimal 6 dB improvement. However, the implementation of this proposed detector is not practical and feasible.

3.3.4 Experimental Realization of Quantum Illumination

It is well-known that the losses and noise in realistic scenarios decreases the advantage of adopting the quantum entanglement. However, experimental results showed that the quantum entanglement still provides substantial gains over the classical systems.

Lopaeva *et. al.* [48] in 2013 presented the first experimental realization of quantum

illumination systems. The SPDC is employed to generate two entangled beams of photons. Those generated photons are passed to a high quantum efficiency CCD camera. One beam (idler) is directly detected while the other beam (signal) is passed to a target object (modeled as a 50:50 beamsplitter). Moreover, the signal beam is superimposed with a thermal background noise produced by scattering a laser beam on an Arecchi's rotating ground glass. In this experimental realization, prior information is unknown and a reception strategy based on photon-counting detection and the second-order correlation measurement is employed. Their results showed that the quantum protocols performed much better than its classical counterpart based on classically correlated light at any background noise levels.

Moreover, experimental results in [49] showed the entanglement-enhanced sensing system improved the performance substantially over the classical systems even in a very lossy and noisy environment.

The experiment was carried out in 2018 [50] when the target was a white card. The distance between the target and detector is around 32 cm. The single photon detector was used. A series of lenses are used to collect the photons reflected from the target. The collected light is then coupled into an optical fiber and then is sent to the detector. The performance of QI and CI systems have been investigated using the receiver operating characteristic plot, which showed the significant improvement of the QI system over CI counterparts.

3.3.5 Microwave Quantum Illumination

Currently, most studies have explored the quantum illumination system using signals at optical frequencies due to the easy access and operation of optical devices such as the SPDC process. However, signals at the optical frequency suffer from severe attenuation in the free space unlike the microwave signals used in the classical radar systems. Then, another research topic is to convert the entangled optical photon pairs from visible light to the microwave range. This is called *microwave quantum illumination*. In 2015, Barzanjeh et al. [51] proposed the microwave quantum illumination which relies on the two optical Gaussian beams generated from the SPDC process. Two beams are passed to an electro-optomechanical (EOM) cavity, which converts the optical to microwave signals. The process is called *collimation*. After this process, the microwave signal is sent towards the interested region and later it is returned detected. It is then converted back to the optical frequency by another EOM converter which converts the microwave to optical signals. Then, the converted optical returned signal and the retained idler can be processed using any detector design. The reliability of microwave quantum illumination using this design at the laboratory level was demonstrated. A major deficiency of this technique is the low efficiency of the frequency conversion. Then, intense sources of optical SPDC generation are required.

The non-degenerate Josephson parameter amplifer (JPA) [19], [52], [53] has been used as a quantum microwave source in the quantum illumination [19], [54], [55]. JPA generators have been applied in the new proposal of *quantum-enhanced noise radar* [54] and in the experimental verification of the advantage of microwave quantum

illumination at macroscopic distances and at room temperature [19]. The weakness of this method is that the JPA requires an extremely low temperature for its operation. Also, the low achievable intensity of the beams precludes the systematic use of JPA microwave quantum illumination in low range applications.

Chapter 4

Quantum Detection Methods in QI

4.1 From Classical Detection to Quantum Detection

Decision theory treats the choice to be made among multiple hypotheses about the system. In the simplest binary decision problem, there are two hypotheses, exemplified by the absence or presence of a signal $s(t)$ of known form in the input $x(t)$ of a receiver during a certain observation interval $(0, T)$. The received signal under each hypothesis is

- H_0 (null hypothesis): $x(t) = n(t)$ (background noise only)
- H_1 (alternative hypothesis): $x(t) = s_r(t) + n(t)$ (reflected signal and background noise)

where $n(t)$ is a random process representing the noise with certain specified statistical properties. $s_r(t)$ is the returned signal from the target, containing target information.

In quantum mechanics, the received signal is represented by its annihilation operator, $\hat{\mathbf{a}}_r$. Then, accordingly, $\hat{\mathbf{a}}_r$ takes different definitions under two hypotheses. In our signal model for target detection, we have: under H_0, there is only noise, and under H_1, we have a target (see also Eq. (3.52), for which the returned signal is an attenuated version of the transmitted signal. Thus, we have:

- H_0: $\hat{\mathbf{a}}_r = \hat{\mathbf{a}}_b$
- H_1: $\hat{\mathbf{a}}_r = \sqrt{\eta}\hat{\mathbf{a}}_s + \sqrt{1-\eta}\hat{\mathbf{a}}_b$

where $\hat{\mathbf{a}}_b$ represents the noise and $\hat{\mathbf{a}}_s$ stands for the transmitted signal. The parameter η denotes the transmissivity of the useful signal over a noisy medium. Quantum illumination concerns the problem of *quantum hypothesis testing*.

4.1.1 Optimal Detection Strategy

A choice is to be made between two hypotheses about a system: H_0 with its density operator $\boldsymbol{\rho}_0$ and H_1 with $\boldsymbol{\rho}_1$. The prior probabilities associated are π_0 and π_1 respectively. The cost of choosing H_i when H_j is true, $P(H_i|H_j)$, is denoted as c_{ij}. The received signal only has two possible states $\{\boldsymbol{\rho}_0, \boldsymbol{\rho}_1\}$ and the unbiased measurement operator of the system under H_0 is denoted as $\hat{\boldsymbol{M}}_0$ and $\hat{\boldsymbol{M}}_1$ is for the alternative hypothesis. These two measurement operators must satisfy $\hat{\boldsymbol{M}}_0 + \hat{\boldsymbol{M}}_1 = \hat{\mathbf{I}}$ for the measurement completeness where $\hat{\mathbf{I}}$ is the identity operator.

If, under H_1, the received signal $\boldsymbol{\rho}_1$ is measured by the measurement operator $\hat{\boldsymbol{M}}_0$, this gives rise to the detection error of "missing" because $\hat{\boldsymbol{M}}_0$ yields the result of "absence of target" while the target is present. Therefore, the probability of missing is given by:

$$P_M = \mathbb{E}(\hat{\boldsymbol{M}}_0\boldsymbol{\rho}_1) = \mathrm{tr}[\hat{\boldsymbol{M}}_0\boldsymbol{\rho}_1]$$

Similarly, the other error in the detection is the probability of false alarm given by

$$P_{\mathrm{F}} = \mathbb{E}(\hat{\boldsymbol{M}}_1\boldsymbol{\rho}_0) = \mathrm{tr}[\hat{\boldsymbol{M}}_1\boldsymbol{\rho}_0] = \mathrm{tr}[(\hat{\mathbf{I}} - \hat{\boldsymbol{M}}_0)\boldsymbol{\rho}_0] = 1 - \mathrm{tr}(\hat{\boldsymbol{M}}_0\boldsymbol{\rho}_0)$$

where $\mathrm{tr}(\boldsymbol{\rho}_0) = 1$ is used.

Given that C_{ij} is defined as the cost of deciding H_i while H_j is true, the average cost is

$$\begin{aligned}\bar{C} &= \pi_0[C_{00}(1 - P_M) + C_{10}P_M] + \pi_1[C_{01}P_{\mathrm{F}} + C_{11}(1 - P_{\mathrm{F}})] \\ &= \pi_0 C_{00} + \pi_1 C_{01} - \pi_1(C_{01} - C_{11})\mathrm{tr}[(\boldsymbol{\rho}_0 - \lambda\boldsymbol{\rho}_1)\hat{\boldsymbol{M}}_0]\end{aligned} \tag{4.54}$$

where

$$\lambda = \frac{\pi_0(C_{10} - C_{00})}{(1 - \pi_0)(C_{01} - C_{11})} \tag{4.55}$$

Since $C_{01} > C_{11}$, then $\bar{C}$ will be minimised when $\mathrm{tr}[(\boldsymbol{\rho}_0 - \lambda\boldsymbol{\rho}_1)\hat{\boldsymbol{M}}_0]$ is maximised. $(\boldsymbol{\rho}_0 - \lambda\boldsymbol{\rho}_1)$ can be represented in terms of its eigenstates $|\eta_k\rangle$ with the corresponding discrete eigenvalues as defined

$$(\boldsymbol{\rho}_0 - \lambda\boldsymbol{\rho}_1)\,|\eta_k\rangle = \eta_k\,|\eta_k\rangle \tag{4.56}$$

Therefore, $\boldsymbol{\rho}_0 - \lambda\boldsymbol{\rho}_1 = \sum_k \eta_k \left|\eta_k\right\rangle \left\langle\eta_k\right|$ and

$$\mathrm{tr}[(\boldsymbol{\rho}_0 - \lambda\boldsymbol{\rho}_1)\hat{\boldsymbol{M}}_0] = \mathrm{tr}[\sum_k \eta_k \left|\eta_k\right\rangle \left\langle\eta_k\right| \hat{\boldsymbol{M}}_0] = \sum_k \eta_k \left\langle\eta_k\right|\hat{\boldsymbol{M}}_0\left|\eta_k\right\rangle \tag{4.57}$$

Then, the maximisation of $\sum_k \eta_k \left\langle\eta_k\right|\hat{\boldsymbol{M}}_0\left|\eta_k\right\rangle$ can be performed if

$$\left\langle\eta_k\right|\hat{\boldsymbol{M}}_0\left|\eta_k\right\rangle = 1,\ \eta_k \geq 0$$
$$\left\langle\eta_k\right|\hat{\boldsymbol{M}}_0\left|\eta_k\right\rangle = 0,\ \eta_k < 0$$

Therefore, the optimal measurement operator of H_0 is given by the eigenvectors with non-negative eigenvalue of $(\boldsymbol{\rho}_0 - \lambda\boldsymbol{\rho}_1)$ and is written as

$$\hat{\boldsymbol{M}}_0 = \sum_{k,\eta_k \geq 0} \left|\eta\right\rangle_k \left\langle\eta_k\right| \tag{4.58}$$

The previous analysis up to now concerns the design of optimum measurement operators; therefore, such analysis assumes the full knowledge of both ρ_0 and ρ_1. In practice, however, We often encounter scenarios in which the background noise is unknown and must be estimated. More importantly, the returned signal from the target is also unknown. Hence, the optimum measurement operators cannot be realized in practice. Without the full knowledge of ρ_0 and ρ_1, we try here to design measurement operators whose performance may approach as closely as possible to the optimum.

4.2 Quantum Chernoff Bound in Gaussian State QI

The detection problem considered in Quantum Illumination concerns the discrimination between two Gaussian states. Based on the exact quantum statistics for the entangled signal and idler beams obtained from the continuous-wave SPDC process, the mode pair with annihilation operators $\hat{\mathbf{a}}_s, \hat{\mathbf{a}}_i$ is in the maximally entangled state. Thus, the joint state is represented in the Fock number basis such that [14]

$$|\psi\rangle_{\text{si}} = \sum_{n=0}^{\infty} \sqrt{\frac{N_s^n}{(N_s+1)^{n+1}}} \, |n\rangle_s \, |n\rangle_i \tag{4.59}$$

where $|\psi\rangle_{\text{si}}$ denotes the joint state of the signal and idler. N_s is the average photon number per mode. The term $|n\rangle_s \, |n\rangle_i$ denotes the joint state of having n photons in the signal beam and n photons in the idler beam simultaneously. The term $\frac{N_s^n}{(N_s+1)^{n+1}}$ gives the probability that this joint state, $|n\rangle_s \, |n\rangle_i$, will happen.

The output $|\psi\rangle_{\text{si}}$ is a joint Gaussian state in the canonical representation with the operator vector $\hat{\mathbf{v}}_c \triangleq [\hat{\mathbf{v}}_c^1 \;\; \hat{\mathbf{v}}_c^2 \;\; \hat{\mathbf{v}}_c^3 \;\; \hat{\mathbf{v}}_c^4]^T = [\hat{\mathbf{a}}_s \;\; \hat{\mathbf{a}}_i \;\; \hat{\mathbf{a}}_s^\dagger \;\; \hat{\mathbf{a}}_i^\dagger]^T$, where $\hat{\mathbf{v}}_c^k$ denotes the kth canonical operator in $\hat{\mathbf{v}}_c$. Thus, the application of the vector of operators $\hat{\mathbf{v}}_c$ on the system state $\boldsymbol{\rho}_{\text{si}} = |\psi\rangle_{\text{si}} \langle\psi|$ gives random results whose mean is given by

$$\bar{\mathbf{v}}_c \triangleq \langle \hat{\mathbf{v}}_c \rangle_{\boldsymbol{\rho}_{si}} = [\bar{v}_c^1 \;\; \bar{v}_c^2 \;\; \bar{v}_c^3 \;\; \bar{v}_c^4]^T \tag{4.60}$$

where each element $\bar{v}_c^k, k = 1, 2, 3, 4$, is given by

$$\bar{v}_c^k = \langle \hat{\mathbf{v}}_c^k \rangle_{\boldsymbol{\rho}_{\text{si}}} = \text{tr}[\hat{\mathbf{v}}_c^k \boldsymbol{\rho}_{\text{si}}] = \text{tr}[\hat{\mathbf{v}}_c^k \left|\psi\right\rangle_{\text{si}} \left\langle\psi\right|_{\text{si}}] = \left\langle\psi\right|_{\text{si}} \hat{\mathbf{v}}_c^k \left|\psi\right\rangle_{\text{si}} \tag{4.61}$$

The detailed derivation process is included in Appendix.A.1 and the mean is

$$\bar{\mathbf{v}}_c = [0 \;\; 0 \;\; 0 \;\; 0]^T \tag{4.62}$$

Then its covariance matrix $\boldsymbol{\Gamma} \triangleq \langle \hat{\mathbf{v}}_c \cdot \hat{\mathbf{v}}_c^\dagger \rangle$, evaluated in Appendix A.1,

$$\boldsymbol{\Gamma} = \begin{bmatrix} N_s + 1 & 0 & 0 & \sqrt{N_s(N_s+1)} \\ 0 & N_s + 1 & \sqrt{N_s(N_s+1)} & 0 \\ 0 & \sqrt{N_s(N_s+1)} & N_s & 0 \\ \sqrt{N_s(N_s+1)} & 0 & 0 & N_s \end{bmatrix} \tag{4.63}$$

The diagonal elements in $\boldsymbol{\Gamma}$ are given by the intensity of the signal or idler beam while the anti-diagonal elements, $\sqrt{N_s(N_s+1)}$ reflect on the correlation between the signal and idler beams. Viewed in this way, it is easily seen that $\left|\psi\right\rangle_{si}$ is maximally entangled because the magnitudes of nonzero off-diagonal terms in $\boldsymbol{\Gamma}$ is equal to the maximum value allowed by quantum mechanics given the diagonal elements of that matrix. Indeed, the upper limit on the magnitudes of these off-diagonal terms for a classical state where the signal and idler modes are unentangled, is N_s [8].

For the characterization of the receiver side, the vector of operators includes operators of received signal and the retained idler, $\hat{\mathbf{v}}_r = [\hat{\mathbf{a}}_r \quad \hat{\mathbf{a}}_i \quad \hat{\mathbf{a}}_r^\dagger \quad \hat{\mathbf{a}}_i^\dagger]^T$.

Under H_0, $\hat{\mathbf{a}}_r = \hat{\mathbf{a}}_b$. Then its mean $\langle \hat{\mathbf{v}}_r^{(0)} \rangle = [0 \quad 0 \quad 0 \quad 0]^T$ and the covariance matrix $\mathbf{\Gamma}_0$ is

$$\mathbf{\Gamma}_0 = \text{diag}\{N_b + 1, N_s + 1, N_b, N_s\} \tag{4.64}$$

Under H_1, $\hat{\mathbf{a}}_r = \sqrt{\eta}\hat{\mathbf{a}}_s + \sqrt{1-\eta}\hat{\mathbf{a}}_b$. Then its mean $\langle \hat{\mathbf{v}}_r^{(1)} \rangle = [0 \quad 0 \quad 0 \quad 0]^T$ and the covariance matrix $\mathbf{\Gamma}_1$ is

$$\mathbf{\Gamma}_1 = \begin{bmatrix} \eta N_s + N_b + 1 & 0 & 0 & \sqrt{\eta N_s(N_s+1)} \\ 0 & N_s + 1 & \sqrt{\eta N_s(N_s+1)} & 0 \\ 0 & \sqrt{\eta N_s(N_s+1)} & \eta N_s + N_b & 0 \\ \sqrt{\eta N_s(N_s+1)} & 0 & 0 & N_s \end{bmatrix} \tag{4.65}$$

The decision between two hypotheses becomes the problem of distinguishing between two Gaussian states, each of which is fully characterized by its mean vector and covariance matrix. As shown in previous section, the minimum probability of error can be achieved by designing the operator using the eigenvectors with nonnegative eigenvalues of $(\boldsymbol{\rho}_0 - \lambda\boldsymbol{\rho}_1)$, which is infeasible in the practical implementation. Then, the *quantum Chernoff Bound* (QCB) places an upper bound on the minimum probability of error in the discrimination between two Gaussian states. The derivation of the QCB relies on the covariance matrix in the quadrature representation $\hat{\mathbf{v}}_q = [\hat{\mathbf{x}}_r \ \hat{\mathbf{p}}_r \ \hat{\mathbf{x}}_i \ \hat{\mathbf{p}}_i]$ where $\hat{\mathbf{x}} = \frac{\hat{\mathbf{a}}+\hat{\mathbf{a}}^\dagger}{\sqrt{2}}$ and $\hat{\mathbf{p}} = -\frac{i(\hat{\mathbf{a}}-\hat{\mathbf{a}}^\dagger)}{\sqrt{2}}$. Its mean of this vector of quadrature operators is

$$\bar{\mathbf{y}} = \langle \hat{\mathbf{v}}_q \rangle = \mathbf{0} \tag{4.66}$$

Then, the covariance matrices in the quadrature representation can be obtained from

$\mathbf{\Gamma}_0$ and $\mathbf{\Gamma}_1$ respectively.

$$\mathbf{\Gamma}_0^q = \frac{1}{4}\text{diag}\{2N_b+1, 2N_b+1, 2N_s+1, 2N_s+1\} \tag{4.67}$$

$$\mathbf{\Gamma}_1^q = \frac{1}{4}\begin{bmatrix} 2\eta N_s + 2N_b + 1 & 0 & 2\sqrt{\eta N_s(N_s+1)} & 0 \\ 0 & 2\eta N_s + 2N_b + 1 & 0 & -2\sqrt{\eta N_s(N_s+1)} \\ 2\sqrt{\eta N_s(N_s+1)} & 0 & 2N_s+1 & \\ 0 & -2\sqrt{\eta N_s(N_s+1)} & 0 & 2N_s+1 \end{bmatrix} \tag{4.68}$$

In the following context, $\mathbf{\Gamma}^q$ will be defined using quadrature operators while $\mathbf{\Gamma}$ will be defined using bosonic operators.

The following will present the derivation of the Gaussian state QCB, which requires the symplectic diagonalisation of the covariance matrices.

4.2.1 Symplectic Diagonalisation and Normal Mode Decomposition

Fundamental properties of the Gaussian states can be easily expressed by the symplectic manipulation of the covariance matrices. By definition, a matrix $\mathbf{S}$ is called *symplectic* when it preserves the symplectic form

$$\boldsymbol{S\Omega S}^T = \mathbf{\Omega} \tag{4.69}$$

where $\mathbf{\Omega}$ is given in Eq.2.7.

Let n represents the number of modes considered in the system, while each mode is considered as a subsystem of the whole system. According to Williamson's Theorem [27], there exists a symplectic matrix $\mathbf{S}$ for every covariance matrix, $\mathbf{\Gamma}$ such that

$$\mathbf{\Gamma} = \mathbf{S} \begin{bmatrix} v_1 & & & & \\ & v_1 & & & \\ & & ... & & \\ & & & v_n & \\ & & & & v_n \end{bmatrix} \mathbf{S}^T = \mathbf{S}[\bigoplus_{k=1}^{n} v_k \mathbf{I}_2]\mathbf{S}^T \tag{4.70}$$

where $\bigoplus$ denotes the direct sum. The direct sum of the above 2×2 matrices $v_k \mathbf{I}_2$ is to formulate a matrix whose diagonal elements are given by these 2×2 block matrices. The set $\{v_1, v_2, ..., v_{n-1}, v_n\}$ is called the *symplectic spectrum*. In particular, this spectrum satisfies

$$\prod_{k=1}^{n} v_k = \sqrt{\det \mathbf{\Gamma}} \tag{4.71}$$

As mentioned in Section 2.1.3, because the covariance matrix $\mathbf{\Gamma}$ and the density operator $\boldsymbol{\rho}$ are connected by Eq.2.13, it can be shown [56], [57] that the symplectic diagonalisation of the covariance matrix as given in Eq.4.70 is equivalent to the unitary transformation $\hat{\mathbf{U}}$ on the system density matrix, which is called as the *normal mode decomposition* of the Gaussian state. The normal mode decomposition of Gaussian states is to split the Gaussian states into decoupled states. Since in QI, we deal with mainly the received signal and the idler; therefore, from now on, we fix the number of subsystems $n = 2$. From Eq.2.20, the normal mode decomposition of the two-mode

Gaussian states is given by [56], [57]

$$\boldsymbol{\rho} = \hat{\mathbf{U}}\Big[\bigotimes_{k=1}^{2} \boldsymbol{\rho}_{\mathrm{th}}(v_k)\Big]\hat{\mathbf{U}}^{\dagger} \tag{4.72}$$

where $\hat{\boldsymbol{U}}$ is the unitary transformation that preserves the Gaussian properties of $\boldsymbol{\rho}$. $\bigotimes_{k=1}^{2} \boldsymbol{\rho}_{\mathrm{th}}(v_k)$ represents the joint state of two thermal states with $\boldsymbol{\rho}_{\mathrm{th}}(v_k)$. The definition of the thermal state is shown in Eq.2.16 with $\bar{n} = \frac{v_k - 1}{2}$[27] and the corresponding thermal state is given as

$$\boldsymbol{\rho}_{\mathrm{th}}(v_k) = \frac{2}{v_k + 1} \sum_{j=0}^{\infty} \left(\frac{v_k - 1}{v_k + 1}\right)^{j} |j\rangle_k \langle j| \tag{4.73}$$

This is a thermal state with the mean photon number $\bar{n} = \frac{v_k - 1}{2}$. We observed that the normal mode decomposition of Eq.4.72 in fact transforms a two-mode Gaussian state into two independent thermal states. The average photon number in kth thermal state is proportional to the symplectic eigenvalue v_k.

4.2.2 Quantum Chernoff Bound

For a quantum detector, there is a finite bandwidth W and time durantion T; therefore, for each detection event, it can detect M modes where $M = WT$. Then, the received signal consists of M identical copies and then the joint state of M modes as mentioned in Sec. 1.2.1 is given by

- H_0: $\boldsymbol{\rho}_0 \otimes \cdots \otimes \boldsymbol{\rho}_0 \triangleq \boldsymbol{\rho}_0^{\otimes M}$
- H_1: $\boldsymbol{\rho}_1 \otimes \cdots \otimes \boldsymbol{\rho}_1 \triangleq \boldsymbol{\rho}_1^{\otimes M}$

where $\boldsymbol{\rho}_0 = \boldsymbol{\rho}_b \otimes \boldsymbol{\rho}_i$ and $\boldsymbol{\rho}_1 = \eta\boldsymbol{\rho}_{\rm si} + (1-\eta)\boldsymbol{\rho}_b \otimes \boldsymbol{\rho}_i$ represent the Gaussian states under H_0 and H_1. $\boldsymbol{\rho}_b$ represents the density operator of the background noise with $\boldsymbol{\rho}_b = \sum_{n=0}^{\infty} \sqrt{\frac{N_b^n}{(N_b+1)^{n+1}}} \left|n\right\rangle \left\langle n\right|$ where N_b stands for the average number of noise photons. $\boldsymbol{\rho}_{\rm si}$ is the density operator of the SPDC output: $\boldsymbol{\rho}_{\rm si} = \left|\psi_{\rm si}\right\rangle \left\langle \psi_{\rm si}\right|$.

The probability of error given $P(H_0) = \pi_0$ and $P(H_1) = \pi_1$ is

$$\begin{aligned} P_e &= \pi_0 P_{\rm F} + \pi_1 P_{\rm M} = \pi_0 {\rm tr}[\hat{\mathbf{M}}_1 \boldsymbol{\rho}_0] + \pi_1 {\rm tr}[\hat{\mathbf{M}}_0 \boldsymbol{\rho}_1] \\ &= {\rm tr}[\hat{\mathbf{M}}_1 \pi_0 \boldsymbol{\rho}_0] + {\rm tr}[\hat{\mathbf{M}}_0 \pi_1 \boldsymbol{\rho}_1] \\ &= \pi_1 - {\rm tr}[\hat{\mathbf{M}}_1 \pi_1 \boldsymbol{\rho}_1] + {\rm tr}[\hat{\mathbf{M}}_1 \pi_0 \boldsymbol{\rho}_0] \\ &= \pi_1 - {\rm tr}[\hat{\mathbf{M}}_1 (\pi_1 \boldsymbol{\rho}_1 - \pi_0 \boldsymbol{\rho}_0)] \end{aligned} \tag{4.74}$$

Thus, the minimization of P_e corresponds to the maximization of the second term in Eq. (4.74), which means that the measurement operator $\hat{\mathbf{M}}_1$ should be formed by the eigenvectors corresponding to all the positive eigenvalues of $(\pi_1 \boldsymbol{\rho}_1 - \pi_0 \boldsymbol{\rho}_0)$, i.e.,

$$\hat{\mathbf{M}}_1 = \sum_{k, v_k > 0} \left|v_k\right\rangle \left\langle v_k\right| \tag{4.75}$$

This positive part of a matrix, $\mathbf{R}$, is represented by $\mathbf{R}_+ = \frac{1}{2}(|\mathbf{R}| + \mathbf{R})$ where $|\mathbf{R}| = (\mathbf{R}^H \mathbf{R})^{1/2}$. Using this expression of the positive part of a matrix, the minimum of

the probability of error in Eq. (4.74) is given by

$$\begin{aligned} P_{e,\min} &= \pi_1 - \mathrm{tr}\left[\frac{1}{2}\Big\{|\pi_1\boldsymbol{\rho}_1 - \pi_0\boldsymbol{\rho}_0| + (\pi_1\boldsymbol{\rho}_1 - \pi_0\boldsymbol{\rho}_0)\Big\}\right] \\ &= \pi_1 - \frac{1}{2}(\pi_1 - \pi_0) - \frac{1}{2}\mathrm{tr}\Big(|\pi_1\boldsymbol{\rho}_1 - \pi_0\boldsymbol{\rho}_0|\Big) \\ &= \frac{1}{2}\Big[\pi_1 + \pi_0 - \mathrm{tr}\Big(|\pi_1\boldsymbol{\rho}_1 - \pi_0\boldsymbol{\rho}_0|\Big)\Big] \\ &= \frac{1}{2}\Big[\mathrm{tr}(\pi_1\boldsymbol{\rho}_1) + \mathrm{tr}(\pi_0\boldsymbol{\rho}_0) - \mathrm{tr}\Big(|\pi_1\boldsymbol{\rho}_1 - \pi_0\boldsymbol{\rho}_0|\Big)\Big] \\ &= \frac{1}{2}\mathrm{tr}(\pi_1\boldsymbol{\rho}_1 + \pi_0\boldsymbol{\rho}_0 - |\pi_1\boldsymbol{\rho}_1 - \pi_0\boldsymbol{\rho}_0|) \end{aligned} \tag{4.76}$$

where we have used the fact that $\mathrm{tr}(\pi_1\boldsymbol{\rho}_1) = \pi_1$ and $\mathrm{tr}(\pi_0\boldsymbol{\rho}_0) = \pi_0$ given that $\mathrm{tr}(\boldsymbol{\rho}_0) = \mathrm{tr}(\boldsymbol{\rho}_1) = 1$.

The following theorem [58] provides an upper bound to the minimum probability of error given in Eq. (4.76):

Theorem 4.2.1 (i) *Given two positive operators* $\mathbf{A}$ *and* $\mathbf{B}$ *and any* $0 \le s \le 1$,

$$\frac{1}{2}\mathrm{tr}\Big[\mathbf{A} + \mathbf{B} - |\mathbf{A} - \mathbf{B}|\Big] \le \mathrm{tr}(\mathbf{A}^s\mathbf{B}^{1-s}) \tag{4.77}$$

(ii) *Let* $\mathbf{A} = \pi_1\boldsymbol{\rho}_1$ *and* $\boldsymbol{B} = \pi_0\boldsymbol{\rho}_0$ *in Eq. (4.77). Then, the minimum error probability in Eq.(4.76) is upper bounded by*

$$P_{e,\min} \le \inf_{0\le s\le 1} \mathrm{tr}[(\pi_0\boldsymbol{\rho}_0)^s(\pi_1\boldsymbol{\rho}_1)^{1-s}] \le \inf_{0\le s\le 1} \frac{1}{2}\mathrm{tr}(\boldsymbol{\rho}_0^s\boldsymbol{\rho}_1^{1-s}) \tag{4.78}$$

(iii) *When the received signal consists of* M *identical copies, the minimum error probability becomes*

$$P_{e,\min} \le \frac{1}{2}\big[\inf_{0\le s\le 1} \mathrm{tr}(\boldsymbol{\rho}_0^s\boldsymbol{\rho}_1^{1-s})\big]^M \triangleq \frac{1}{2}\big[\inf_{0\le s\le 1} Q_s\big]^M \tag{4.79}$$

where $Q_s = \mathrm{tr}(\boldsymbol{\rho}_0^s \boldsymbol{\rho}_1^{1-s})$

The detailed proof of the above theorem can be found in Appendix.A.2.

Eq. (4.79) is called the *Quantum Chernoff Bound* of the minimum probability of error. When $s = \frac{1}{2}$, this error bound is called the *Quantum Bhattarchayya bound*.

We note that the upper bound on the minimum probability of error in Eq.4.79 is dependent on Q_s. To find the function Q_s, we proceed as follows:

Given that the knowledge of $\boldsymbol{\rho}_0$ and $\boldsymbol{\rho}_1$, calculating the power of these two operators, $\boldsymbol{\rho}_0^s$ and $\boldsymbol{\rho}_1^{1-s}$ will involve complicated procedures; therefore, the normal mode decomposition is employed to simplify the derivation with the clear procedure shown in Appendix A.3.

Applying the symplectic transformation on the covariance matrices $\boldsymbol{\Gamma}_0^q$ and $\boldsymbol{\Gamma}_1^q$ of Gaussian states as given in Eqs.4.67 and 4.68 with the corresponding symplectic matrices $\mathbf{S_0}$ and $\mathbf{S}_1$, let $\{\alpha_k\}$ and $\{\beta_k\}$ be the symplectic eigenvalues obtained and let $\bar{\mathbf{y}}_0$ and $\bar{\mathbf{y}}_1$ be the averaged value of $\hat{\mathbf{v}}_r^j = [\hat{\mathbf{x}}_r^j \ \hat{\mathbf{p}}_r^j \ \hat{\mathbf{x}}_i^j \ \hat{\mathbf{p}}_i^j]$ on the density operator under the hypotheses $H_0, (j = 0)$ and $H_1.(j = 1)$ respectively. Then, we have the following theorem [56].

Theorem 4.2.2 *For any two n-mode Gaussian states* $\boldsymbol{\rho}_0$ *and* $\boldsymbol{\rho}_1$ *having respective normal mode decompositions* $(\bar{\mathbf{y}}_0, \mathbf{S}_0, \{\alpha_k\})$ *and* $(\bar{\mathbf{y}}_1, \mathbf{S}_1, \{\beta_k\})$*, we have,*

$$Q_s = \bar{Q}_s \exp\left\{-\frac{1}{2}\mathbf{d}^T\Big[\boldsymbol{V}_0(s) + \mathbf{V}_1(1-s)\Big]^{-1}\mathbf{d}\right\} \tag{4.80}$$

where

$$\bar{Q}_s = \frac{2^n \prod_{k=1}^{n} G_s(\alpha_k) G_{1-s}(\beta_k)}{\sqrt{\det[\mathbf{V}_0(s) + \mathbf{V}_1(1-s)]}} \tag{4.81}$$

And $\mathbf{d} = \bar{\mathbf{y}}_0 - \bar{\mathbf{y}}_1$

$$\mathbf{V}_0(s) = \mathbf{S}_0[\bigoplus_{k=1}^{n} F_s(\alpha_k)\mathbf{I}_2]\mathbf{S}_0^T \tag{4.82}$$

$$\mathbf{V}_1(1-s) = \mathbf{S}_1[\bigoplus_{k=1}^{n} F_{1-s}(\beta_k)\mathbf{I}_2]\mathbf{S}_1^T \tag{4.83}$$

Two defined functions $G_p(x)$ and $F_p(x)$ are

$$G_p(x) = \frac{2^p}{(x+1)^p - (x-1)^p} \tag{4.84a}$$

$$F_p(x) = \frac{(x+1)^p + (x-1)^p}{(x+1)^p - (x-1)^p} \tag{4.84b}$$

The detailed derivation and development of this theorem is included in the appendix A.3.

Quantum Chernoff Bound of QI with SPDC Signal

Let us now apply the results of Theorems 4.2.1 and 4.2.2 to the case of the QI binary detection described in Eqs. (4.64) and (4.65). At the QI receiver, both system states under the two different hypothesis $\boldsymbol{\rho}_1$, $\boldsymbol{\rho}_0$ have zero means, i.e., $\bar{\mathbf{y}}_0 = \bar{\mathbf{y}}_1 = \mathbf{0}$; hence, the exponential term in Eq. (4.80) becomes unity, and thus, $Q_s = \bar{Q}_s$. The symplectic matrix $\mathbf{S}_0$ of $\boldsymbol{\Gamma}_0^p$ is the identity matrix $\mathbf{I}_4$. And its corresponding symplectic spectra

[8] are $\alpha_1 = \frac{2N_b+1}{4}$ and $\alpha_2 = \frac{2N_s+1}{4}$. The symplectic matrix $\mathbf{S}_1$ of $\mathbf{\Gamma}_1^p$ is [8]

$$\mathbf{S}_1 = \begin{bmatrix} \mathbf{X}_+ & \mathbf{X}_- \\ \mathbf{X}_- & \mathbf{X}_+ \end{bmatrix} \tag{4.85}$$

where

$$\mathbf{X}_+ = \begin{bmatrix} x_+ & 0 \\ 0 & x_+ \end{bmatrix}, \quad \mathbf{X}_- = \begin{bmatrix} x_- & 0 \\ 0 & -x_- \end{bmatrix} \tag{4.86}$$

and

$$\begin{aligned} x_+ &= \sqrt{\frac{A+S+\sqrt{(A+S)^2-4\eta C^2}}{2\sqrt{(A+S)^2-4\eta C^2}}} \\ x_- &= \sqrt{\frac{A+S-\sqrt{(A+S)^2-4\eta C^2}}{2\sqrt{(A+S)^2-4\eta C^2}}} \end{aligned} \tag{4.87}$$

where $A = 2\eta N_s + N_b$, $S = 2N_s + 1$ and $B = 2N_b + 1$, $C = 2\sqrt{N_s(N_s+1)}$.

Then, for $\mathbf{\Gamma}_1^p$,

$$\beta_k = \frac{1}{8}[(-1)^k(S-A) + \sqrt{(A+S)^2 - 4\eta C^2}] \tag{4.88}$$

$\alpha_1, \alpha_2, \beta_1, \beta_2$ and $\mathbf{S_0}, \mathbf{S_1}$ are obtained for $\mathbf{\Gamma}_0^p$ and $\mathbf{\Gamma}_1^p$. Using the theorem mentioned above, the corresponding quantum Bhattacharyya bound can be derived as shown

$$P_e \leq \frac{1}{2}\left\{\frac{16}{(\sqrt{\alpha_1+1}-\sqrt{\alpha_1-1})(\sqrt{\alpha_2+1}-\sqrt{\alpha_2-1})(\sqrt{\beta_1+1}-\sqrt{\beta_1-1})(\sqrt{\beta_2+1}-\sqrt{\beta_2-1})}\right\}^M \cdot \left\{\frac{1}{[x_+^2 F_{\frac{1}{2}}(\beta_1) + x_-^2 F_{\frac{1}{2}}(\beta_2) + F_{\frac{1}{2}}(\alpha_1)][x_-^2 F_{\frac{1}{2}}(\beta_1) + x_+^2 F_{\frac{1}{2}}(\beta_2) + F_{\frac{1}{2}}(\alpha_2)] - [x_+ x_- - F_{\frac{1}{2}}(\beta_1)F_{\frac{1}{2}}(\beta_2)]}\right\}^M \tag{4.89}$$

where $F_{\frac{1}{2}}(x)$ is given by the Eq.4.84b with $p = \frac{1}{2}$. It can be seen that the analytic expression for this bound in Eq.4.89 is very cumbersome and it is hard to see

clearly the relationship between the error bound and η, N_s, N_b and M. However, when $\eta \ll 1, N_s \ll 1, N_b \gg 1$, this expression can be simplified to a much more compact approximation of this bound as shown

$$P_e \leq \frac{1}{2}\exp(-\frac{M\eta N_s}{N_b}) \tag{4.90}$$

Then, the error probability for quantum illumination is upper bounded by Eq.4.90.

If we apply the error bound development in Theorem 4.2.2 to the *coherent illumination* which employs the signal and idler that are correlated only to the maximum degree allowed by the classical states (see Sec.2.2), then, the minimum error probability bound will be given [8]

$$P_e^{(CI)} \leq \frac{1}{2}\exp(-\frac{M\eta N_s}{4N_b}) \tag{4.91}$$

The QI with the optimal detection is expected to achieve 6 dB improvement in the error exponent over the coherent illumination case. This result shows the expected superior performance of the quantum illumination systems over the classical counterparts.

4.3 Power Detection Methods in QI

The calculated QCB shows the advantage of the quantum illumination system over classical radar systems. Then, the receiver design to reach this bound is pursued. Current researches on the detector design included the proposal of detectors using the optical parametric amplifier and the phase conjugator respectively. The design

with the amplifier will be discussed in this section. However, it has to be noted that these two detectors are suboptimal, and can only achieve a 3 dB improvement over classical illumination systems.

4.3.1 Optical Parametric Amplifier

Central to the first practical quantum detection method in the QI using SPDC signals is the use of the *optical parametric amplifier* (OPA), which is used to exploit the entanglement. Here, we will briefly discuss its operation. An OPA is an opto-electronic device which uses *four-wave mixing* enabled by the *Kerr nonlinearity* to amplify optical signals [59]. The operation of the OPA with a power gain G is shown in Fig.4.4 and governed by the matrix equation

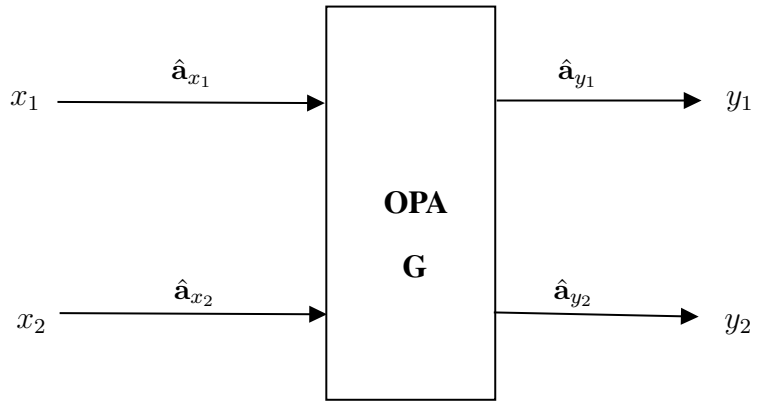

Figure 4.4: The schematic diagram of the OPA with two inputs x_1, x_2 and two outputs y_1, y_2

$$\begin{bmatrix} \hat{\mathbf{a}}_{y_1} \\ \hat{\mathbf{a}}^{\dagger}_{y_2} \end{bmatrix} = \begin{bmatrix} \sqrt{G} & \sqrt{G-1} \\ \sqrt{G-1} & \sqrt{G} \end{bmatrix} \begin{bmatrix} \hat{\mathbf{a}}_{x_1} \\ \hat{\mathbf{a}}^{\dagger}_{x_2} \end{bmatrix} \tag{4.92}$$

The OPA takes two inputs with the annihilation operator, $\hat{\mathbf{a}}_{x_1}$ and $\hat{\mathbf{a}}_{x_2}$. It generates two outputs which are different combinations of two input signals. In this analysis, we only focus on y_1, which is given by

$$\hat{\mathbf{a}}_{y_1} = \sqrt{G}\hat{\mathbf{a}}_{x_1} + \sqrt{G-1}\hat{\mathbf{a}}^{\dagger}_{x_2} \tag{4.93}$$

Then, its number operator implemented by the photon detection at the output is

$$\hat{\mathbf{n}}_{y_1} = \hat{\mathbf{a}}^{\dagger}_{y_1}\hat{\mathbf{a}}_{y_1} = G\hat{\mathbf{a}}^{\dagger}_{x_1}\hat{\mathbf{a}}_{x_1} + (G-1)\hat{\mathbf{a}}_{x_2}\hat{\mathbf{a}}^{\dagger}_{x_2} + \sqrt{G(G-1)}(\hat{\mathbf{a}}^{\dagger}_{x_1}\hat{\mathbf{a}}^{\dagger}_{x_2} + \hat{\mathbf{a}}_{x_2}\hat{\mathbf{a}}_{x_1}) \tag{4.94}$$

If the two inputs are uncorrelated, the cross terms in the above equation are zero and the mean number of photons at this output is given by

$$\langle\hat{\mathbf{n}}_{y_1}\rangle = \langle\hat{\mathbf{a}}^{\dagger}_{y_1}\hat{\mathbf{a}}_{y_1}\rangle = G\,\langle\hat{\mathbf{a}}^{\dagger}_{x_1}\hat{\mathbf{a}}_{x_1}\rangle + (G-1)\,\langle\hat{\mathbf{a}}_{x_2}\hat{\mathbf{a}}^{\dagger}_{x_2}\rangle \tag{4.95}$$

Let the mean numbers of photons of two inputs be $\langle\hat{\mathbf{n}}_{x_1}\rangle = \langle\hat{\mathbf{a}}^{\dagger}_{x_1}\hat{\mathbf{a}}_{x_1}\rangle = m_1$ and $\langle\hat{\mathbf{n}}_{x_2}\rangle = \langle\hat{\mathbf{a}}^{\dagger}_{x_2}\hat{\mathbf{a}}_{x_2}\rangle = m_2$. Then, as $[\hat{\mathbf{a}}, \hat{\mathbf{a}}^{\dagger}] = 1$, $\hat{\mathbf{a}}\hat{\mathbf{a}}^{\dagger} = 1 + \hat{\mathbf{a}}^{\dagger}\hat{\mathbf{a}}$, the mean number of photons at the OPA output is $\langle\hat{\mathbf{n}}_{y_1}\rangle = Gm_1 + (G-1)(1+m_2)$. This output includes the two amplified inputs and the noise added by the OPA represented by $(G-1)$. The variance of this output is given by

$$\sigma^2 = \langle\delta n^2_{y_1}\rangle = \langle\hat{\mathbf{n}}^2_{y_1}\rangle - \langle\hat{\mathbf{n}}_{y_1}\rangle^2 \tag{4.96}$$

where, from Eq. (4.95), we have

$$\begin{aligned}\langle \hat{\mathbf{n}}_{y_1}^2 \rangle = G^2 \langle \hat{\mathbf{n}}_{x_1}^2 \rangle + (G-1)^2(1 + 2\langle \hat{\mathbf{n}}_{x_2} \rangle + \langle \hat{\mathbf{n}}_{x_2}^2 \rangle) \\ + G(G-1)(\langle \hat{\mathbf{n}}_{x_1}\hat{\mathbf{n}}_{x_2} \rangle + \langle \hat{\mathbf{n}}_{x_2}\hat{\mathbf{n}}_{x_1} \rangle + \langle (1+\hat{\mathbf{n}}_{x_1})(1+\hat{\mathbf{n}}_{x_2}) \rangle)\end{aligned} \tag{4.97}$$

and

$$\begin{aligned}\langle \hat{\mathbf{n}}_{y_1} \rangle^2 = G^2 \langle \hat{\mathbf{n}}_{x_1} \rangle^2 + (G-1)^2(1 + 2\langle \hat{\mathbf{n}}_{x_2} \rangle + \langle \hat{\mathbf{n}}_{x_2} \rangle^2) \\ + G(G-1)(\langle \hat{\mathbf{n}}_{x_1} \rangle \langle \hat{\mathbf{n}}_{x_2} \rangle + \langle \hat{\mathbf{n}}_{x_2} \rangle \langle \hat{\mathbf{n}}_{x_1} \rangle)\end{aligned} \tag{4.98}$$

Thus, the output variance is given by

$$\sigma^2 = G^2\sigma_{x_1}^2 + (G-1)^2\sigma_{x_2}^2 + G(G-1)(1 + m_1 + m_2 + m_1 m_2) \tag{4.99}$$

where $\sigma_{x_1}^2$ and $\sigma_{x_2}^2$ denote the variance of two inputs: $\sigma_{x_1}^2 = \langle \hat{\mathbf{n}}_{x_1}^2 \rangle - \langle \hat{\mathbf{n}}_{x_1} \rangle^2$ and $\sigma_{x_2}^2 = \langle \hat{\mathbf{n}}_{x_2}^2 \rangle - \langle \hat{\mathbf{n}}_{x_2} \rangle^2$. As given by Eq.4.99, the variance of the output signal consists of amplified variances of two inputs and the additional term resulting from the parametric amplification process. Therefore, the use of an OPA not only adds additional noise photons to the output but also contributes to its variance.

If two inputs are correlated, the mean number of photons at this output is given by

$$\langle \hat{\mathbf{n}}_{y_1} \rangle = G \langle \hat{\mathbf{n}}_{x_1} \rangle + (G-1) \langle \hat{\mathbf{n}}_{x_2} + \hat{\mathbf{I}} \rangle + \sqrt{G(G-1)}(\langle \hat{\mathbf{a}}_{x_1}^\dagger \hat{\mathbf{a}}_{x_2}^\dagger \rangle + \langle \hat{\mathbf{a}}_{x_2} \hat{\mathbf{a}}_{x_1} \rangle) \tag{4.100}$$

And the variance is given by

$$\begin{aligned}
\sigma^2 &= G^2\sigma_{x_1}^2 + G(G-1)\sigma_{x_2}^2 + G(G-1)(1+m_1+m_2+m_1m_2 \\
&= G(G-1)[\langle \hat{\mathbf{a}}_{x_1}^{\dagger^2}\hat{\mathbf{a}}_{x_2}^{\dagger^2}\rangle - \langle \hat{\mathbf{a}}_{x_1}^{\dagger}\hat{\mathbf{a}}_{x_2}^{\dagger}\rangle^2 + \langle \hat{\mathbf{a}}_{x_2}^{2}\hat{\mathbf{a}}_{x_1}^{2}\rangle - \langle \hat{\mathbf{a}}_{x_2}\hat{\mathbf{a}}_{x_1}\rangle^2] \\
&= G\sqrt{G(G-1)}[\langle \hat{\mathbf{a}}_{x_1}^{\dagger}\hat{\mathbf{a}}_{x_1}\hat{\mathbf{a}}_{x_1}^{\dagger}\hat{\mathbf{a}}_{x_2}^{\dagger}\rangle + \langle \hat{\mathbf{a}}_{x_1}^{\dagger}\hat{\mathbf{a}}_{x_2}^{\dagger}\hat{\mathbf{a}}_{x_1}^{\dagger}\hat{\mathbf{a}}_{x_1}\rangle - 2m_1\langle \hat{\mathbf{a}}_{x_1}^{\dagger}\hat{\mathbf{a}}_{x_2}^{\dagger}\rangle] \\
&= G\sqrt{G(G-1)}[\langle \hat{\mathbf{a}}_{x_1}^{\dagger}\hat{\mathbf{a}}_{x_1}\hat{\mathbf{a}}_{x_2}\hat{\mathbf{a}}_{x_1}\rangle + \langle \hat{\mathbf{a}}_{x_2}\hat{\mathbf{a}}_{x_1}\hat{\mathbf{a}}_{x_1}^{\dagger}\hat{\mathbf{a}}_{x_1}\rangle - 2m_1\langle \hat{\mathbf{a}}_{x_2}\hat{\mathbf{a}}_{x_1}\rangle] \\
&= (G-1)\sqrt{G(G-1)}[\langle \hat{\mathbf{a}}_{x_2}\hat{\mathbf{a}}_{x_2}^{\dagger}\hat{\mathbf{a}}_{x_1}^{\dagger}\hat{\mathbf{a}}_{x_2}^{\dagger}\rangle + \langle \hat{\mathbf{a}}_{x_1}^{\dagger}\hat{\mathbf{a}}_{x_2}^{\dagger}\hat{\mathbf{a}}_{x_2}\hat{\mathbf{a}}_{x_2}^{\dagger}\rangle - 2m_1\langle \hat{\mathbf{a}}_{x_1}^{\dagger}\hat{\mathbf{a}}_{x_2}^{\dagger}\rangle] \\
&= (G-1)\sqrt{G(G-1)}[\langle \hat{\mathbf{a}}_{x_2}\hat{\mathbf{a}}_{x_2}^{\dagger}\hat{\mathbf{a}}_{x_2}\hat{\mathbf{a}}_{x_1}\rangle + \langle \hat{\mathbf{a}}_{x_2}\hat{\mathbf{a}}_{x_1}\hat{\mathbf{a}}_{x_2}\hat{\mathbf{a}}_{x_2}^{\dagger}\rangle - 2m_1\langle \hat{\mathbf{a}}_{x_2}\hat{\mathbf{a}}_{x_1}\rangle]
\end{aligned} \tag{4.101}$$

The OPA is a nonlinear optical device, which can modify the statistical properties of the light it amplifies. If the signal to be amplified exhibits squeezing property such as the SPDC output, this feature can be lost after amplification when the gain is too high. The limit of the power gain which can preserve the non-classical property in the signal has been derived [60], and the recommended maximum gain for the OPA is 2. Thus, in the quantum detector proposed in the following, we choose $G < 2$.

4.4 Double-OPA Detection Design

Inspection of the one-OPA design reveals that both the mean and variance of the OPA output depend on the intensity of the two inputs. Thus, we may find an optimum combination of the two inputs arriving at an output having a minimum detection error. This leads us to the consideration of a new *double OPA detector*. The optimum design and its detection performance analysis are presented in this section. We first propose to pre-process the idler before mixing it with the received signal beam. This

leads to the configuration of a two-OPA photon counting detector as shown in Fig.4.5.

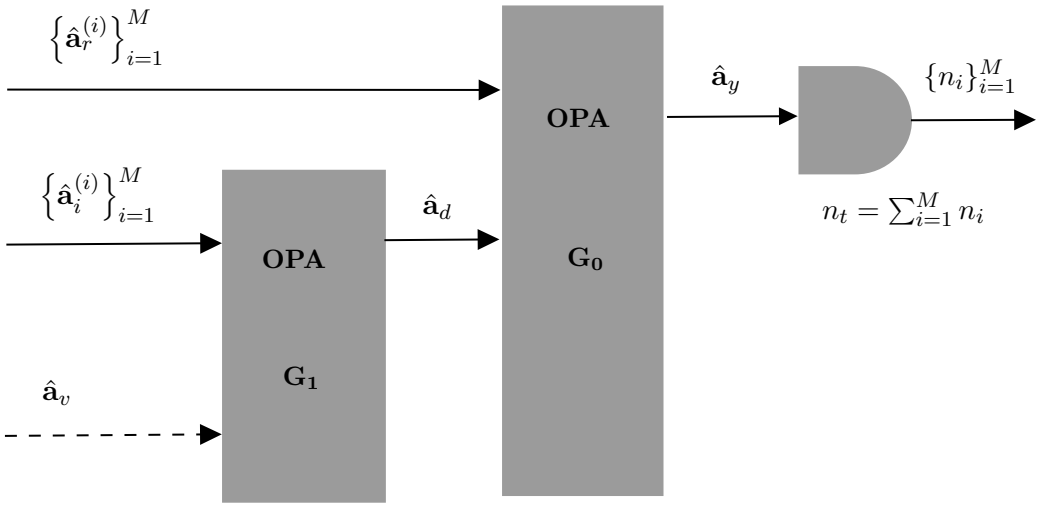

Figure 4.5: A schematic diagram of the proposed dual-OPA detector design. It consists of two OPAs with different gain and one photon counter

Here, the first OPA with gain G_1 takes on two inputs, the idler beam $\hat{\mathbf{a}}_i$ and the vacuum beam $\hat{\mathbf{a}}_v$, producing an output

$$\hat{\mathbf{a}}_d = \sqrt{G_1}\hat{\mathbf{a}}_i + \sqrt{G_1 - 1}\hat{\mathbf{a}}_v^{\dagger} \tag{4.102}$$

This output is then passed to the second OPA having gain G_0, and together with the received beam, $\hat{\mathbf{a}}_r$, form the output

$$\hat{\mathbf{a}}_y = \sqrt{G_1 G_0}\hat{\mathbf{a}}_i + \sqrt{G_0(G_1 - 1)}\hat{\mathbf{a}}_v^{\dagger} + \sqrt{G_0 - 1}\hat{\mathbf{a}}_r^{\dagger} \tag{4.103}$$

where $\hat{\mathbf{a}}_y$ denotes the output of the two-OPA detector. A photon counter is placed at

this output to measure the number of photons giving

$$\begin{aligned}\hat{\mathbf{n}}_y &= \hat{\mathbf{a}}_y^\dagger \hat{\mathbf{a}}_y \\ &= G_1G_0\hat{\mathbf{a}}_i^\dagger\hat{\mathbf{a}}_i + (G_0-1)\hat{\mathbf{a}}_r\hat{\mathbf{a}}_r^\dagger + \sqrt{G_1G_0(G_0-1)}(\hat{\mathbf{a}}_i^\dagger\hat{\mathbf{a}}_r + \hat{\mathbf{a}}_i\hat{\mathbf{a}}_r^\dagger) + G_0(G_1-1)(\hat{\mathbf{a}}_v^\dagger\hat{\mathbf{a}}_v+1) \\ &+ G_0\sqrt{G_1(G_1-1)}(\hat{\mathbf{a}}_i^\dagger\hat{\mathbf{a}}_v^\dagger + \hat{\mathbf{a}}_v\hat{\mathbf{a}}_i) + \sqrt{G_0(G_0-1)(G_1-1)}(\hat{\mathbf{a}}_v\hat{\mathbf{a}}_r^\dagger + \hat{\mathbf{a}}_r\hat{\mathbf{a}}_v^\dagger) \\ &= G_1G_0\hat{\mathbf{a}}_i^\dagger\hat{\mathbf{a}}_i + (G_0-1)\hat{\mathbf{a}}_r\hat{\mathbf{a}}_r^\dagger + \sqrt{G_1G_0(G_0-1)}(\hat{\mathbf{a}}_i^\dagger\hat{\mathbf{a}}_r + \hat{\mathbf{a}}_i\hat{\mathbf{a}}_r^\dagger) + G_0(G_1-1)\end{aligned} \tag{4.104}$$

The result in the last step of Eq.4.104 is because of the fact that $\langle\hat{\mathbf{a}}_v^\dagger\hat{\mathbf{a}}_v\rangle = 0$ and other terms involving $\hat{\mathbf{a}}_v$ or $\hat{\mathbf{a}}_v^\dagger$ which yields zero as well. The photon number $\langle\hat{\mathbf{a}}_y^\dagger\hat{\mathbf{a}}_y\rangle$ is obtained by taking the average of $\hat{\mathbf{n}}_y$ in Eq.4.104.

For this two-OPA detector, the expected number of photons $N_j = \langle\hat{\mathbf{n}}_y\rangle$ under hypothesis $H_j, j = 0, 1$ are

$$N_0 = G_1G_0N_S + (G_0-1)(1+N_B) + G_0(G_1-1) \tag{4.105a}$$

$$N_1 = G_1G_0N_S + (G_0-1)(1+N_B+\eta N_S) + 2\sqrt{G_1G_0(G_0-1)}\sqrt{\eta N_S(N_S+1)} + G_0(G_1-1) \tag{4.105b}$$

The variance under each hypothesis can be calculated using Eq.4.96. Under H_0, the variance is

$$\sigma_0^2 \approx G_1^2G_0^2N_S(N_S+1) + (G_0-1)^2N_B(N_B+1) + G_1G_0(G_0-1)(1+N_B+N_S+2N_BN_S) \tag{4.106}$$

where the first two terms come from variances of two input signals and the third term originates from the OPA process. since $\hat{\mathbf{a}}_r$ includes $\hat{\mathbf{a}}_b$ and $\hat{\mathbf{a}}_r$ has to satisfy the commutation relationship $[\hat{\mathbf{a}}_r, \hat{\mathbf{a}}_r^\dagger] = 1$, then, a coefficient $\sqrt{1-\eta}$ has been added to

$\hat{\mathbf{a}}_b$ and correspondingly, the averaged noise photon number becomes $\frac{N_B}{1-\eta}$. Here, the approximation sign ($\approx$) used in Eq.4.106 and Eq.4.107 is because when $\eta \ll 1$, $\frac{N_B}{1-\eta}$ is approximated by N_B.

Similarly, under H_1, the variance can be derived and is given by

$$\begin{aligned}\sigma_1^2 \approx\ & G_1^2 G_0^2 N_S(N_S+1) + (G_0-1)^2(N_B^2+N_B+\eta N_B) \\ & + G_0 G_1 (G_0-1)(1+N_B+N_S+2N_S N_B) \\ & + (G_0-1)(1+2N_B)\sqrt{G_0 G_1 (G_0-1)}\sqrt{\eta N_S(N_S+1)} \\ & + G_1 G_0 (4N_S+3)\sqrt{G_0 G_1 (G_0-1)}\sqrt{\eta N_S(N_S+1)}\end{aligned} \tag{4.107}$$

The first two terms are the amplified input variances. The OPA process contributes to the third term. The last two terms are related to the entangled relationship between two input signals.

Then, at each trial, the measured result of the output is noted and the averaged result over M trials is used as the test statistics. When the number of trials, M is sufficiently large, the distribution of the mean number of photons detected at this output, n_t can be approximated as a Gaussian distribution with above mean N_i and variance σ_i^2/M due to the Central Limit Theorem. If the detection threshold N_{th} is pre-determined, the probability of false alarm and probability of missing are

$$P_{\text{F}} = \int_{N_{\text{th}}}^{\infty} p(n_{\text{t}}|H_0)dn_{\text{t}} = \frac{1}{2}\text{erfc}\Big(\frac{N_{\text{th}}-N_0}{\sqrt{2/M}\sigma_0}\Big) \tag{4.108a}$$

$$P_{\text{M}} = \int_{-\infty}^{N_{\text{th}}} p(n_{\text{t}}|H_1)dn_{\text{t}} = 1 - \frac{1}{2}\text{erfc}\Big(\frac{N_{\text{th}}-N_1}{\sqrt{2/M}\sigma_1}\Big) \tag{4.108b}$$

4.4.1 Minimum Probability of Error Criterion

The detector in radar systems can be designed to minimize the total probability of error. Without any prior information about the target presence, it is assumed that

$$P(H_0) = P(H_1) = \frac{1}{2} \tag{4.109}$$

Then, the probability of error becomes

$$P_e = \frac{1}{2}(P_F + P_M) \tag{4.110}$$

where P_F and P_M are given in Eqs. 4.108. The minimum probability of error in this case can be achieved when the threshold is chosen to be the cross-over point of $p(n_t|H_0)$ and $p(n_t|H_1)$:

$$N_{\text{th}} \approx \frac{\sigma_1 N_0 + \sigma_0 N_1}{\sigma_0 + \sigma_1} \tag{4.111}$$

where this approximation comes from the approximation $\ln(\sigma_0/\sigma_1) \approx 0$. Then, the minimum probability of error is

$$P_e = \frac{1}{2}\text{erfc}\Big[\sqrt{\frac{M(N_1 - N_0)^2}{2(\sigma_0 + \sigma_1)^2}}\Big] \tag{4.112}$$

As N_i, σ_i are all dependent on G_0 and G_1, the minimum probability of error can be further optimized with respect to G_0 and G_1. Optimal G_0 and G_1 are given by calculating

$$\frac{\partial P_e}{\partial G_0}\Big|_{G_{0\text{opt}}} = 0, \quad \frac{\partial P_e}{\partial G_1}\Big|_{G_{1\text{opt}}} = 0 \tag{4.113}$$

If the solution is found by locating the optimum value of Eq. (4.113), because there is no constraints on values of G_0 and G_1, it is called as an *unconstrained optimum design*. However, since the gain of the OPA should not exceed 2 for the preservation of entanglement [60], a constraint is put on gains of both OPAs such that $G_0 < 2$ and $G_1 < 2$. An optimum solution under this constraint of the gains is called a *constrained optimum design*. The performance of both constrained and unconstrained optimum designs of the 2-OPA detectors is evaluated in the following section.

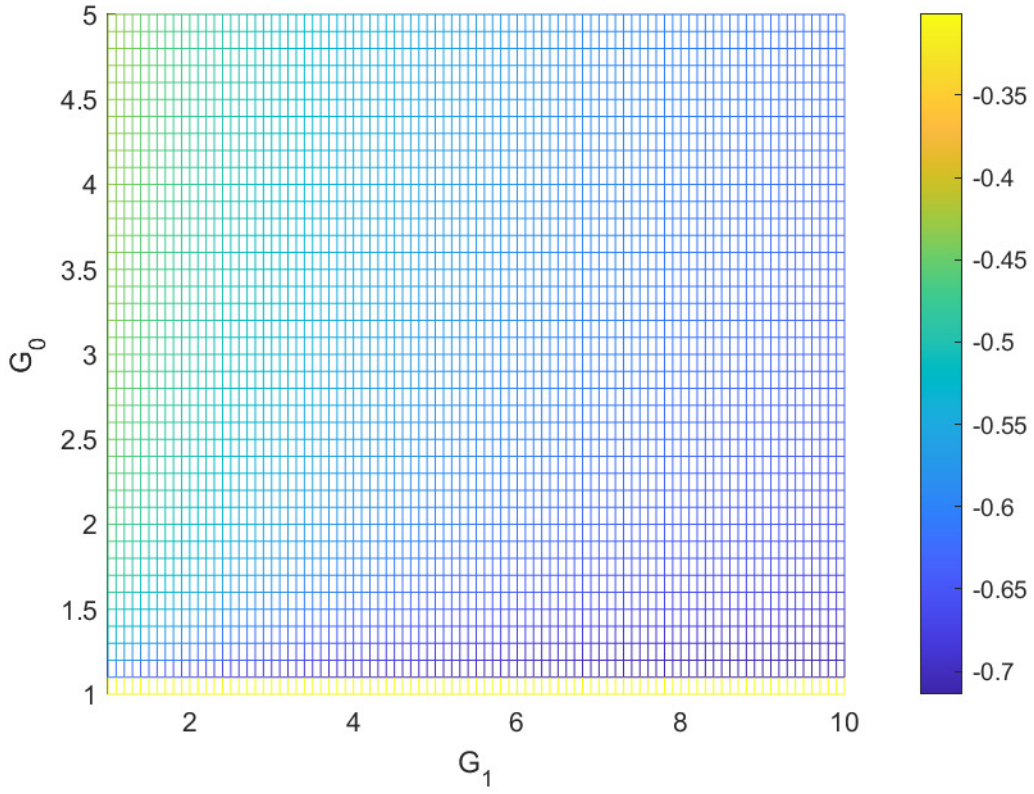

(1) *Unconstrained Optimum Solution*: – Closed-form solutions of Eq.(4.113) are very difficult to obtain. We obtain the optimal solution by exhaustive numerical search. Figure shows the log of the probability of error of the detector at different values

of G_0 and G_1. This figure is plotted with given values of $N_B = 10, N_S = 0.01, \eta = 0.01, M = 10^6$, and there is no constraint on G_0 and G_1. Here, we locate the optimum values of OPA gains to be $G_0 = 1.1, G_1 = 8.5$. Compare this value with the one-OPA design ($G_1 = 1$ case) in which the optimal value of G_0 is 1.1.

(2) *Constrained Optimum Solution*: – In [60], it has been demonstrated that there is substantial loss in the entanglement between the signal and idler when the gain is equal to or higher than 2. This places a constraint on gains of both OPAs such that $G_0 < 2$ and $G_1 < 2$. Following these gain constraints and performing an exhaustive numerical search using numerical values of $N_B = 10, N_S = 0.01, \eta = 0.01, M = 10^6$, the constrained optimum gains for the two OPAs are $G_0 = 1.1$ and $G_1 = 1.9$.

Numerical Results

The probability distributions $p(n_t|H_j)$ for this set of parameters are shown in Fig.4.6(a) of one-OPA detector and in Fig.4.6(b) of unconstrained two-OPA detector, in Fig.4.6(c) of constrained 2-OPA detector.

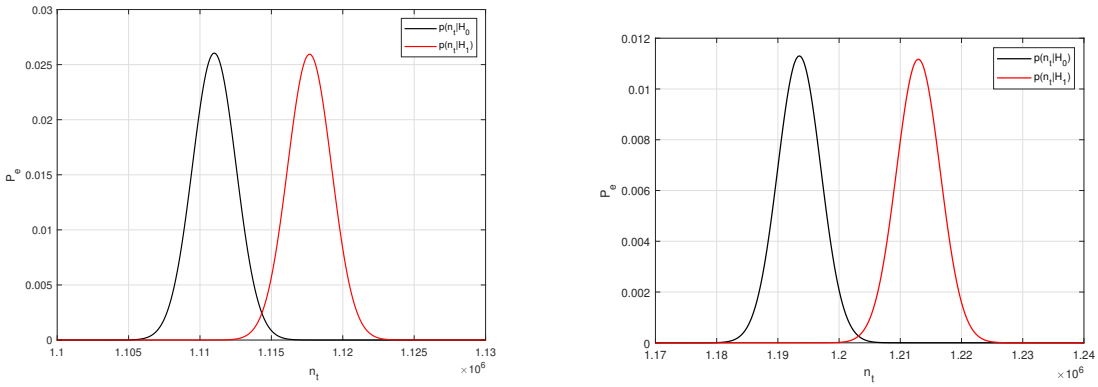

(a) one-OPA (b) unconstrained two-OPA

Figure 4.6: The probability distributions $p(n_t|H_0)$ and $p(n_t|H_1)$ with $M = 10^6$

From Fig.4.6, it can be observed that $p(n_t|H_0)$ and $p(n_t|H_1)$ are separated farther in the unconstrained 2-OPA detector than those of 1-OPA design. In the 2-OPA detector design, the overlap between two distributions is significantly smaller thsn that for the 1-OPA detector. Therefore, the detector using two OPAs is expected to achieve a lower probability of error than the 1-OPA detector.

Minimum Error Probability with M

The minimum error probability as defined in Eq.4.112 is dependent on the number of trials M. The numerical result given by Eq.4.112 is obtained for these three designs of detectors: (i) optimum 1-OPA design, (ii) optimum constrained 2-OPA design, and (iii) optimum unconstrained 2-OPA design as shown in Fig.4.7

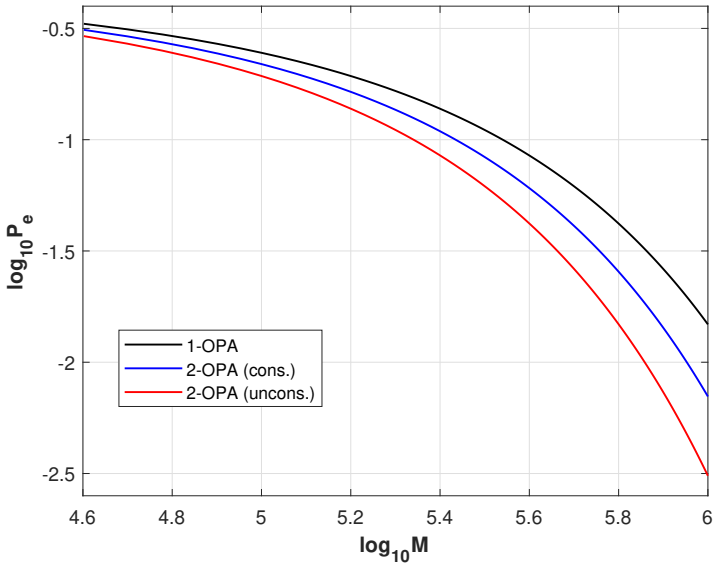

Figure 4.7: The probabilities of error for different M of one-OPA and 2 two-OPA detectors

Fig.4.7 shows that when M is relatively small, say, at $4 \times 10^4 (\log_{10} M = 4.602)$, the probability of error of 1-OPA design is 33.17% ($\log_{10} P_e = -0.48$). At this point, the two-OPA detector achieves 29% ($\log_{10} P_e = -0.535$) error probability, which outperforms the previous design significantly and makes this detector design desirable as a radar system.

When M increases from 4×10^4 to a larger value, say, $M = 10^6$, the error probabilities of both detectors decrease. The probability of error of one-OPA design decreases gradually from 33% to 1.6% ($\log_{10} P_e = -1.78$). There is a sharp reduction in the error probability of two-OPA design from 29% to 0.32% ($\log_{10} P_e = -2.51$).

From this plot, it can be concluded that the number of independent trials required to achieve the same error probability can be largely reduced when two-OPA detector

design is employed. At a given M, the error probability achieved by the two-OPA design is much lower than that of one-OPA design.

The result in Fig.4.7 provides the approximated theoretical minimum error probability. For the practical simulation results without approximation, the performance of these three detectors is shown in Fig.4.8. In this case, the weak signal is immersed in the bright noisy background, $N_s = 0.01, N_b = 10, \eta = 0.01$

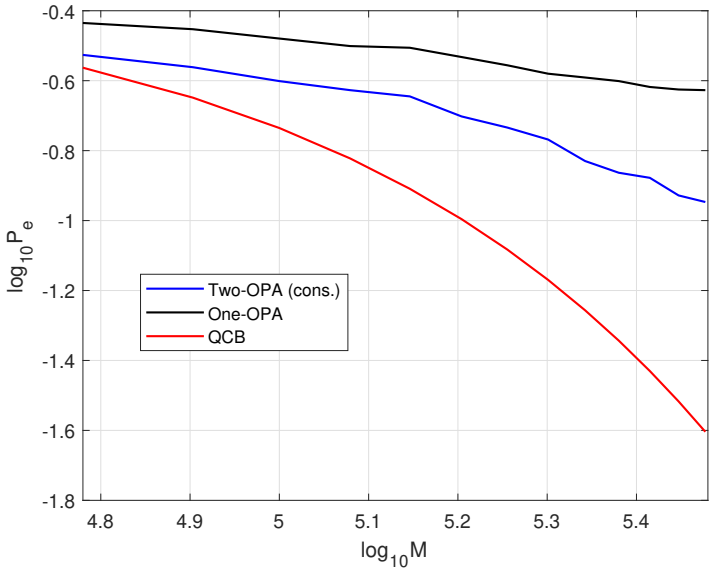

Figure 4.8: The numerical simulation of the one-OPA detector and the dual-OPA with the linearity constraint in comparison with the theoretical QCB.

For a clearer comparison, the following table includes the probability of error for two detectors at different values of M.

	$M = 10^5$	$M = 3 * 10^5$
1-OPA	0.3315	0.236
2-OPA	0.2505	0.113
QCB	0.1839	0.025

Table 4.1: The minimum probability of error for two OPA detectors

The advantage of the 2-OPA detector over 1-OPA is still obvious in the practical simulation.

4.4.2 Neynman-Pearson Criterion

In many practical cases, the target is unknown and therefore, the returned signal under H_1 is unknown. An important detection strategy to overcome this difficulty is the *Neynman Pearson criterion*. This criterion involves a likelihood ratio test

$$\Gamma(n_t) = \frac{p(n_t|H_1)}{p(n_t|H_0)} \underset{H_0}{\overset{H_1}{\gtrless}} \xi$$

It is only the value of the threshold with which this ratio is compared that varies with the criterion. The performance of the test can be completely specified by a graph with the probability of detection, P_D against the probability of false alarm, P_F. Such a graph is called the *receiver operating characteristic* (ROC). It depends only on the probability density function of the observations under two hypotheses, $p(n_t|H_0), p(n_t|H_1)$.

Using this criterion, the detector is designed so that the probability of false alarm is constrained to be less than a fixed value α while the probability of detection is maximised. Then, varying the value of α, the performance of the detector can be plotted as the *receiver operating characteristic* (ROC) curve, which displays the probability of detection achieved at different probabilities of false alarm ranging from 0 to 1.

The performance of one-OPA and two-OPA detector designs is investigated. The system parameters in this performance comparison (Fig.4.9) are chosen as $M = 10^5, N_s = 0.01, N_b = 10, \eta = 0.01$ in .

For the distributions $p(n_t|H_i)$, its variance var=σ_i^2/M decreases as M increases. Thus, the overlapping area between two distributions becomes smaller and the error probability is correspondingly reduced.

When the acceptable probability of false alarm is below 0.2, the highest probability of detection achieved by one-OPA detector is around 70.4% while 81.3% is achievable for unconstrained two-OPA detector design and 76.2% for the constrained two-OPA design.

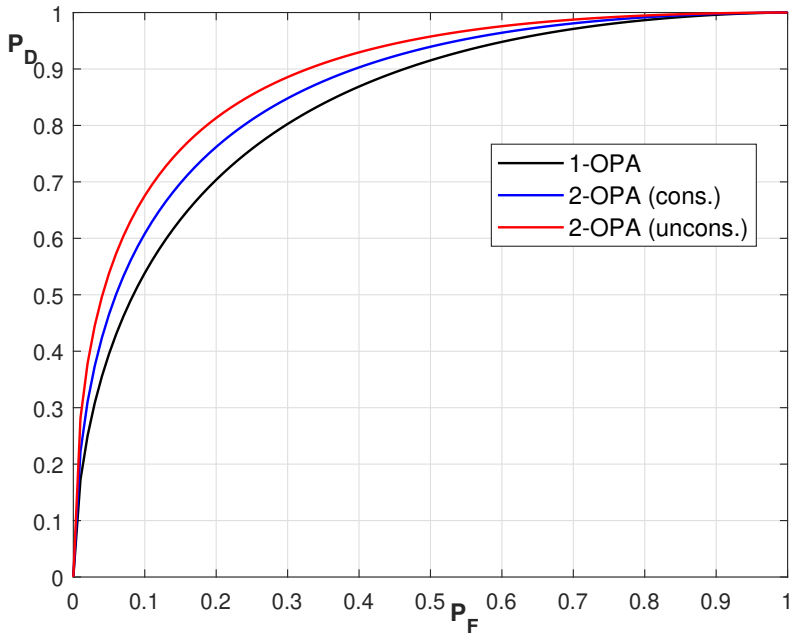

Figure 4.9: ROC of one-OPA and two-OPA detector designs with $M = 10^5$

Fig.4.10 shows the improvement of the probability of detection as a function of P_{F}. It plots the difference between P_D of the 2-OPA with linearity constraint and 1-OPA. We can observe an enhancement at any probability of false alarm. The maximum enhancement is about 7.11% at $P_F = 0.07$.

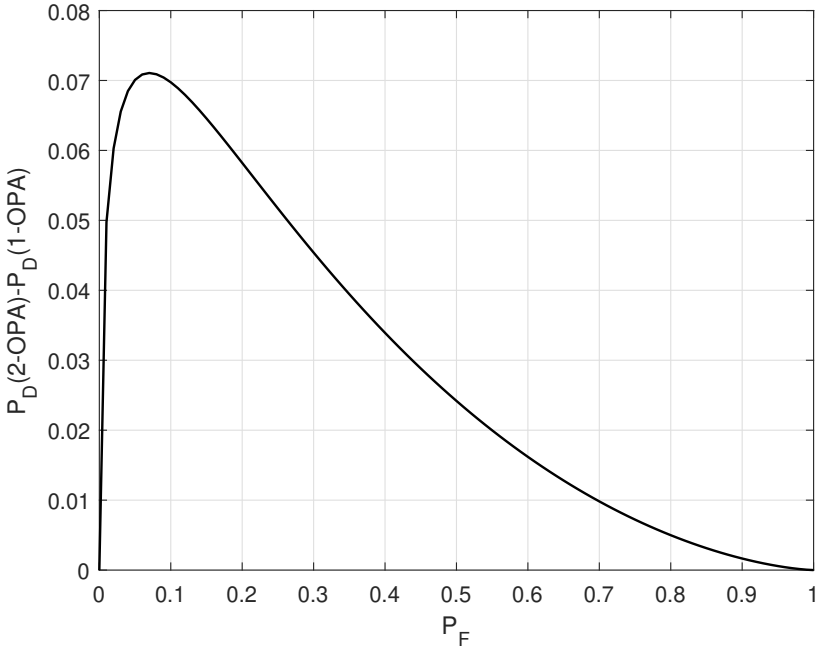

Figure 4.10: The difference between the probabilities of detection of two-OPA and one-OPA detectors as a function of probability of false alarm

Variation of Receiver Performance with M

The performance of detection designs in ROC plots is investigated at three number of trials, $M = 5 \times 10^4, 10^5, 2 \times 10^5$ as shown in Fig.4.11.

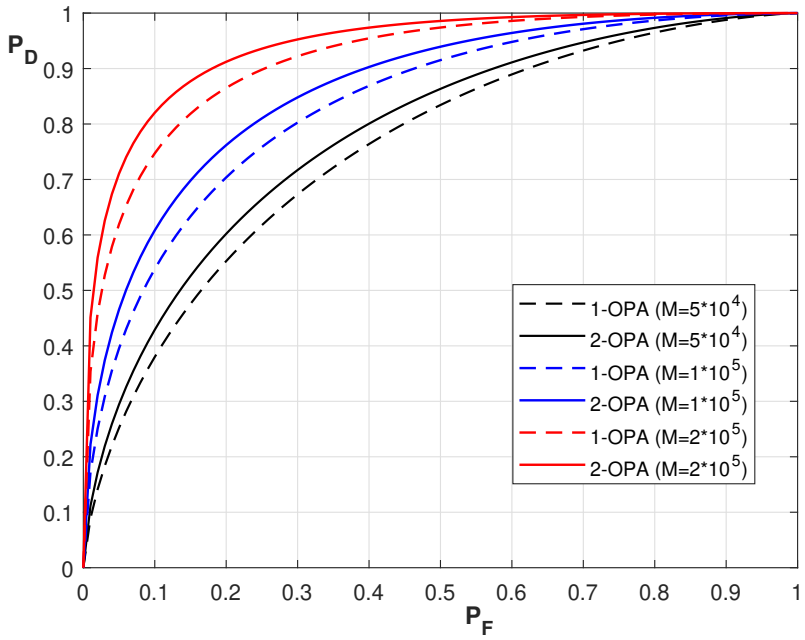

Figure 4.11: Receiving operating characteristics of one-OPA and two-OPA detectors with M=$5 \cdot 10^4$ and $M = 10^5$

In Fig.4.11, it compares the performance of the one-OPA and constrained two-OPA detector designs. At any value of M, the two-OPA detector achieves better performance than the one-OPA design. Moreover, when M increases, the advantage of the 2-OPA over 1-OPA becomes more obvious. Table 4.2 shows the probability of detection of two detectors at three different M when the probability of false alarm is fixed at 0.05.

	M=$5 * 10^4$	M=$1 * 10^5$	M=$2 * 10^5$
1-OPA	0.25	0.40	0.62
2-OPA	0.30	0.47	0.71

Table 4.2: The probability of detection of 1-OPA and 2-OPA designs at $M = 5 * 10^4, 10^5, 2 * 10^5$.

When M increases from $5 * 10^4$ to $2 * 10^5$, the improvement introduced by the 2-OPA design increases from 5% to 9%.

Detection Performance with N_B and η

The performance of detectors is dependent on the background noise level. When N_B increases, both N_0 and N_1 increases; however, the difference between them is unchanged. Moreover, σ_0 and σ_1^2 increases with N_B. Therefore, the performance of both OPA detectors deteriorates significantly when the environment becomes more noisy. However, the dual OPA detector achieves better detection performance at any noise level compared to that of the one-OPA detector.

Therefore, the ROC plots at three different noise intensities, $N_b = 5, 10, 15$ in Fig.4.12

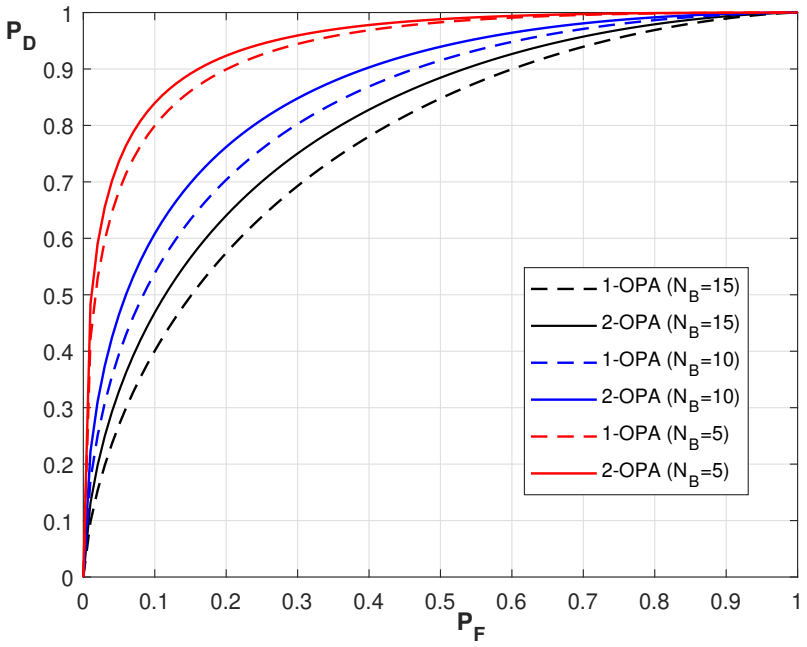

Figure 4.12: Receiving operating characteristics of one-OPA and two-OPA detectors with M=$5 \cdot 10^4$ and $M = 10^5$

Moreover, the mean and variance N_1, σ_1 are dependent on the system transmissivity η. From Eqs. 4.105, increasing η increases the difference between N_0 and N_1. σ_1^2 becomes more significant with an increasing value of η. Therefore, the system with a larger system transmissivity increases N_1 but sacrifices the variance. Compared with the impact of the noise level in the system performance, the impact of η is less significant. As shown in Fig.4.13, there is an improvement in the detection performance of OPA detectors when η increases.

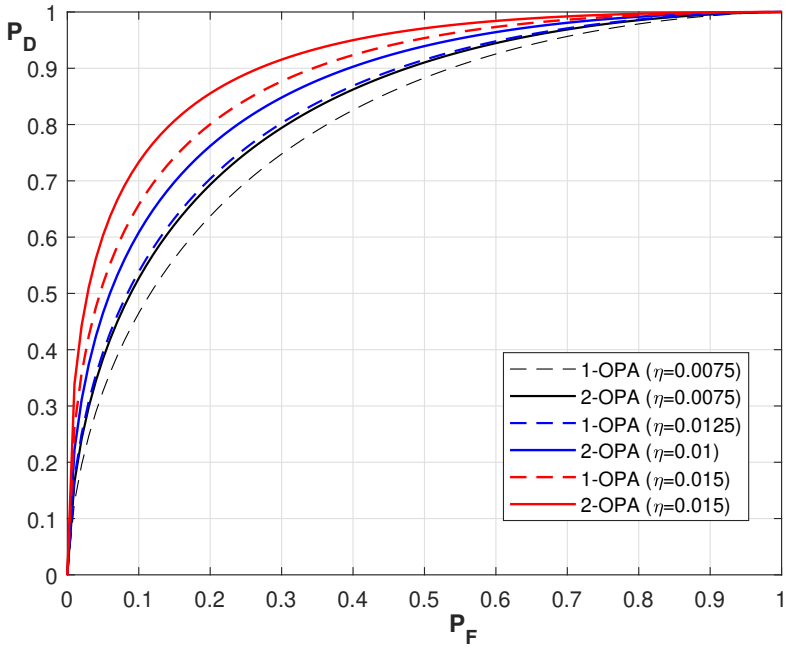

Figure 4.13: Receiving operating characteristics of one-OPA and two-OPA detectors with M=$5 \cdot 10^4$ and $M = 10^5$

Moreover, the dual OPA detector at any value of η achieves a higher probability of detection than that of one-OPA detector.

4.5 Quantum Detection - Covariance Matrix

The bipartite (entangled) states of two modes of the radiation field are employed in Quantum Illumination. If the SPDC process is considered as the major source of signal generation, its output as a Gaussian state will be considered which the mean and covariance matrix can be completely characterize by its mean and covariance matrix. Besides the mean values of the quadrature operators $\hat{\mathbf{x}}, \hat{\mathbf{p}}$ which the OPA detection

design relies on, the most relevant quantity needed to characterize a bipartite state is its covariance matrix. Therefore, it is suggested to investigate the use of the covariance matrix between the return signal and idler under each hypothesis in the Quantum Illumination. Here, a theoretical analysis of this method is presented and the method of construction of the covariance matrix is included. The performance of the detector with covariance matrix is compared with two OPA detectors.

4.5.1 Theoretical Analysis

The SPDC output is a zero-mean Gaussian state whose Wigner distribution takes the form

$$p(\mathbf{v}) = \frac{1}{\sqrt{(2\pi)^4 |\mathbf{\Gamma}^q|}} \exp\Big[-\frac{1}{2}\mathbf{v}^T (\mathbf{\Gamma}^q)^{-1}\mathbf{v}\Big] \tag{4.114}$$

where $\mathbf{v} = (x_s, p_s, x_i, p_i)$ is a vector of Cartesian coordinates of signal and idler systems.

The covariance matrix of a two mode state is a real symmetric positive matrix defined as follows

$$\mathbf{\Gamma}^q = \begin{bmatrix} \Delta\hat{\mathbf{v}}_1^2 & \Delta\hat{\mathbf{v}}_1\hat{\mathbf{v}}_2 & \Delta\hat{\mathbf{v}}_1\hat{\mathbf{v}}_3 & \Delta\hat{\mathbf{v}}_1\hat{\mathbf{v}}_4 \\ \Delta\hat{\mathbf{v}}_2\hat{\mathbf{v}}_1 & \Delta\hat{\mathbf{v}}_2^2 & \Delta\hat{\mathbf{v}}_2\hat{\mathbf{v}}_3 & \Delta\hat{\mathbf{v}}_2\hat{\mathbf{v}}_4 \\ \Delta\hat{\mathbf{v}}_3\hat{\mathbf{v}}_1 & \Delta\hat{\mathbf{v}}_3\hat{\mathbf{v}}_2 & \Delta\hat{\mathbf{v}}_3^2 & \Delta\hat{\mathbf{v}}_3\hat{\mathbf{v}}_4 \\ \Delta\hat{\mathbf{v}}_4\hat{\mathbf{v}}_1 & \Delta\hat{\mathbf{v}}_4\hat{\mathbf{v}}_2 & \Delta\hat{\mathbf{v}}_4\hat{\mathbf{v}}_3 & \Delta\hat{\mathbf{v}}_4^2 \end{bmatrix} \tag{4.115}$$

where $\hat{\mathbf{v}} = (\hat{\mathbf{x}}_s, \hat{\mathbf{p}}_s, \hat{\mathbf{x}}_i, \hat{\mathbf{p}}_i)$ is a vector of quadrature operators. $\Delta\hat{\mathbf{v}}_i^2 = \langle\hat{\mathbf{v}}_i^2\rangle - \langle\hat{\mathbf{v}}_i\rangle^2$ and $\Delta\hat{\mathbf{v}}_i\hat{\mathbf{v}}_j = \frac{1}{2}\langle\hat{\mathbf{v}}_i\hat{\mathbf{v}}_j + \hat{\mathbf{v}}_j\hat{\mathbf{v}}_i\rangle - \langle\hat{\mathbf{v}}_i\rangle\langle\hat{\mathbf{v}}_j\rangle, i \neq j$.

For the SPDC output, its Wigner-distribution covariance matrix between the initial

signal and idler beams can be obtained using the Eq.4.115

$$\mathbf{\Gamma}^q = \frac{1}{4}\begin{bmatrix} 2N_S+1 & 0 & 2\sqrt{N_S(N_S+1)} & 0 \\ 0 & 2N_S+1 & 0 & -2\sqrt{N_S(N_S+1)} \\ 2\sqrt{N_S(N_S+1)} & 0 & 2N_S+1 & 0 \\ 0 & -2\sqrt{N_S(N_S+1)} & 0 & 2N_S+1 \end{bmatrix} \tag{4.116}$$

The covariance matrix between the return signal and idler beams under each hypothesis becomes

$$\mathbf{\Gamma}_0^q = \frac{1}{4}\begin{bmatrix} 2N_B+1 & 0 & 0 & 0 \\ 0 & 2N_B+1 & 0 & 0 \\ 0 & 0 & 2N_S+1 & 0 \\ 0 & 0 & 0 & 2N_S+1 \end{bmatrix} \tag{4.117}$$

And

$$\mathbf{\Gamma}_1^q = \frac{1}{4}\begin{bmatrix} 2(\eta N_S+N_B)+1 & 0 & 2\sqrt{\eta N_S(N_S+1)} & 0 \\ 0 & 2(\eta N_S+N_B)+1 & 0 & -2\sqrt{\eta N_S(N_S+1)} \\ 2\sqrt{\eta N_S(N_S+1)} & 0 & 2N_S+1 & 0 \\ 0 & -2\sqrt{\eta N_S(N_S+1)} & 0 & 2N_S+1 \end{bmatrix} \tag{4.118}$$

It can be observed that the difference between two covariance matrices is significant. Therefore, the covariance matrix provides more information than the measured output intensity.

Every element in the covariance matrix requires the calculation of the expectation value of different operators with respect to the system state, $\langle \hat{\mathbf{X}} \rangle_\rho$. However, in reality,

getting these values needs numerous repeated computations.

Construction of Covariance Matrix

Reference [61] proposed the method of contruction of covariance matrix using a single homodyne detector and their results showed that this method is convenient and robust. The covariance matrix in Eq.4.115 consists of three parts

$$\mathbf{\Gamma}^q = \begin{bmatrix} \mathbf{A} & \mathbf{C} \\ \mathbf{C}^T & \mathbf{B} \end{bmatrix}$$

The construction of $\mathbf{A}$ and $\mathbf{B}$ relies on the measurement of the return signal and idler respectively. $\mathbf{C}$ requires the measurement of correlation relationship between the return signal and the idler. Diagonal elements in $\mathbf{A}$ correspond to the variance of $\hat{\mathbf{x}}_r$ and $\hat{\mathbf{p}}_r$ respectively. The measurement of $\hat{\mathbf{x}}$ is performed using a single homodyne detector.

Off diagonal elements in $\mathbf{A}$ are

$$a_{12} = a_{21} = \frac{1}{2}(\langle \hat{\mathbf{z}}_r^2 \rangle - \langle \hat{\mathbf{t}}_r^2 \rangle) - \langle \hat{\mathbf{x}}_r \rangle \langle \hat{\mathbf{p}}_r \rangle \tag{4.119}$$

where $\hat{\mathbf{z}}_r = \frac{\hat{\mathbf{x}}_r + \hat{\mathbf{p}}_r}{\sqrt{2}}$ and $\hat{\mathbf{t}}_r = \frac{\hat{\mathbf{x}}_r - \hat{\mathbf{p}}_r}{\sqrt{2}}$. For a single mode, indicated by Eq.(2.57), it is required to obtain values of x, p, t and z. These values can be obtained by a single homodyne detector with the systematic diagram shown in Fig.4.14

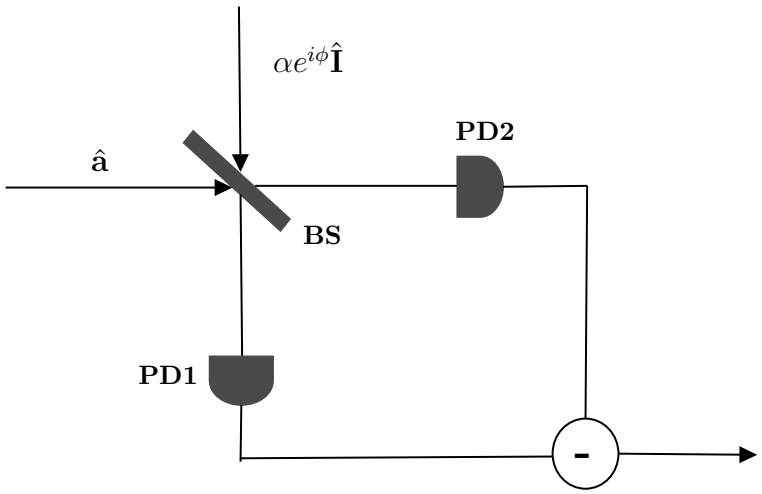

Figure 4.14: The schematic diagram of a homodyne detector

The interested mode, $\hat{\mathbf{a}}$ and a strong signal from the local oscillator $\alpha e^{i\phi}$ are fed into a 50:50 beamsplitter (BS). α denotes the magnitude of the local oscillator signal and ϕ represents the phase difference between $\hat{\mathbf{a}}$ and the local oscillator output. Two outputs from the BS are

$$\hat{\mathbf{c}}_1 = \frac{\hat{\mathbf{a}} + \alpha e^{i\phi}\hat{\mathbf{I}}}{\sqrt{2}} \tag{4.120a}$$

$$\hat{\mathbf{c}}_2 = \frac{\hat{\mathbf{a}} - \alpha e^{i\phi}\hat{\mathbf{I}}}{\sqrt{2}} \tag{4.120b}$$

One output $\hat{\mathbf{c}}_1$ is measured by the photodetector, PD1 and $\hat{\mathbf{c}}_2$ is fed into PD2.

$$\hat{\mathbf{c}}_1^\dagger\hat{\mathbf{c}}_1 = \frac{1}{2}(\hat{\mathbf{a}}^\dagger\hat{\mathbf{a}} + \alpha^2\hat{\mathbf{I}} + \alpha e^{i\phi}\hat{\mathbf{a}}^\dagger + \alpha e^{-i\phi}\hat{\mathbf{a}}) \tag{4.121a}$$

$$\hat{\mathbf{c}}_2^\dagger\hat{\mathbf{c}}_2 = \frac{1}{2}(\hat{\mathbf{a}}^\dagger\hat{\mathbf{a}} + \alpha^2\hat{\mathbf{I}} - \alpha e^{i\phi}\hat{\mathbf{a}}^\dagger - \alpha e^{-i\phi}\hat{\mathbf{a}}) \tag{4.121b}$$

The difference between outputs of two photodetectors becomes

$$\hat{\mathbf{s}} = \hat{\mathbf{c}}_1^\dagger \hat{\mathbf{c}}_1 - \hat{\mathbf{c}}_2^\dagger \hat{\mathbf{c}}_2 = \alpha e^{i\phi}\hat{\mathbf{a}}^\dagger + \alpha e^{-i\phi}\hat{\mathbf{a}} = \sqrt{2}\alpha \frac{e^{i\phi}\hat{\mathbf{a}}^\dagger + e^{-i\phi}\hat{\mathbf{a}}}{\sqrt{2}}$$

Then, with the knowledge of amplitude of local oscillator output α, the output can be normalized to

$$\hat{\mathbf{s}}' = \frac{e^{i\phi}\hat{\mathbf{a}}^\dagger + e^{-i\phi}\hat{\mathbf{a}}}{\sqrt{2}} \tag{4.122}$$

where for different values of ϕ, it becomes

$$\hat{\mathbf{s}}' = \begin{cases} \hat{\mathbf{x}}, & \phi = 0 \\ \hat{\mathbf{p}}, & \phi = \pi/2 \\ \hat{\mathbf{z}}, & \phi = \pi/4 \\ \hat{\mathbf{t}}, & \phi = -\pi/4 \end{cases}$$

Therefore, different parameters can be measured by adjusting the phase angle of the local oscillator.

In the construction of the covariance matrix, six different modes are of interest. First group are the return signal and idler modes with their annihilation operators $\hat{\mathbf{a}}_r$ and $\hat{\mathbf{a}}_i$ respectively, which are used to reconstruct $\mathbf{A}$ and $\mathbf{B}$. In the construction of $\mathbf{C}$, another four modes are focused on, which are different combinations of $\hat{\mathbf{a}}_r$ and $\hat{\mathbf{a}}_i$ as shown:

$$\begin{aligned} \hat{\mathbf{a}}_1 &= (\hat{\mathbf{a}}_r + \hat{\mathbf{a}}_i)/\sqrt{2}, \quad \hat{\mathbf{a}}_2 = (\hat{\mathbf{a}}_r - \hat{\mathbf{a}}_i)/\sqrt{2}, \\ \hat{\mathbf{a}}_3 &= (i\hat{\mathbf{a}}_r + \hat{\mathbf{a}}_i)/\sqrt{2}, \quad \hat{\mathbf{a}_4} = (i\hat{\mathbf{a}}_r - \hat{\mathbf{a}}_i)/\sqrt{2} \end{aligned} \tag{4.123}$$

These four modes are achieved by passing the return signal and idler to different setups. $\hat{\mathbf{a}}_1$ and $\hat{\mathbf{a}}_2$ are two outputs of the beamsplitter. For $\hat{\mathbf{a}}_3$ and $\hat{\mathbf{a}}_4$, the return signal is passed to a $\lambda/4$ plate, whose output is combined with the idler beam by a 50:50 beamsplitter.

then the elements of $\mathbf{C}$ can be expressed in terms of these parameters such that

$$\begin{aligned} c_{11} &\triangleq \frac{1}{2}(\langle \hat{\mathbf{x}}_1^2 \rangle - \langle \hat{\mathbf{x}}_2^2 \rangle) - \langle \hat{\mathbf{x}}_r \rangle \langle \hat{\mathbf{x}}_i \rangle \\ c_{12} &\triangleq \frac{1}{2}(\langle \hat{\mathbf{p}}_3^2 \rangle - \langle \hat{\mathbf{p}}_4^2 \rangle) - \langle \hat{\mathbf{x}}_r \rangle \langle \hat{\mathbf{p}}_i \rangle \\ c_{21} &\triangleq \frac{1}{2}(\langle \hat{\mathbf{x}}_4^2 \rangle - \langle \hat{\mathbf{x}}_3^2 \rangle) - \langle \hat{\mathbf{p}}_r \rangle \langle \hat{\mathbf{x}}_i \rangle \\ c_{22} &\triangleq \frac{1}{2}(\langle \hat{\mathbf{p}}_1^2 \rangle - \langle \hat{\mathbf{p}}_2^2 \rangle) - \langle \hat{\mathbf{p}}_r \rangle \langle \hat{\mathbf{p}}_i \rangle \end{aligned} \tag{4.124}$$

where $\hat{\mathbf{x}}_j = (\hat{\mathbf{a}}_j + \hat{\mathbf{a}}_j^\dagger)/\sqrt{2}$ and $\hat{\mathbf{p}}_j = -i(\hat{\mathbf{a}}_j - \hat{\mathbf{a}}_j^\dagger)/\sqrt{2}$, $j = 1, 2, 3, 4$.

We note that the SPDC output is a zero-mean Gaussian state. For one system mode, four different operators are measured using the measurement setup stated above. The determination of the expectation value of each operator and its variance can be carried out using the *quantum tomography* [62]. This allows reconstructing the mean value of any quadrature operator, $\langle \hat{\mathbf{s}}_\phi \rangle$, as the statistical average of a suitable *kernel* function over the ensemble of homodyne data, $\{(v_n, \theta_n)\}_{n=1}^N$. Here (v_n, θ_n) denotes the measured data v_n at the system measurement phase θ. The phase range will be $[-\pi, \pi]$. Then, the expected value of $\hat{\mathbf{s}}_\phi$ can be given by

$$\langle \hat{\mathbf{s}}_\phi \rangle = \frac{1}{N} \sum_{n=1}^{N} R_\epsilon(v_n, \theta_n), \quad \text{and} \quad \langle \hat{\mathbf{s}}_\phi^2 \rangle = \frac{1}{N} \sum_{n=1}^{N} K_\epsilon(v_n, \theta_n) \tag{4.125}$$

where N is the total number of samples, and $\epsilon > 0.5$ is the detection efficiency, usually

taken around 90%. R and K are the kernal functions.

The suitable kernels are[61]

$$R_\epsilon(v_n, \theta_n) = 2v_n \cos(\phi - \theta_n) \tag{4.126a}$$

$$K_\epsilon(v_n, \theta_n) = \frac{1}{4}\{1 + (4v_n^2 - \frac{1}{\epsilon})[4\cos^2(\phi - \theta_n) - 1]\} \tag{4.126b}$$

The derivation of the QCB relies on the symplectic diagonalisation of two covariance matrices, which places an upper bound on the minimum probability of error $P_e \leq \frac{1}{2}\exp(-\frac{\eta N_s}{N_b})$. However, in the OPA detector designs, only the 11th, 33th, 13th and 31th elements in the covariance matrices are exploited to increase the difference between $\bar{N}_0$ and $\bar{N}_1$, i.e., the OPA detector designs do not use all the information in the covariance matrix and therefore cannot achieve optimal error performance. The Chernoff bound for the OPA detector [47] is $P_e \leq \frac{1}{2}\exp(-\frac{\eta N_s}{2N_b})$ and is substantially higher than the Quantum Chernoff bound.

From the reconstruction of the covariance matrices, all 16 elements in the matrix can be obtained and will be used for target detection. Therefore, the detection method relying on the reconstructed CM is expected to outperform the OPA detection designs and approach the Quantum Chernoff bound.

4.5.2 Target Detection based on distance of CM

To facilitate target detection in quantum illumination by distinguishing the CM $\mathbf{\Gamma}_1$ from $\mathbf{\Gamma}_0$, we need to introduce some measures of the statistical relationship between

these matrices. Let us suppose we have a library of "noise-only" CM obtained by directing the beams of photons towards a known "no-target" region, followed by correlating the received and the idler beams as described above. We denote this set of estimates of CM under H_0 by $\{\tilde{\mathbf{\Gamma}}_{0n}, n = 1, \cdots, N\}$ and note that these CM estimates are *Hermitian and positive semi-definite* (HPSD) . In the following, we present some measures which account for the statistical relationships between these matrices.

To distinguish between any two of these matrices $\tilde{\mathbf{\Gamma}}_{0m}$ and $\tilde{\mathbf{\Gamma}}_{0n}$, we define a distance measure $d(\tilde{\mathbf{\Gamma}}_{0m}, \tilde{\mathbf{\Gamma}}_{0n})$ which is a metric satisfying the non-negativity, symmetry, and triangle inequality axioms. The distance between two matrices measures the dissimilarity between them. Here, we focus on the following measures.

Euclidean Distance between CM

We can regard two such $M \times M$ matrices as two free points in the M^2 complex signal space $\mathcal{H}$ and apply the Euclidean distance (ED) as the distance measure between them. ED is an inner product [63] distance which is the most commonly used in signal processing because it coincides with the usual concept of distance in a 3-dimensional space. The ED between two such matrices $\tilde{\mathbf{\Gamma}}_{0m}$ and $\tilde{\mathbf{\Gamma}}_{0n}$ is defined as

$$d_{\mathrm{E}}(\tilde{\mathbf{\Gamma}}_{0m}, \tilde{\mathbf{\Gamma}}_{0n}) = \sqrt{\mathrm{tr}\Big[(\tilde{\mathbf{\Gamma}}_{0m} - \tilde{\mathbf{\Gamma}}_{0n})(\tilde{\mathbf{\Gamma}}_{0m} - \tilde{\mathbf{\Gamma}}_{0n})^{\dagger}\Big]} \tag{4.127}$$

Eq. (4.127), induced by the inner product norm, is sometimes also called the Frobenius distance [64].

Riemannian Detection between CMs

Covariance matrices, being HPSD, are structurally constrained, and form a manifold $\mathcal{M}$ in the signal space $\mathcal{H}$ [22]. Thus, the distance between two such matrices should be measured along the geodesic of the manifold. This distance is known as the *Riemannian distance* (RD). Measurement of RD between HPSD $\mathbf{\Gamma} \in \mathcal{M}$ can be facilitated [21], [22] by establishing a mapping $\pi : \mathcal{M} \to \mathcal{H}$. This mapping π associates each point $\mathbf{\Gamma} \in \mathcal{M}$ with a $\mathbf{\Gamma}' \triangleq \pi(\mathbf{\Gamma})$. By choosing a particular mapping π with its corresponding Riemannian metric, we can find a Euclidean subspace $\mathcal{U}_{\mathcal{H}}$ in $\mathcal{H}$ which contains $\mathbf{\Gamma}'$ and which is *isometric* with $\mathcal{T}_{\mathcal{M}}(\mathbf{\Gamma})$, the tangent space at $\mathbf{\Gamma}$ on the manifold $\mathcal{M}$. Hence, the RD between $\mathbf{\Gamma}_1$ and $\mathbf{\Gamma}_2$ on the manifold $\mathcal{M}$ can be expressed directly as the distance between $\mathbf{\Gamma}_1'$ and $\mathbf{\Gamma}_2'$ in the Euclidean subspace $\mathcal{U}_{\mathcal{H}}$ in which ED is the distance measure. Following this approach, three different closed-form expressions of RD for the HPSD matrix manifold have been obtained and studied [22].

$$d_{R_1}(\mathbf{P}_m, \mathbf{P}_m) = \sqrt{\mathrm{tr}\Big[\mathbf{P}_m + \mathbf{P}_n - 2(\mathbf{P}_m^{1/2}\mathbf{P}_n\mathbf{P}_m^{1/2})^{1/2}\Big]} \tag{4.128a}$$

$$d_{R_2}(\mathbf{P}_m, \mathbf{P}_m) = \sqrt{\mathrm{tr}\Big[\mathbf{P}_m + \mathbf{P}_n - 2\mathbf{P}_m^{1/2}\mathbf{P}_n^{1/2}\Big]} \tag{4.128b}$$

$$d_{R_3}(\mathbf{P}_m, \mathbf{P}_m) = \sqrt{\mathrm{tr}\Big[(\log \mathbf{P}_m^{-1/2}\mathbf{P}_n\mathbf{P}_m^{-1/2})^2\Big]} \tag{4.128c}$$

Choices of Distance Measures

The sample covariance matrix $\tilde{\mathbf{\Gamma}}$ follows a Wishart distribution with its mean and covariance matrix defined [65]:

$$\mathbb{E}(\tilde{\mathbf{\Gamma}}) = \mathbf{\Gamma} \tag{4.129}$$

$$\text{cov}[\text{vec}(\tilde{\mathbf{\Gamma}})] = \frac{1}{n}(\mathbf{I}_{4^2} + \mathbf{K})(\mathbf{\Gamma} \otimes \mathbf{\Gamma}) \tag{4.130}$$

where n is the number of identical samples. The matrix $\mathbf{K}$ is defined as

$$\mathbf{K} = \sum_{i,j=1}^{m} (\mathbf{H}_{ij} \otimes \mathbf{H}'_{ij}) \tag{4.131}$$

where $\mathbf{H}_{ij}$ is the 4×4 matrix with only its ijth elements equal to one and other elements zero.

The mean and covariance under the ith hypothesis are $\mathbb{E}(\tilde{\mathbf{\Gamma}}|H_i) = \mathbf{\Gamma}_i$ and $\text{cov}[\text{vec}(\tilde{\mathbf{\Gamma}})|H_i] = \frac{1}{n}(\mathbf{I}_{4^2} + \mathbf{K})(\mathbf{\Gamma}_i \otimes \mathbf{\Gamma}_i)$. The relative distance measured is

$$\Delta = \frac{d(\mathbf{\Gamma}_0, \mathbf{\Gamma}_1)}{\sigma_0 + \sigma_1} \tag{4.132}$$

where $\sigma_i = \sqrt{\text{tr}(\text{cov}[\text{vec}(\tilde{\mathbf{\Gamma}})|H_i])}$.

The relative distance using the Euclidean distance, d_{R1} and d_{R2} has been investigated as shown in Fig.4.15

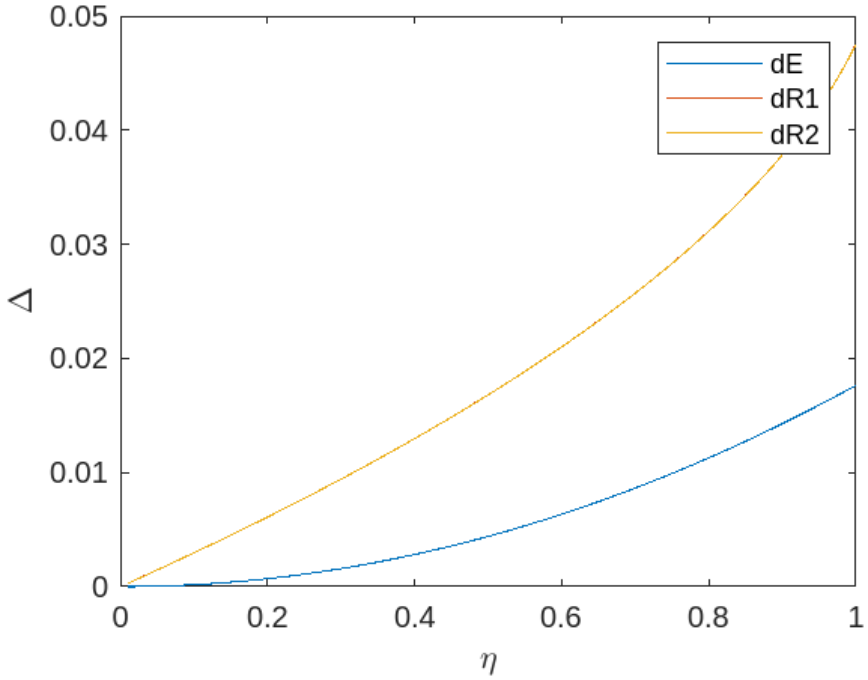

Figure 4.15: The relative distance using three distance measures at different values of η

It can be observed from this plot that Riemannian distances give a higher relative distance over the Euclidean distance. However, results from two Riemannian distances are very close. We choose d_{R2} because it is more mathematically tractable.

In this thesis, we only employ d_{R_2} (re-denoted as d_{R} here) which was developed using the mapping π such that $\mathbf{P}' = \mathbf{P}^{1/2}$ together with an appropriate Riemannian metric [22]. Thus, suppose we have two random sets of Gaussian states $\{\tilde{\mathbf{v}}_{0m}\}$ and $\{\tilde{\mathbf{v}}_{0n}\}$ collected under the hypothesis H_0, and we form the respective sample CMs $\tilde{\mathbf{\Gamma}}_{0m}$ and $\tilde{\mathbf{\Gamma}}_{0n}$ using these two collected sets of Gaussian states. Then, the RD between $\tilde{\mathbf{\Gamma}}_{0m}$

and $\tilde{\mathbf{\Gamma}}_{0n}$ can be expressed as

$$d_{\mathrm{R}}(\tilde{\mathbf{\Gamma}}_{0m}, \tilde{\mathbf{\Gamma}}_{0n}) = \sqrt{\mathrm{tr}\left[\tilde{\mathbf{\Gamma}}_{0m} + \tilde{\mathbf{\Gamma}}_{0n} - 2\tilde{\mathbf{\Gamma}}_{0m}^{1/2}\tilde{\mathbf{\Gamma}}_{0n}^{1/2}\right]} \tag{4.133}$$

Suppose $\{\tilde{\mathbf{v}}_{1m}\}$ and $\{\tilde{\mathbf{v}}_{1n}\}$ are collected under H_1, then the RD between $\tilde{\mathbf{\Gamma}}_{1m}$ and $\tilde{\mathbf{\Gamma}}_{1n}$ can be expressed as

$$d_{\mathrm{R}}(\tilde{\mathbf{\Gamma}}_{1m}, \tilde{\mathbf{\Gamma}}_{1n}) = \sqrt{\mathrm{tr}\left[\tilde{\mathbf{\Gamma}}_{1m} + \tilde{\mathbf{\Gamma}}_{1n} - 2\tilde{\mathbf{\Gamma}}_{1m}^{1/2}\tilde{\mathbf{\Gamma}}_{1n}^{1/2}\right]} \tag{4.134}$$

Mean of Positive Semi-Definite (PSD) Matrices

The mean is a fundamental statistic used in signal processing to represent centrality of data points. For a finite set of real scalars, $\{x_1, x_2, \cdots, x_N\}$, the arithmetic mean or simply the mean is defined as $\bar{x} = \frac{1}{N}\sum_n x_n$. It is well known [66] that the mean minimizes the sum of the squared distances from the points.

For a group of $M \times M$ PSD matrices, $\{\tilde{\mathbf{\Gamma}}_n, n = 1, \cdots, N\}$, the concepts of mean can be generalized by using their geometric properties, thus we have,

$$\bar{\mathbf{\Gamma}} = \arg\min_{\bar{\mathbf{\Gamma}}} \sum_{n=1}^{N} d^2\left(\bar{\mathbf{\Gamma}}, \tilde{\mathbf{\Gamma}}_n\right) \tag{4.135}$$

where d, the distance measured between two matrices, is a general metric. For the particular cases in which d is considered to be the various RD d_{R}, then the results are respectively called the Riemannian mean (RMn), denoted by $\bar{\mathbf{\Gamma}}_{\mathrm{R}}$. Notice that

different RD yields different RMn. Likewise, if d is taken to be ED, we will call the corresponding central points Euclidean mean (EMn), denoted by $\bar{\mathbf{\Gamma}}_{\mathrm{E}}$.

The sample Euclidean mean (EMn) can be evaluated by simply taking the arithmetic mean of the N observed matrices $\tilde{\mathbf{\Gamma}}_n$ such that

$$\bar{\mathbf{\Gamma}}_{\mathrm{E}} = \frac{1}{N}\sum_{n=1}^{N}\tilde{\mathbf{\Gamma}}_n \tag{4.136}$$

On the other hand, RMn has been studied by various authors [67], [68]. A fast convergent algorithm to locate RMn has been developed on the manifold [69] by alternately projecting the mean from the isometric Euclidean subspace to the Riemannian manifold, and back. For our chosen RD of Eq. (4.128b), it turns out to be particular simple such that the RMn is given by:

$$\bar{\mathbf{\Gamma}}_{\mathrm{R}} = \bar{\mathbf{\Gamma}}'_{\mathrm{R}} \cdot \bar{\mathbf{\Gamma}}'^{\dagger}_{\mathrm{R}} \tag{4.137}$$

where $\bar{\mathbf{\Gamma}}'_{\mathrm{R}} = \frac{1}{N}\sum_{n=1}^{N}\tilde{\mathbf{\Gamma}}_n^{1/2}$. Eq. (4.137) can be shown by substituting d_R of Eq. (4.128b) correspondingly into Eq. (4.135) and equating the differential of the objective functions w.r.t. to $\bar{\mathbf{\Gamma}}$ to zero.

Weighted Riemannian Distance and Weighted Mean

The $M \times M$ CM can be emphasized or de-emphasized by the weighting of the distance measure. Weighting is usually designed according to prior information for the facilitation of the application. Weighting of a distance can be effected by applying a HPSD weighting matrix $\mathbf{W}$ to the CM such that we write $\mathbf{W} = \mathbf{\Xi}\mathbf{\Xi}^{\dagger}$, where $\mathbf{\Xi}$ is

$M \times K, K \leq M$, and we let $\mathbf{\Gamma}_{m\mathrm{W}} = \mathbf{\Xi}^{\dagger}\mathbf{\Gamma}_{m}\mathbf{\Xi}$ and $\mathbf{\Gamma}_{n\mathrm{W}} = \mathbf{\Xi}^{\dagger}\mathbf{\Gamma}_{n}\mathbf{\Xi}$ be the weighted versions of $\mathbf{\Gamma}_m$ and $\mathbf{\Gamma}_n$, respectively. It is easy to see that $\mathbf{\Gamma}_{m\mathrm{W}}$ and $\mathbf{\Gamma}_{m\mathrm{W}}$ are also HPSD matrices. The distance between two weighted HPSD matrices then results in a weighted distance. Thus, from Eqs. (4.127) and (4.128b), the weighted ED and weighted RD between $\mathbf{\Gamma}_m$ and $\mathbf{\Gamma}_n$ are given by

$$d_{\mathrm{WE}}(\tilde{\mathbf{\Gamma}}_{0m}, \tilde{\mathbf{\Gamma}}_{0n}) = \sqrt{\mathrm{tr}[(\tilde{\mathbf{\Gamma}}_{0m\mathrm{W}} = \tilde{\mathbf{\Gamma}}_{0n\mathrm{W}})(\tilde{\mathbf{\Gamma}}_{0m\mathrm{W}} = \tilde{\mathbf{\Gamma}}^{\dagger}_{0n\mathrm{W}})]} \tag{4.138a}$$

$$d_{\mathrm{WR}}(\tilde{\mathbf{\Gamma}}_{0m}, \tilde{\mathbf{\Gamma}}_{0n}) = \sqrt{\mathrm{tr}[\tilde{\mathbf{\Gamma}}_{0m\mathrm{W}} + \tilde{\mathbf{\Gamma}}_{0n\mathrm{W}} - 2\tilde{\mathbf{\Gamma}}^{1/2}_{0m\mathrm{W}}\tilde{\mathbf{\Gamma}}^{1/2}_{0n\mathrm{W}}]} \tag{4.138b}$$

By substituting d_{WR} correspondingly into Eq. (4.135) and equating the differential of the objective functions w.r.t. to $\bar{\mathbf{\Gamma}}$ to zero, it can be readily shown that the weighted Riemannian mean is given by

$$\bar{\mathbf{\Gamma}}_{\mathrm{WR}} = \bar{\mathbf{\Gamma}}'_{\mathrm{WR}}\bar{\mathbf{\Gamma}}'^{\dagger}_{\mathrm{WR}} \tag{4.139}$$

where $\bar{\mathbf{\Gamma}}'_{\mathrm{WR}} = \frac{1}{N}\sum_{n=1}^{N}(\tilde{\mathbf{\Xi}}^{\dagger}\tilde{\mathbf{\Gamma}}_{n}\mathbf{\Xi})^{1/2}$.

For the purpose of target detection, the optimum value of the weighting matrix $\mathbf{W}$ will be developed in the following section.

4.5.3 Target Detection Based on the CM

Target detection is a binary problem deciding if the returned signal is noise only or (signal + noise). Let $\mathcal{N}$ designate the set of sample CMs which are formed by

correlating the received noise beam and the idler beam, and let there be N "noise-only" CMs, $\tilde{\mathbf{\Gamma}}_{0n} \in \mathcal{N}, n = 1, \cdots, N$, collected under H_0 as described before. We denote the mean of the collected noise CM by $\bar{\mathbf{\Gamma}}_0$ with the understanding that $\bar{\mathbf{\Gamma}}_0$ may represent the EMn, RMn, or their weighted versions. Then, our hypothesis asserts that any noise CM $\tilde{\mathbf{\Gamma}}_{0k} \in \mathcal{N}$ should be relatively close to $\bar{\mathbf{\Gamma}}_0$. Thus, setting the fixed false alarm rate at $\alpha\%$, we can choose $d_{\text{th}}(\alpha)$ to be the threshold distance away from $\bar{\mathbf{\Gamma}}_0$ such that there is no more than $\alpha\%$ of the noise CM further away from $\bar{\mathbf{\Gamma}}_0$ than this distance. The value of $d_{\text{th}}(\alpha)$ can be obtained from the histogram distribution of the collected noise CM set. If a CM $\tilde{\mathbf{\Gamma}}_k$ from the kth beam lies within the distance of $d_{\text{th}}(\alpha)$ from $\bar{\mathbf{\Gamma}}_0$, H_0 is decided. Otherwise, we decide on H_1. Thus, our decision rule based on the CFAR criterion is given by

$$d(\tilde{\mathbf{\Gamma}}_k, \bar{\mathbf{\Gamma}}_0) \underset{H_0}{\overset{H_1}{\gtrless}} d_{\text{th}}(\alpha) \tag{4.140}$$

Optimum Weighting Matrix for Target Detection

The purpose of weighting a distance measure is to use any prior information for increasing the efficiency of signal processing. For signal detection, the weighting matrix should thus enhance the dissimilarity between (signal + noise) and noise CM. Suppose our library of collected CMs can be divided into two classes: $\mathcal{S}$, from a known signal, and $\mathcal{N}$, from noise. Then, we can seek for a weighting matrix which maximizes the correlation between matrices of similar classes and minimizes the correlation between dissimilar classes. In particular, if $\bar{\mathbf{\Gamma}}_{1W}$ and $\bar{\mathbf{\Gamma}}_{0W}$ are respectively the weighted Riemannian means of the signal and noise CM, it has been suggested [69]

that we seek for an optimum weighting matrix $\mathbf{W} = \mathbf{\Xi}\mathbf{\Xi}^{\dagger}$, $\mathbf{\Xi}$ being $M \times K, K \leq M$, such that

$$\min_{\mathbf{\Xi}} \; F_o(\mathbf{\Xi}) \triangleq \min_{\mathbf{\Xi}} \; \text{tr} \; (\bar{\mathbf{\Gamma}}_{1W}^{-1} \bar{\mathbf{\Gamma}}_{0W}) \tag{4.141}$$

Eq. (4.141) is in fact seeking a weighting matrix minimizing the upper bound of the ratio of the correlation between means of dissimilar classes to that of similar class. It has been shown that [69] the optimum weighting matrix satisfying Eq. (4.141) is given by $\mathbf{\Xi}_{\text{op}} = \{\mathbf{u}_{M-K}, ..., \mathbf{u}_M\}$, where $\{\mathbf{u}_1, ..., \mathbf{u}_M\}$ are the eigenvectors of the eigenvalues, $\{\lambda_1 \geq \cdots \geq \lambda_M\}$, of the matrix product, $(\bar{\mathbf{\Gamma}}_1^{-1} \bar{\mathbf{\Gamma}}_0)$, of the two unweighted means.

In practice, we usually do not have information of the target and the CM under H_1 is generally unknown. We can only use the estimated noise CM measured under H_0. Under such circumstances, following the same principle of optimum weighting as above, we thus seek for an optimum weighting matrix $\mathbf{W} = \mathbf{\Xi}\mathbf{\Xi}^{\dagger}$ such that $\text{tr}(\bar{\mathbf{\Gamma}}_{0W}^{-1})$ is minimized, yielding

$$\mathbf{\Xi}_{\text{op}} = \{\mathbf{u}_{M-K}, ..., \mathbf{u}_M\} \tag{4.142}$$

where $\{\mathbf{u}_1, ..., \mathbf{u}_M\}$ are the eigenvectors corresponding to the eigenvalues, $\{\lambda_1 \geq \cdots \geq \lambda_M\}$, of $\bar{\mathbf{\Gamma}}_0^{-1}$.

We now summarize the above detection procedures as follows

We can now apply these various concepts of ED, RD, EMn, RMn, as well as their respective optimally weighted versions to the decision rule of Eq. (4.140) so that the target detection can be carried out by these different detectors. By varying the value of α, we can plot the ROC of these detectors of different measures.

4.5.4 Simulations and Discussions

The numerical simulations of three CM detectors with the Euclidean distance, Riemannian distance and weighted Riemannian distance are investigated, which are compared with the performance of 2 OPA detectors as shown in Fig.4.16. The QCB as defined in the Eq.4.90 is included in the figure.

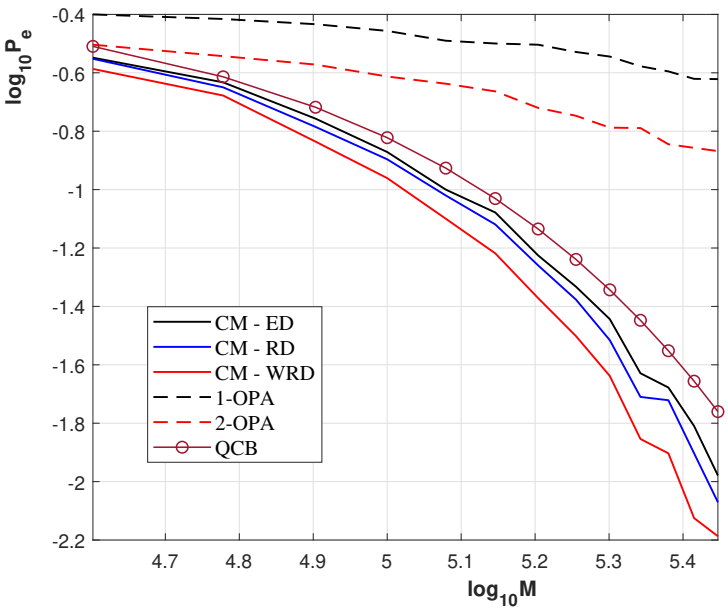

Figure 4.16: The probability of error of three CM detectors, 2 OPA detectors and the QCB

In Fig.4.16, any CM detector achieves a lower probability of error than that of any OPA design. Moreover, the OPA detectors are suboptimal since their performance does not reach the QCB, which is the upper bound of the minimum probability of error. Fortunately, the CM detectors can achieve a probability of error that is below the QCB value. Among these three CM detectors, the one using the RD obtains a

slightly lower probability of error than that of the CM detector with the ED because the RD provides a more accurate and informative measure of the distance between HPSD matrices. The CM design using the weighted RD has the best performance.

The receiving operating characteristics plots the probability of detection at different values of probability of false alarm. The receiving operating characteristics (ROC) for the CM detectors and the OPA detector design are obtained in Fig.4.17.

In quantum illumination, the signal is embedded in a very noisy environment and the propagation attenuation is significant. These parameters can take $N_S = 0.01, N_B = 10, \eta = 0.01$.

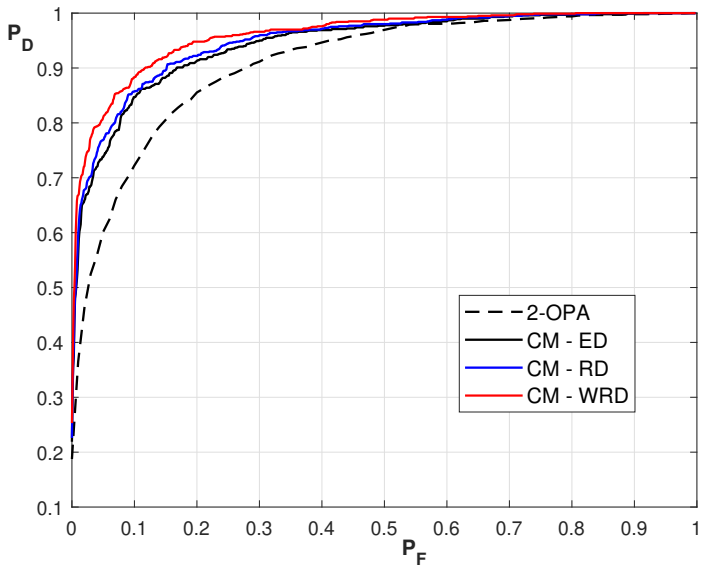

Figure 4.17: The receiving operating characteristics (ROC) of the OPA detection design and CM detectors. The setup is $N_B = 10$, $M = 10^5$, $N_S = 0.01$, $\eta = 0.01$.

It can be observed in Fig.4.17 that the target detection using the ED between CMs outperforms the OPA detection in a way that given a probability of false alarm, CM

detector achieves a higher probability of detection than OPA detector. This advantage is more obvious when the probability of false alarm is small. In radar systems, the acceptable probability of false alarm is small and below 0.2. The maximum enhancement is around 20%.

Moreover, given a chosen threshold value, the probability of error can be found with $P_E = \frac{1}{2}(P_{FA} + P_M)$ assuming that two hypotheses are equally likely to happen.

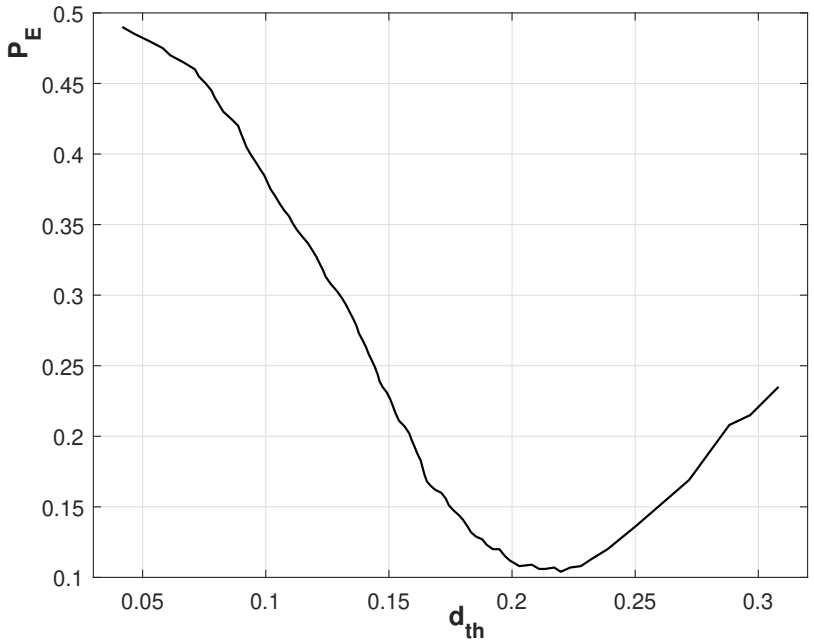

Figure 4.18: The probability of error for different threshold value with $N_B = 10, N_S = 0.01, \eta = 0.01, M = 10^5$

In Fig.4.18, the minimum probability of error achieved by the CM detector is around 0.11 (11%) and for OPA detector, the minimum error probability is 18.1% as shown in Fig.4.8. Therefore, when both detector designs are with their optimal threshold values, the CM detector can achieve about 7% improvement in the minimum error

probability.

Discussions

The improvement of detector using CM is that the distance between two theoretical covariance matrices is much larger than the difference between photon numbers under two hypotheses. With the above parameters, $N_1 - N_0$ is 0.0014; while $d_E(\mathbf{\Lambda}_1 - \mathbf{\Lambda}_0) = 1.4151$, which greatly increases the distance and reduces the probability of error.

Detector Performance for Different M

Fig. 4.19 shows the receiver performance of the 2-OPA and the RD-CM detectors at three different values of M. Here, the three dotted lines and three solid lines represent the ROC of respectively the 2-OPA and the RD-CM detectors at different M. It is observed that while the performance of both detectors are enhanced by the increase of M, the performance of the RD-CM detector is significantly higher than that of the 2-OPA detector for the same M. For the same $P_{\mathrm{F}} = 0.05$, a glance at Fig. 4.19 shows us the substantial difference of P_{D} for the two kinds of detectors. These values are shown in Table 4.3.

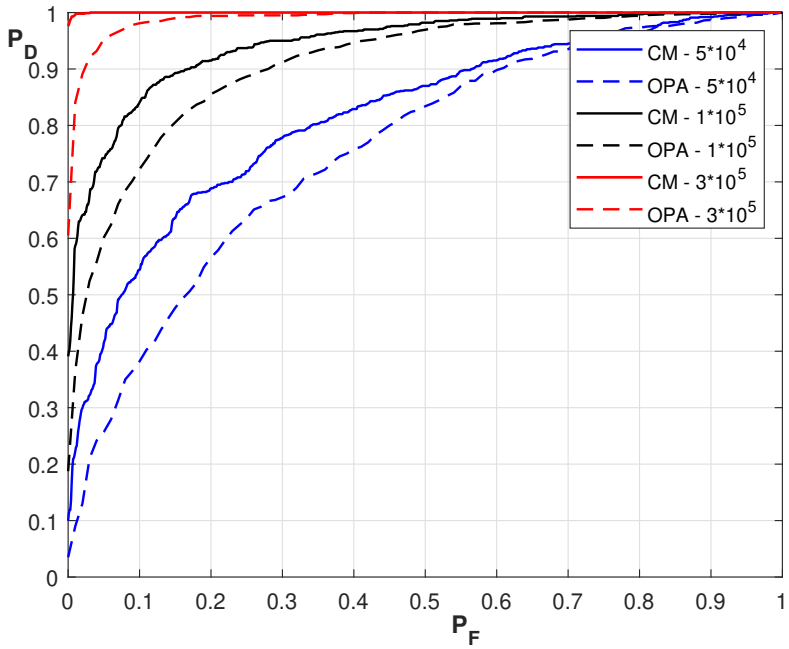

Figure 4.19: The receiving operating characteristics of different detectors at M=$5 * 10^4, 10^5, 3 * 10^5$

	M=$5 * 10^4$	M=$1 * 10^5$	M=$3 * 10^5$
OPA	0.257	0.6015	0.953
CM	0.415	0.742	0.998

Table 4.3: The probability of detection of 2-OPA and CM-RD detectors at $P_F = 0.05$ with $N_B = 10, \eta = 0.01, N_S = 0.01$

Detector Performance for Different N_B

Firstly, the detection performance of the OPA detector with different N_B is investigated from the ROC plot and the minimum error probability. In Fig.4.20, it can be observed that when N_B increases from 1 to 10, the probability of detection decreases

dramatically around 50% at a very small probability of false alarm. If the environment becomes more noisy at $N_B = 20$, the probability of detection decreases near 20%. Continually, at $N_B = 30$, the reduction in the probability of detection is around 5%. Therefore, it can be observed that when the environment becomes more noisy, the probability of detection decreases but the degree of reduction becomes smaller.

In radar systems, the acceptable range of probability of false alarm is from 0 to 0.15. At $N_B = 10$, the probability of detection is from 0.36 to 0.76. At $N_B = 20$, the range of the detection probability is 0.21 to 0.6. At $N_B = 30$, the probability of detection becomes 0.15 to 0.53. Therefore, it can be observed that the probability of detection becomes smaller than 0.5, which is undesirable when the environment is very noisy.

It is investigated that the performance of the CM with ED detector and OPA detector varies when the environment is less noisy ($N_B = 1$) or more noisy ($N_B = 20$) as shown in Fig.4.20

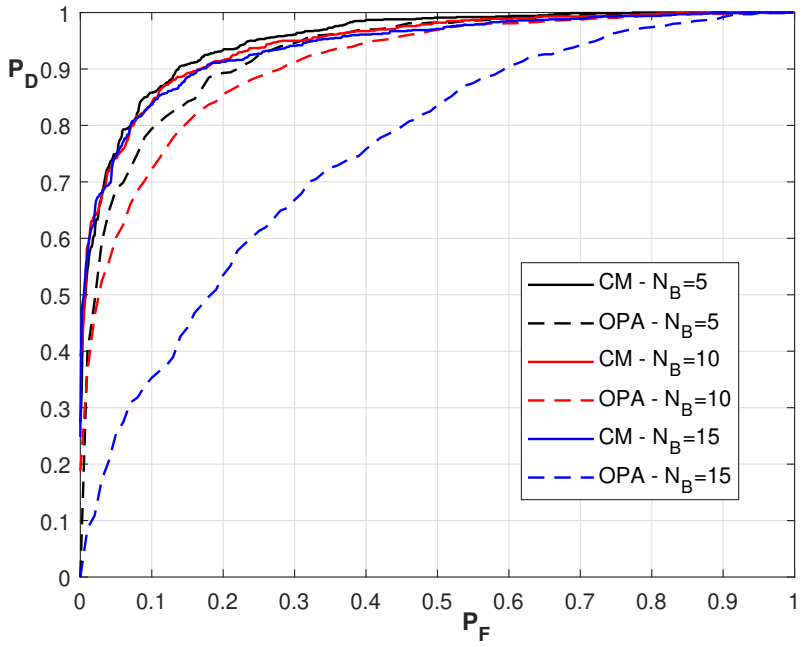

Figure 4.20: The ROCs for CM detector and OPA detector when the noisy intensity varies.

For the OPA detector design, for a given probability of false alarm, the probability of detection decreases around 10% when the noise intensity increases from $N_B = 10$ to $N_B = 20$. However, when the environment becomes less noisy from $N_B = 10$ to $N_B = 1$, there is no improvement in the probability of detection. Therefore, the performance of the OPA detector design degrades largely when the environment becomes noisy.

For the CM detector using ED, the maximum improvement in the probability of detection is around 10% when the environment is less noisy from $N_B = 10$ to $N_B = 1$. Increasing the noisy intensity does not affect the detector performance. Therefore, the CM detector design is more robust in the noisy environment.

Detector Performance for Different η

We now examine the variation of performance of the detectors with that of the overall transmissivity of the channel, η. For the 2-OPA detector, the optimum gain values G_0 and G_1 are depends on η which is, in general, unknown to the receiver. Thus we use the nominal value of $\eta = 0.01$ to arrive at the optimum gains in this example.

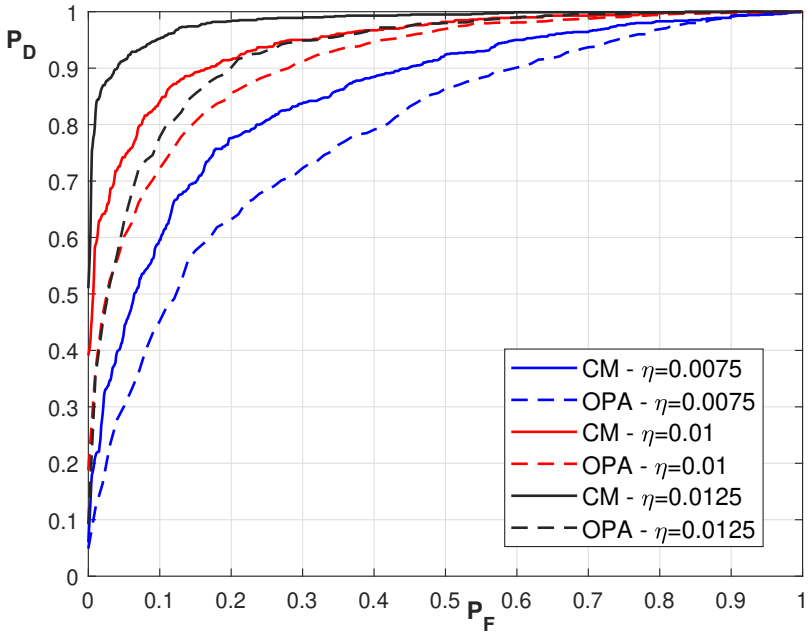

Figure 4.21: The ROCs for CM detector and OPA detector when the noisy intensity varies.

Fig. 4.21 shows the ROCs of the 2-OPA and RD-CM detectors at $\eta = .0075$, .01, and .0125. As expected, the performance of both detectors deteriorate as η decreases. This is because decrease of η indicates the mean values of the respective distributions under H_0 and H_1 are closer together, causing higher probability of error. At equal

values of η, however, the performance of the 2-OPA detector is substantially inferior to that of the RD-CM detector.

Chapter 5

Quantum Estimation in QI

5.1 From Classical Estimation to Quantum Estimation

The classical estimation theory typically treats n data samples $\boldsymbol{x} = (x_1, ..., x_n)$ whose joint probability distribution, $p(\boldsymbol{x}, \boldsymbol{\theta}) = p(x_1, ..., x_n; \theta_1, ...\theta_m)$, depends on m unknown parameters $\boldsymbol{\theta} = (\theta_1, ..., \theta_m)$ that are to be estimated. For instance, the data may be samples taken at a series of time instances, $t_j = jT$, $x_j = x(t_j)$ of the received signal $x(t) = s(t; \boldsymbol{\theta}) + n(t)$ which is composed of noise $n(t)$ of known statistical properties amd a signal $s(t; \boldsymbol{\theta})$ depending on parameters $\boldsymbol{\theta}$ such as the amplitude, time of arrival and carrier frequency. On the basis of n data samples $\boldsymbol{x}$, the values of these parameters $\boldsymbol{\theta}$ are to be estimated as accurately as possible.

Estimation theory sets up a measure of the cost or seriousness of errors in the estimated values $\tilde{\boldsymbol{\theta}} = (\tilde{\theta}_1, ..., \tilde{\theta}_m)$ of the parameters. The most common cost function is a weighted sum of the square errors

$$C(\tilde{\boldsymbol{\theta}}, \boldsymbol{\theta}) = \sum_{k=1}^{m} w_k(\tilde{\theta}_k - \theta_k)^2 \tag{5.143}$$

where ω_k is the weight of the error in the kth parameter. The problem is to find the estimate of each parameter from the collected data samples, $\tilde{\theta}_k = \tilde{\theta}_k(x_1, ..., x_n)$, such that the cost function can be minimized. The lower bound on the sizes of the errors in terms of the mean squared deviation is also of interest. Another measure is the bias of each estimate which is defined as the deviation of the expected value of the estimate from the true value of the parameter.

The classical estimation theory is extended to the quantum system, called *quantum parameter estimation*, also known as *quantum metrology*, was first proposed by Helstrom [70] and Holevo [71]. Its main goal is to perform high-precision measurements of the parameters in a given quantum system. The quantum system of a quantum radar corresponding to the transmitted signal being prepared in a known quantum state, represented by the density operator, $\boldsymbol{\rho}$ which is used for the measurement. The known system state is sent to interact with any present target. Then, the returned signal in the state $\boldsymbol{\rho_\theta}$ incorporates information about the unknown parameters, $\boldsymbol{\theta}$. A subsequent quantum measurement, represented by these measurement operators $\{\hat{\mathbf{M}}_{x_i}\}$, is applied on the received signal $\boldsymbol{\rho_\theta}$ whose expected results are $x_i = \langle \hat{\mathbf{M}}_{x_i} \rangle_{\boldsymbol{\rho_\theta}} = \mathrm{tr}(\hat{\mathbf{M}}_{x_i} \boldsymbol{\rho_\theta})$ that will be used to estimate unknown parameters through an estimator function $\tilde{\boldsymbol{\theta}}(\boldsymbol{x})$. Because of the fundamental probabilistic nature

of quantum mechanics that the system state is not deterministic, the outcomes of measurements are probabilistic, which puts fundamental limits on the precision of the parameter estimation.

5.2 Classical Cramer-Rao Bound and Quantum Cramer-Rao Bound

The Fisher information and Cramer-Rao bound has been extensively studied in the classical systems, which are based on probability distributions. These concepts have been extended into quantum systems as *quantum Cramer-Rao bound* (QCR).

5.2.1 Fisher Information and Cramer-Rao Bound[72]

The *Fisher information* (FI) or classical Fisher information quantifies the amount of information that a set of data contains about unknown parameters. For one single parameter estimation θ, the probability distribution for obtaining a set of data samples, $\boldsymbol{x}$ given the value of the parameter θ is $p(\boldsymbol{x}|\theta)$. For given values of random variable $\boldsymbol{x}$, the *score*, $s(\theta)$ [72] is defined as

$$s(\theta) = \frac{d}{d\theta} \log(p(\boldsymbol{x}|\theta)) \tag{5.144}$$

The score is the derivative of the log-likelihood function with respect to the parameter. Its magnitude is an indication of how sensitive the log-likelihood function is to a

change in the parameter θ, which makes the variance of the score an intuitive metric to justify if the distribution is sensitive to the parameter. The variance of the score gives the *Fisher information*, $\mathcal{I}$,

$$\mathcal{I} = \mathbb{E}\left[\left(\frac{d}{d\theta}\log(p(\boldsymbol{x}|\theta))\right)^2\right] = \mathbb{E}\left[-\frac{d^2}{d\theta^2}\log p(\boldsymbol{x}|\theta)\right] = \int \frac{1}{p(\boldsymbol{x}|\theta)}\left(\frac{dp(\boldsymbol{x}|\theta)}{d\theta}\right)d\boldsymbol{x} \tag{5.145}$$

An estimator is a function of the collected data, $\tilde{\theta}(\boldsymbol{x})$. The bias of an estimator, $b(\tilde{\theta})$, is the average difference between the estimator and the true value

$$b(\tilde{\theta}) = \mathbb{E}[\tilde{\theta}(\boldsymbol{x})] - \theta \tag{5.146}$$

An unbiased estimator has a bias of 0. The *Cramer-Rao Bound* (CRB) places a lower bound on the variance of any unbiased estimator of θ which takes a value of the inverse of the FI,

$$\text{var}[\tilde{\theta}(\boldsymbol{x})] \geq \frac{1}{\mathcal{I}} \tag{5.147}$$

Then, this bound gives an idea of the best possible error that can be achieved for the estimated parameter given measured results $\boldsymbol{x}$.

For the multiparameter estimation problem $\boldsymbol{\theta}$, it is concerned with a *Fisher information matrix*, $\boldsymbol{I}$, whose ij^{th} element is defined as

$$I_{ij} = -\mathbb{E}_{\boldsymbol{\theta}}\left[\frac{\partial^2}{\partial\theta_i\partial\theta_j}p(\boldsymbol{x}|\boldsymbol{\theta})\right] \tag{5.148}$$

Then, the Cramer-Rao bound in the multiparameter estimation problem becomes

$$\mathrm{cov}(\boldsymbol{\theta}) \geq \boldsymbol{I}^{-1} \tag{5.149}$$

where $\mathrm{cov}(\boldsymbol{\theta})$ is the covariance matrix.

5.2.2 Quantum Cramer-Rao Bound[70]

The ultimate precision in the estimation of quantum systems is given by the *quantum Cramer-Rao (QCR) bound*. For the estimation of the parameter θ encoded onto a quantum state, $\boldsymbol{\rho}_\theta$, there is a lower bound on the variance $\Delta\hat{\boldsymbol{\theta}}^2 = \langle\hat{\boldsymbol{\theta}}^2\rangle - \langle\hat{\boldsymbol{\theta}}\rangle^2$ of any unbiased estimator $\hat{\boldsymbol{\theta}}$: $\langle\hat{\boldsymbol{\theta}}\rangle = \theta$. If the considered state, $\boldsymbol{\rho}_\theta$, lives in a Hilbert space of dimensions d, consider a set of basis vectors $\{|f_n\rangle\}_{n=1}^d$ in which the state becomes diagonal

$$\boldsymbol{\rho}_\theta = \sum_{n=1}^{d} p_n \left|f_n\right\rangle \left\langle f_n\right| \tag{5.150}$$

where p_n gives the probability of $\boldsymbol{\rho}_\theta$ being in the state $|f_n\rangle$ and $\sum_{n=1}^d p_n = 1$.

Given that $\hat{\boldsymbol{\Pi}}_x$ is the element of the set of measurement operators that $\int \hat{\boldsymbol{\Pi}}_{\boldsymbol{x}} d\boldsymbol{x} = \hat{\mathbf{I}}$, in the definition of the classical Fisher information in Eq.5.145, the term $\frac{dp(\boldsymbol{x}|\theta)}{d\theta} \triangleq d_\theta p(\boldsymbol{x}|\theta)$ in quantum systems is defined as using the Born rule

$$d_\theta p(\boldsymbol{x}|\theta) = \mathrm{tr}[\hat{\boldsymbol{\Pi}}_x d_\theta \boldsymbol{\rho}_\theta] \tag{5.151}$$

Now, the *Symmetric Logarithmic Derivative* (SLD) operator associated with the parameter $\hat{\mathbf{L}}_\theta$ is defined in [70]

$$2\frac{d\boldsymbol{\rho}_\theta}{d\theta} = \hat{\mathbf{L}}_\theta\boldsymbol{\rho}_\theta + \boldsymbol{\rho}_\theta\hat{\mathbf{L}}_\theta \tag{5.152}$$

Because both the SLD operator and density operators are Hermitian symmetric, the complex conjugate of the $\hat{\mathbf{L}}_\theta\boldsymbol{\rho}_\theta$ is $\boldsymbol{\rho}_\theta\hat{\mathbf{L}}_\theta$. The sum of these two terms only consists of the real part of these two terms and hence, $d_\theta\boldsymbol{\rho}_\theta$ can be given by the real part of $\hat{\mathbf{L}}_\theta\boldsymbol{\rho}_\theta$. Therefore, Eq.5.151 can be written as

$$d_\theta p(\boldsymbol{x}|\theta) = \mathrm{Re}(\mathrm{tr}[\hat{\boldsymbol{\Pi}}_x\hat{\mathbf{L}}_\theta\boldsymbol{\rho}_\theta]) \tag{5.153}$$

The definition of the Fisher information in classical systems in Eq.5.145 can be extended to quantum systems, which is given by

$$\mathcal{I}(\theta) = \int \frac{\mathrm{Re}(\mathrm{tr}[\hat{\boldsymbol{\Pi}}_x\hat{\mathbf{L}}_\theta\boldsymbol{\rho}_\theta])^2}{\mathrm{tr}[\hat{\boldsymbol{\Pi}}_x\boldsymbol{\rho}_\theta]}d\boldsymbol{x} \tag{5.154}$$

This Fisher information is upper bounded by [73]

$$\begin{aligned}
\mathcal{I}(\theta) &\leq \int \left|\frac{\mathrm{tr}[\boldsymbol{\rho}_\theta\hat{\boldsymbol{\Pi}}_x\hat{\mathbf{L}}_\theta]}{\sqrt{\mathrm{tr}[\boldsymbol{\rho}_\theta\hat{\boldsymbol{\Pi}}_x]}}\right|^2 dx \\
&= \int \left|\mathrm{tr}\left[\frac{\sqrt{\boldsymbol{\rho}_\theta}\sqrt{\hat{\boldsymbol{\Pi}}_x}}{\sqrt{\mathrm{tr}[\boldsymbol{\rho}_\theta\hat{\boldsymbol{\Pi}}_x]}}\sqrt{\hat{\boldsymbol{\Pi}}_x}\hat{\mathbf{L}}_\theta\sqrt{\boldsymbol{\rho}_\theta}\right]\right|^2 dx \\
&\leq \int \mathrm{tr}[\hat{\boldsymbol{\Pi}}_x\hat{\mathbf{L}}_\theta\boldsymbol{\rho}_\theta\hat{\mathbf{L}}_\theta]dx \\
&= \mathrm{tr}[\hat{\mathbf{L}}_\theta\boldsymbol{\rho}_\theta\hat{\mathbf{L}}_\theta] = \mathrm{tr}[\boldsymbol{\rho}_\theta\hat{\mathbf{L}}_\theta^2] \triangleq \mathcal{H}(\theta)
\end{aligned} \tag{5.155}$$

The first inequality comes from that the real part of a complex number is equal to or smaller than the absolute value of the complex number.

The second inequality comes from the Schwartz inequality that given two matrices $\boldsymbol{A}$ and $\boldsymbol{B}$,

$$|\mathrm{tr}[\mathbf{A}^{\dagger}\mathbf{B}]|^2 \leq \mathrm{tr}[\boldsymbol{A}^{\dagger}\boldsymbol{A}]\mathrm{tr}[\boldsymbol{B}^{\dagger}\boldsymbol{B}] \tag{5.156}$$

where in our case, $\mathbf{A}^{\dagger} = \frac{\sqrt{\boldsymbol{\rho}_\theta}\sqrt{\hat{\boldsymbol{\Pi}}_x}}{\sqrt{\mathrm{tr}[\boldsymbol{\rho}_\theta\hat{\boldsymbol{\Pi}}_x]}}$ and $\boldsymbol{B} = \sqrt{\hat{\boldsymbol{\Pi}}_x}\hat{\mathbf{L}}_\theta\sqrt{\boldsymbol{\rho}_\theta}$. Then,

$$\mathrm{tr}(\boldsymbol{A}^{\dagger}\boldsymbol{A}) = \mathrm{tr}(\frac{\sqrt{\boldsymbol{\rho}_\theta}\sqrt{\hat{\boldsymbol{\Pi}}_x}}{\sqrt{\mathrm{tr}[\boldsymbol{\rho}_\theta\hat{\boldsymbol{\Pi}}_x]}}\frac{\sqrt{\hat{\boldsymbol{\Pi}}_x}\sqrt{\boldsymbol{\rho}_\theta}}{\sqrt{\mathrm{tr}[\boldsymbol{\rho}_\theta\hat{\boldsymbol{\Pi}}_x]}}) = \mathrm{tr}(\frac{\boldsymbol{\rho}_\theta\hat{\boldsymbol{\Pi}}_x}{\mathrm{tr}[\boldsymbol{\rho}_\theta\hat{\boldsymbol{\Pi}}_x]}) = 1 \tag{5.157}$$

And

$$\mathrm{tr}(\boldsymbol{B}^{\dagger}\boldsymbol{B}) = \mathrm{tr}(\sqrt{\boldsymbol{\rho}_\theta}\hat{\mathbf{L}}_\theta\sqrt{\hat{\boldsymbol{\Pi}}_x}\sqrt{\hat{\boldsymbol{\Pi}}_x}\hat{\mathbf{L}}_\theta\sqrt{\boldsymbol{\rho}_\theta}) = \mathrm{tr}(\boldsymbol{\rho}_\theta\hat{\mathbf{L}}_\theta\hat{\boldsymbol{\Pi}}_x\hat{\mathbf{L}}_\theta) \tag{5.158}$$

The above chain of inequalities proved that the Fisher information $\mathcal{I}$ of any quantum measurement $\hat{\boldsymbol{\Pi}}_x$ is upper bounded by the *quantum Fisher Information* (QFI) $\mathcal{H}(\theta)$ that

$$\mathcal{I}(\theta) \leq \mathcal{H}(\theta) \tag{5.159}$$

Given the Fisher information in quantum systems, the variance for unbiased estimators is lower bounded by the *quantum Cramer-Rao bound* (QCRB)

$$\mathrm{var}(\tilde{\theta}) \geq \frac{1}{\mathcal{H}(\theta)} \tag{5.160}$$

Solving the SLD operators is important to obtain the QCR bound of the quantum system. The definition of the SLD operator in Eq.5.152 is Lyapunov matrix equation

to be solved for the SLD $\hat{\mathbf{L}}_\theta$. The general solution may be written as [74]

$$\hat{\mathbf{L}}_\theta = 2\int_0^\infty \exp(-\boldsymbol{\rho}_\theta t)(\partial_\theta \boldsymbol{\rho}_\theta)\exp(-\boldsymbol{\rho}_\theta t)dt \tag{5.161}$$

given that $\boldsymbol{\rho}_\theta = \sum_n p_n |f_n\rangle \langle f_n|$. This solution becomes

$$\begin{aligned}\hat{\mathbf{L}}_\theta &= 2\int_0^\infty (\sum_n e^{-p_n t}|f_n\rangle\langle f_n|)(\partial_\theta\boldsymbol{\rho}_\theta)(\sum_m e^{-p_m t}|f_m\rangle\langle f_m|)dt \\ &= 2\sum_{m,n}|f_n\rangle\langle f_n|(\partial_\theta\boldsymbol{\rho}_\theta)|f_m\rangle\langle f_m|\int_0^\infty e^{-(p_n+p_m)t}dt \\ &= 2\sum_{n,m}\frac{\langle f_n|(d_\theta\boldsymbol{\rho}_\theta)|f_m\rangle}{p_n+p_m}|f_n\rangle\langle f_m|\end{aligned} \tag{5.162}$$

where $d_\theta\boldsymbol{\rho}_\theta \triangleq \frac{d\boldsymbol{\rho}_\theta}{d\theta}$.

For the multiparameter estimation, $\boldsymbol{\theta} = (\theta_1, \cdots, \theta_m)$, the SLD operators of these m parameters are $\hat{\mathbf{L}} = [\hat{\mathbf{L}}_{\theta_1}, \cdots, \hat{\mathbf{L}}_{\theta_m}]$. Then, the ijth elemenet of the covariance matrix is defined as

$$\mathrm{cov}(\hat{\mathbf{L}})_{ij} = \mathrm{cov}(\hat{\boldsymbol{\theta}}_i, \hat{\boldsymbol{\theta}}_j) = \langle(\hat{\boldsymbol{\theta}}_i - \langle\hat{\boldsymbol{\theta}}_i\rangle)(\hat{\boldsymbol{\theta}}_j - \langle\hat{\boldsymbol{\theta}}_j\rangle)\rangle \tag{5.163}$$

When $i = j$, it gives the variance in estimating ith element; when $i \neq j$, this defines the covariance between ith and jth elements.

This covariance matrix is lower bounded by the *multiparameter QCR bound*

$$\mathrm{cov}(\hat{\mathbf{L}}) \geq \mathbf{H}(\hat{\boldsymbol{\theta}})^{-1} \tag{5.164}$$

where $\mathbf{H}(\hat{\boldsymbol{\theta}})$ is the QFI matrix whose ijth element is defined as

$$H(\hat{\boldsymbol{\theta}})_{ij} = \frac{1}{2}\mathrm{tr}(\boldsymbol{\rho}_{\boldsymbol{\theta}}\{\hat{\mathbf{L}}_{\theta_i}, \hat{\mathbf{L}}_{\theta_j}\}), i, j = 1, \cdots m \tag{5.165}$$

where θ_i is the ith element in $\boldsymbol{\theta}$. $\{\hat{\mathbf{A}}, \hat{\mathbf{B}}\} = \hat{\mathbf{A}}\hat{\mathbf{B}} + \hat{\mathbf{B}}\hat{\mathbf{A}}$ is the anti-commutation relationship between two operators.

5.3 Quantum Estimation Problems in Quantum Illumination

The time-frequency entangled signal and idler beams from the SPDC process is employed to perform the simultaneous range and velocity estimation in the quantum illumination systems. The signal beam is sent towards the region of interest and interacts with any present target. The received signal will be measured in conjunction with the retained idler beam.

In this section, the wavefunction of the signal and idler in the time domain will be introduced. Then, the estimation problem in the QI systems using the SPDC output will be clearly stated.

5.3.1 SPDC Wavefunction in Time and Frequency Domains

The previous section on quantum detection focused on the SPDC outputs in the Fock number representation, which explicitly showed how signal and idler beams are

entangled in terms of the number of photons. This section will focus on the characterization of the SPDC outputs using the temporal waveform, which incorporates information of unknown parameters to be estimated. Outputs from the SPDC process is a two-mode Gaussian state whose Wigner (or wave) function takes a Gaussian form.

Waveform in the Time-Domain and Frequency-Domain

The time-frequency entangled photons are created in the collinearly phase-matched SPDC process of a 2-mm long β-barium borate (BBO) crystal which is pumped by a 30 mW, cw, 390 nm laser beam. The temporal wavefunction of two outputs can be obtained experimentally. The SPDC output is directly passed to spectral filters. The down-converted signal and idler photons are separated from the pump by a dichroic mirror due to the difference in the frequency, and from each other via a polarization beam splitter due to different polarizations of signal and idler photons. They are then coupled into two single-mode fibers. Two measurement devices are used to measure the two-photon coherence time and frequency correlation.

The generation time of the signal photon t_s and idler photon t_i is measured experimentally. Then, the wave function of the signal and idler photons in the time domain

can be obtained as given in Eq.5.166 [75], [76]

$$\begin{aligned}|\psi_{\mathrm{si}}\rangle = N \int\int \exp\Big\{ -i\frac{\omega_p}{2}[(t_s-\bar{t}_s)+(t_i-\bar{t}_i)] - i\frac{\bar{\omega_s}-\bar{\omega}_i}{2}[(t_s-\bar{t}_s)-(t_i-\bar{t}_i)]\Big\} \\ \cdot A(t_s,t_i)B(t_s,t_i)\,|t_s\rangle_s\,|t_i\rangle_i\,dt_s dt_i \\ \triangleq \int\int \psi_{\mathrm{si}}(t_s,t_i)\,|t_s\rangle_s\,|t_i\rangle_i\,dt_s dt_i\end{aligned} \tag{5.166}$$

where $\psi_{\mathrm{si}}(t_s,t_i)$ gives the temporal information of the signal and idler photons. And $\bar{\omega}_s$ and $\bar{\omega}_i$ denote the central frequency of the signal and idler beams. $\omega_p = \bar{\omega}_s + \bar{\omega}_i$ is the frequency of the pump photon. $\bar{t}_s$ and $\bar{t}_i$ are the mean time of generating signal and idler photons respectively. $|t_s\rangle_s$ means that there is one signal photon generated at t_s.

A Gaussian correlation function between the generation time of the signal photon t_s and the idler photon t_i [76],

$$A(t_s,t_i) = \exp\Big\{ -\frac{[(t_s-\bar{t}_s)-(t_i-\bar{t}_i)]^2}{4\tau_r^2}\Big\} \tag{5.167}$$

provides a good approximation for the biphoton temporal correlation function. Here, τ_r stands for the correlation time between the signal and idler photons, which is determined by the bandwidth of the spectral filters. The biphoton temporal correlation function, $A(t_s,t_i)$, can be interpreted as the correlation between the time at which the two photons exit the nonlinear crystal.

The function, $B(t_s,t_i)$, represents the biphoton envelope function [76],

$$B(t_s,t_i) = \exp[-\frac{(t_s-\bar{t}_s+t_i-\bar{t}_i)^2}{16\tau_h^2}] \tag{5.168}$$

where the biphoton envelope is given by the coherence time τ_h of the pump photon of frequency ω_p that was destroyed in the creation of the entangled biphoton.

Given the measured τ_r and τ_h, $\bar{\omega}_s$ and $\bar{\omega}_i$, the wavefunction of the SPDC output after the Gaussian filtering is given as

$$\begin{aligned}\psi_{\mathrm{si}}(t_s,t_i) = \frac{1}{\sqrt{2\pi\tau_r\tau_h}}\exp\left[-i\frac{\omega_p}{2}(t_s+t_i-\bar{t}_s-\bar{t}_i)-i\frac{\bar{\omega}_s-\bar{\omega}_i}{2}(t_s-t_i-\bar{t}_s+\bar{t}_i)\right] \\ \cdot\exp\left[-\frac{(t_s+t_i-\bar{t}_s-\bar{t}_i)^2}{16\tau_h^2}-\frac{(t_s-t_i-\bar{t}_s+\bar{t}_i)^2}{4{\tau_r}^2}\right]\end{aligned} \tag{5.169}$$

The corresponding wave function in the frequency domain can be obtained by applying the Fourier transform on the wavefunction in the time domain as given in Eq.5.169

$$\Psi_{\mathrm{si}}(\omega_s,\omega_i) = \sqrt{\frac{2\tau_h\tau_r}{\pi}}\exp\left[-\frac{\tau_r^2(\omega_s-\omega_i-\Delta\omega)^2}{4}-\tau_h^2(\omega_s+\omega_i-\omega_p)^2\right] \tag{5.170}$$

where $\Delta\omega = \bar{\omega}_s - \bar{\omega}_i$ as the difference between two central frequencies. Then, $\psi(t_s,t_i)$ and $\Psi(\omega_s,\omega_i)$ can be regarded as a Fourier pair.

SPDC Representation

Substituting $A(t_s,t_i)$ and $B(t_s,t_i)$ into Eq.5.169, we obtain the waveform representation of the entangled signal and idler beams such that:

$$\begin{aligned}\left|\psi_{\mathrm{si}}\right\rangle_{si} &= \int\int \psi_{\mathrm{si}}(t_s,t_i)\left|t_s\right\rangle_s\left|t_i\right\rangle_i dt_s dt_i \\ &= \int\int \Psi_{\mathrm{si}}(\omega_s,\omega_i)\left|\omega_s\right\rangle_s\left|\omega_i\right\rangle_i d\omega_s d\omega_i\end{aligned} \tag{5.171}$$

where $|\psi(t_s, t_i)|^2$ gives the probability of obtaining one signal photon at t_s and one idler photon at t_i. $|\Psi(\omega_s, \omega_i)|^2$ provides the probabilistic information in the frequency domain.

The wavefunction in 5.169 can be written in the following form to quantify the degree of entanglement

$$\begin{aligned}\psi(t_s, t_i) = N \exp[-i\bar{\omega}_s(t_s - \bar{t}_s) - i\bar{\omega}_i(t_i - \bar{t}_i)]\cdot \\ \exp\Bigg[- (t_s - \bar{t}_s)^2\sigma_s^2 - (t_i - \bar{t}_i)^2\sigma_i^2 + 2\kappa(t_s - \bar{t}_s)(t_i - \bar{t}_i)\sigma_s\sigma_i]\end{aligned} \tag{5.172}$$

where $N = \frac{2\sqrt{(1-\kappa^2)}\sigma_s\sigma_i}{\pi}$ is the normalization factor and here

$$\sigma_s^2 = \sigma_i^2 = \frac{1}{16\tau_h^2} + \frac{1}{4\tau_r^2} \tag{5.173}$$

and, κ represents the degree of entanglement, which is given by

$$\kappa = \frac{4\tau_h^2 - \tau_r^2}{4\tau_h^2 + \tau_r^2} \tag{5.174}$$

where $\kappa \in [0, 1)$. When $\kappa = 0$, signal and idler beams are uncorrelated and separable. When $\kappa \to 1$, two beams become highly entangled. However, the $\kappa = 1$ does not correspond to any physical system state.

Then, the wavefunction in the frequency domain becomes

$$\Psi(\omega_s, \omega_i) = \tilde{N}_0 \exp\Bigg[- \frac{(\omega_s - \bar{\omega}_s)^2}{4(1-\kappa^2)\sigma_s^2} - - \frac{(\omega_i - \bar{\omega}_i)^2}{4(1-\kappa^2)\sigma_i^2} - \frac{\kappa(\omega_s - \bar{\omega}_s)(\omega_i - \bar{\omega}_s)}{2(1-\kappa^2)\sigma_s\sigma_i}] \tag{5.175}$$

Here, $\tilde{N}_0 = \sqrt{\frac{2\sigma_s\sigma_i}{\pi}}$ is the normalization factor.

5.3.2 Estimation Problem in QI

After the generation of two entangled photons, the signal photon is sent towards the target and the idler is retained as shown in Fig.5.22. Here, we assume the target is at a distance d from the QI system and is moving away along the signal propagation path with a velocity v.

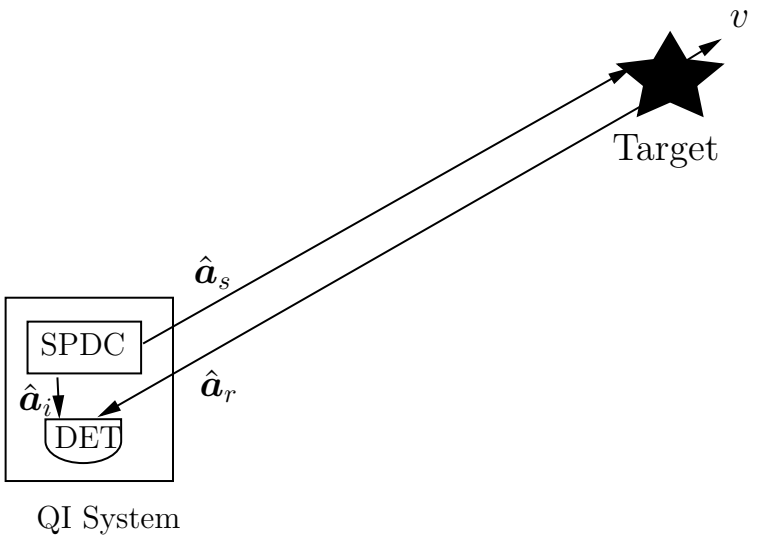

Figure 5.22: The schematic diagram of the QI to interact with a target. The one-way distance between the QI system and the target is d. The QI system includes both the generation of the entangled signal and idler photons and the detection of the return signal and retained idler photons. Here, 'DET' in the QI system denotes the detector used to detect the return signal and idler.

If the signal photon is transmitted at 0 and reaches the target at t_s, then the distance that the signal photon needs to propagate in order to reach the target is $(d + vt_s)$. (Here, c stands for the speed of light, and the sign of the target velocity v is taken

as positive since the target is moving away from the radar system.) Afterwards, the transmitted signal will be reflected back to the QI system by the target. The total distance traveled by the signal photon will be $2(d + vt_s)$. The corresponding time delay experienced is $\frac{2(d+vt_s)}{c}$ and the return signal is received by the QI receiver at

$$t_r(t_s) = t_s + \frac{2(d + vt_s)}{c} = t_s + \frac{2d}{c} + \frac{2vt_s}{c} \tag{5.176}$$

The wavefunction of the return signal and idler, ψ_{ri}, takes the same form given in Eqs.5.172 and 5.175 however, the central generation time of the signal $\bar{t}_s$ is replaced by the central time of return signal $\bar{t}_r$. Moreover, due to the Doppler shift, the central frequency of the signal photon $\bar{\omega}_s$ changes to the central frequency of the return photon $\bar{\omega}_r$. $\bar{t}_r$ and $\bar{\omega}_r$ are given as

$$\bar{t}_r = \bar{t}_s + \frac{2d}{c - v} \tag{5.177}$$

$$\bar{\omega}_r = \frac{c - v}{c + v}\bar{\omega}_s \tag{5.178}$$

Then, the information about the target distance, d, is carried by the central time $\bar{t}_r$ and the information about the target velocity is carried by $\bar{t}_r$ and $\bar{\omega}_r$. The aim of the radar system is to estimate the range and velocity of target as accurate as possible. Therefore, to perform the simultaneous estimation of the new central time and central frequency is the first step. After estimating the time and frequency, the range and velocity can be further estimated.

However, due to the Heisenberg uncertainty relation in Eq.3.48, the accuracy in the simultaneous measurement of two parameters in one system is limited. Hence, the

following section will present the lower bound on product of the variance in the estimation of the central time and frequency.

5.3.3 Quantum Cramer-Rao Bound in QI

In the QI systems, the system state which incorporates unknown system parameters $\boldsymbol{\rho}_{\boldsymbol{\theta}}$ is given as $\boldsymbol{\rho}_{\boldsymbol{\theta}} = |\psi_{\mathrm{ri}}\rangle \langle\psi_{\mathrm{ri}}|$, whose wavefunction is given in Eq.5.172. As stated above, the estimation of the mean arrival of time and frequency of any return signal $\boldsymbol{\theta} \triangleq (\bar{t}_r, \bar{\omega}_r)$ is the focus in the QI estimation problems. The accuracy in the simultaneous estimation of these two parameters is lower-bounded by the multi-variate QCR bound. The reference [23] presented the derivation of the corresponding multivariate *Quantum Cramer-Rao Bound*. The corresponding SLD operators associated with these two parameters are $\hat{\mathbf{L}} \triangleq (\hat{\mathbf{L}}_{\bar{t}_r}, \hat{\mathbf{L}}_{\bar{\omega}_r})$. Based on Eqs.5.152 and 5.162, these SLD operators can be obtained in terms of the focused system operator $\boldsymbol{\rho}_{\mathrm{ri}}$

$$\hat{\mathbf{L}}_{\bar{t}_r} = 2 \sum_{n,m;p_n+p_m\neq 0} \frac{\langle f_m|\partial_{\bar{t}_r}\boldsymbol{\rho}_{\mathrm{ri}}|f_n\rangle}{p_n+p_m} |f_m\rangle \langle f_n| \tag{5.179a}$$

$$\hat{\mathbf{L}}_{\bar{\omega}_r} = 2 \sum_{n,m;p_n+p_m\neq 0} \frac{\langle f_m|\partial_{\bar{\omega}_r}\boldsymbol{\rho}_{\mathrm{ri}}|f_n\rangle}{p_n+p_m} |f_m\rangle \langle f_n| \tag{5.179b}$$

given that $\boldsymbol{\rho}_{\mathrm{ri}} = \sum_n p_n |f_n\rangle \langle f_n|$.

The covariance matrix as mentioned in sec.3.2.2 is bounded by the multiparameter QCR bound

$$\mathrm{cov}(\hat{\mathbf{L}}) \geq \mathbf{H}^{-1}(\boldsymbol{\theta}) \tag{5.180}$$

where $\mathbf{H}(\hat{\boldsymbol{\theta}})$ is the QFI matrix and is defined as

$$H(\boldsymbol{\theta})_{ij} = \frac{1}{2}\mathrm{tr}(\boldsymbol{\rho}_{\mathrm{ri}}\{\hat{\mathbf{L}}_{\theta_i}, \hat{\mathbf{L}}_{\theta_j}\}), i, j = 1, 2 \tag{5.181}$$

where θ_i is the ith element in $\boldsymbol{\theta}$. The symbol $\{\cdot\}$ is the anti-commutation relation.

The state based on the use of the SPDC output is a pure state and then $\boldsymbol{\rho}_{\mathrm{ri}} = |\psi_{\mathrm{ri}}\rangle \langle\psi_{\mathrm{ri}}|$. The derivative of the density matrix with respect to one parameter is given

$$\partial_{\theta_i}\boldsymbol{\rho}_{\mathrm{ri}} = (\partial_{\theta_i} |\psi_{\mathrm{ri}}\rangle) \langle\psi_{\mathrm{ri}}| + |\psi_{\mathrm{ri}}\rangle (\partial_{\theta_i} \langle\psi_{\mathrm{ri}}|) \tag{5.182}$$

There are three density operators of interest:$\boldsymbol{\rho}_{\mathrm{ri}}, \partial_{\bar{t}_r}\boldsymbol{\rho}_{\mathrm{ri}}, \partial_{\bar{\omega}_r}\boldsymbol{\rho}_{\mathrm{ri}}$. Correspondingly, there are three functions to be considered

$$\psi_{\mathrm{ri}} \propto \exp[-i\bar{\omega}_r(t_r - \bar{t}_r) - i\bar{\omega}_i(t_i - \bar{t}_i) - \sigma_r^2(t_r - \bar{t}_r)^2 - \sigma_i^2(t_i - \bar{t}_i)^2 + 2\kappa\sigma_r\sigma_i(t_r - \bar{t}_r)(t_i - \bar{t}_i)] \tag{5.183a}$$

$$\partial_{\bar{t}_r}\psi_{\mathrm{ri}} = [i\bar{\omega}_r + 2\sigma_r^2(t_r - \bar{t}_r) - 2\kappa\sigma_r\sigma_i(t_i - \bar{t}_i)]\psi_{\mathrm{ri}} \tag{5.183b}$$

$$\partial_{\bar{\omega}_r}\psi_{\mathrm{ri}} = [-i(t_r - \bar{t}_r)]\psi_{\mathrm{ri}} \tag{5.183c}$$

where $\sigma_r^2 = \frac{c-v}{c+v}\sigma_s^2$ due to the moving target. These vectors $\{|\psi_{ri}\rangle, \partial_{\bar{t}_r} |\psi_{ri}\rangle, \partial_{\bar{\omega}_r} |\psi_{ri}\rangle\}$ generate a three-dimensional Hilbert space. We can find an orthogonal basis for this

space using the Gram-Schmit decomposition method is $\{|f_i\rangle\}_{i=1}^{3}$ with its corresponding wavefunction [23]

$$f_1(t_r, t_i) = \psi_{\text{ri}}(t_r, t_i) \tag{5.184a}$$

$$f_2(t_r, t_i) = \sqrt{2(1-\kappa)}[\sigma_r(t_r - \bar{t}_r) + \sigma_i(t_i - \bar{t}_i)]\psi_{\text{ri}}(t_r, t_i) \tag{5.184b}$$

$$f_3(t_r, t_i) = \sqrt{2(1-\kappa)}[\sigma_r(t_r - \bar{t}_r) - \sigma_i(t_i - \bar{t}_i)]\psi_{\text{ri}}(t_r, t_i) \tag{5.184c}$$

where $\langle f_i | f_j \rangle = \delta_{ij}$.

The system state in such bases is $\boldsymbol{\rho} = |\psi_{\text{ri}}\rangle \langle \psi_{\text{ri}}|$ and hence, the matrix form under the given orthonormal bases is

$$\boldsymbol{\rho} = \begin{bmatrix} 1 & 0 & 0 \\ 0 & 0 & 0 \\ 0 & 0 & 0 \end{bmatrix} \tag{5.185}$$

Hence, evaluating the values of p_n in Eqs.5.179, we have $p_1 = \langle f_1 | \boldsymbol{\rho} | f_1 \rangle = 1, p_2 = \langle f_2 | \boldsymbol{\rho} | f_2 \rangle = 0, p_3 = \langle f_3 | \boldsymbol{\rho} | f_3 \rangle = 0$. Then, the SLD operators as defined in Eqs.5.179 can be reduced to

$$\begin{aligned} \hat{\mathbf{L}}_{\bar{t}_r} = 2 \Bigg[& \frac{\langle f_1 | \partial_{\bar{t}_r} \boldsymbol{\rho}_{\text{ri}} | f_1 \rangle}{2} |f_1\rangle \langle f_1| + \langle f_2 | \partial_{\bar{t}_r} \boldsymbol{\rho}_{\text{ri}} | f_1 \rangle |f_2\rangle \langle f_1| + \langle f_3 | \partial_{\bar{t}_r} \boldsymbol{\rho}_{\text{ri}} | f_1 \rangle |f_3\rangle \langle f_1| \\ & + \langle f_1 | \partial_{\bar{t}_r} \boldsymbol{\rho}_{\text{ri}} | f_2 \rangle |f_1\rangle \langle f_2| + \langle f_1 | \partial_{\bar{t}_r} \boldsymbol{\rho}_{\text{ri}} | f_3 \rangle |f_1\rangle \langle f_3| \Bigg] \end{aligned} \tag{5.186}$$

$$\hat{\mathbf{L}}_{\bar{\omega}_r} = 2\Bigg[\frac{\langle f_1|\partial_{\bar{\omega}_r}\boldsymbol{\rho}_{\rm ri}|f_1\rangle}{2}|f_1\rangle\langle f_1| + \langle f_2|\partial_{\bar{\omega}_r}\boldsymbol{\rho}_{\rm ri}|f_1\rangle|f_2\rangle\langle f_1| + \langle f_3|\partial_{\bar{\omega}_r}\boldsymbol{\rho}_{\rm ri}|f_1\rangle|f_3\rangle\langle f_1| + \langle f_1|\partial_{\bar{\omega}_r}\boldsymbol{\rho}_{\rm ri}|f_2\rangle|f_1\rangle\langle f_2| + \langle f_1|\partial_{\bar{\omega}_r}\boldsymbol{\rho}_{\rm ri}|f_3\rangle|f_1\rangle\langle f_3|\Bigg] \tag{5.187}$$

Putting the SLD operator in the matrix form based on these three basis vectors can be obtained

$$\hat{\mathbf{L}}_{\bar{t}_r} = \sigma_r\sqrt{2}\begin{bmatrix} 0 & \sqrt{1-\kappa} & \sqrt{1+\kappa} \\ \sqrt{1-\kappa} & 0 & 0 \\ \sqrt{1+\kappa} & 0 & 0 \end{bmatrix} \tag{5.188}$$

$$\hat{\mathbf{L}}_{\bar{\omega}_r} = \frac{1}{\sigma_r\sqrt{2}}\begin{bmatrix} 0 & \frac{i}{\sqrt{1-\kappa}} & \frac{i}{\sqrt{1+\kappa}} \\ -\frac{i}{\sqrt{1-\kappa}} & 0 & 0 \\ -\frac{i}{\sqrt{1+\kappa}} & 0 & 0 \end{bmatrix} \tag{5.189}$$

where ijth element of $\hat{\mathbf{L}}_{\bar{t}_r}$ and $\hat{\mathbf{L}}_{\bar{\omega}_r}$ corresponds to the projection of $\hat{\mathbf{L}}_{\bar{t}_r}$ and $\hat{\mathbf{L}}_{\bar{\omega}_r}$ operators into the basis space $|f_i\rangle\langle f_j|$. The detailed derivation of Eqs.5.188 and 5.189 is included in Appendix B.1.

The QFI matrix can be obtained by using Eq.5.181 with the matrix form of the SLD operators and the system state in Eq.5.185

$$\mathbf{H} = \begin{bmatrix} 4\sigma_r^2 & 0 \\ 0 & \frac{1}{\sigma_r^2(1-\kappa^2)} \end{bmatrix} \tag{5.190}$$

The inverse of this matrix is

$$\mathbf{H}^{-1} = \frac{1-\kappa^2}{4}\begin{bmatrix} \frac{1}{\sigma_r^2(1-\kappa^2)} & 0 \\ 0 & 4\sigma_r^2 \end{bmatrix} \tag{5.191}$$

Based on Eq.5.164, the variance of the time estimator is lower bounded by $\frac{1}{4\sigma_r^2}$ and the lower bound of the variance of the frequency estimator is $\sigma_r^2(1-\kappa^2)$. Then, the product of the uncertainties of time and frequency estimators is

$$\Delta\bar{t}_r \Delta\bar{\omega}_r \geq \frac{\sqrt{1-\kappa^2}}{2} \tag{5.192}$$

where $\Delta\bar{t}_r$ and $\Delta\bar{\omega}_r$ stand for the standard deviation in estimating $\bar{t}_r$ and $\bar{\omega}_r$ respectively.

5.3.4 QCR Bound with Random Channel

The derivation of the QCR bound above considers the theoretical wavefunction of the return signal and idler beams without any distortion. In this section we consider the more realistic case when the wavefuction of the returned photon is affected by the random channel. During the propagation through a noisy random channel, the photon will be coupled to the external environment and hence, its wavefunction will be affected by this random fluctuation. The photon wavefunction is transmitted through this random channel. The effect of this propagating medium on the signal photon can thus be represented by the convolution of the photon temporal wavefunction with the random wavefunction ψ_n[77]

$$\psi_{\mathrm{ri}}^n = \psi_{\mathrm{ri}}(t_r, t_i) * \psi_n(t_r) \tag{5.193}$$

where $*$ stands for the convolution operation between two wave functions. ψ_n is the temporal wavefunction of the noise

$$\psi_n(t) \propto \exp(-\sigma_n^2 t^2) \tag{5.194}$$

where σ_n^2 represents the variance due to the external environment and also the coupling strength between the system and the environment. In the following, we investigated how this random channel may affect the Quantum Cramer-Rao Bound on the estimation of $\bar{t}_r$ and $\bar{\omega}_r$. The convolution of the signal wavefunction with the noise wavefunction yields

$$\begin{aligned}\psi_{\mathrm{ri}}^n = &\Big[\frac{2}{\pi}\sigma_n\sigma_s\sigma_i\sqrt{\frac{1-\kappa^2}{\sigma_n^2+\sigma_s^2}}\Big]^{1/2}\cdot\exp\Big[-i\frac{\sigma_n^2}{\sigma_n^2+\sigma_s^2}(t_r-\bar{t}_r)\bar{\omega}_r - i\frac{\kappa\sigma_s\sigma_i\bar{\omega}_r+\sigma_n^2\bar{\omega}_i+\sigma_s^2\bar{\omega}_i}{\sigma_n^2+\sigma_s^2}(t_i-\bar{t}_i)\Big]\\ &\cdot\exp\Big[-\frac{\sigma_n^2\sigma_s^2}{\sigma_n^2+\sigma_s^2}(t_r-\bar{t}_r)^2 - \frac{\sigma_n^2\sigma_i^2+(1-\kappa^2)\sigma_s^2\sigma_i^2}{\sigma_n^2+\sigma_s^2}(t_i-\bar{t}_i)^2 + \frac{2\kappa\sigma_n^2\sigma_s\sigma_i}{\sigma_n^2+\sigma_s^2}(t_r-\bar{t}_r)(t_i-\bar{t}_i)\Big]\end{aligned} \tag{5.195}$$

Following the same procedures in deriving the QCR bound without noise in Sec. 5.3.3, the variance in estimating $\bar{t}_r$ and $\bar{\omega}_r$ with the noise considered becomes

$$\mathrm{var}(\bar{t}_r) \geq \frac{(\sigma_n^2+\sigma_s^2)^2}{2\sigma_n^2\sigma_s^2[2\sigma_n^2+(1+\kappa^2)\sigma_s^2]} \tag{5.196a}$$

$$\mathrm{var}(\bar{\omega}_r) \geq \frac{2(1-\kappa^2)\sigma_n^2\sigma_s^2(\sigma_n^2+\sigma_s^2)^2}{2\sigma_n^6+2\kappa^2\sigma_n^2\sigma_s^4+(1+3\kappa^2)\sigma_s^2\sigma_n^4+\kappa^2(1-\kappa^2)\sigma_s^6} \tag{5.196b}$$

The product of these variances gives

$$\mathrm{var}(\bar{t}_r)\mathrm{var}(\bar{\omega}_r) \geq \frac{(1-\kappa^2)(1+\sigma_s^2/\sigma_n^2)^4}{[2+(1+\kappa^2)\sigma_s^2/\sigma_n^2][2+2\kappa^2\sigma_s^4/\sigma_n^4+(1+3\kappa^2)\sigma_s^2/\sigma_n^2+\kappa^2(1-\kappa^2)\sigma_s^6/\sigma_n^6]} \tag{5.197}$$

As shown, the variance is highly dependent on the ratio between σ_s and σ_n, $\frac{\sigma_s^2}{\sigma_n^2}$. The joint standard deviation at different signal-to-noise (SNR) ratio is plotted in Fig.5.23

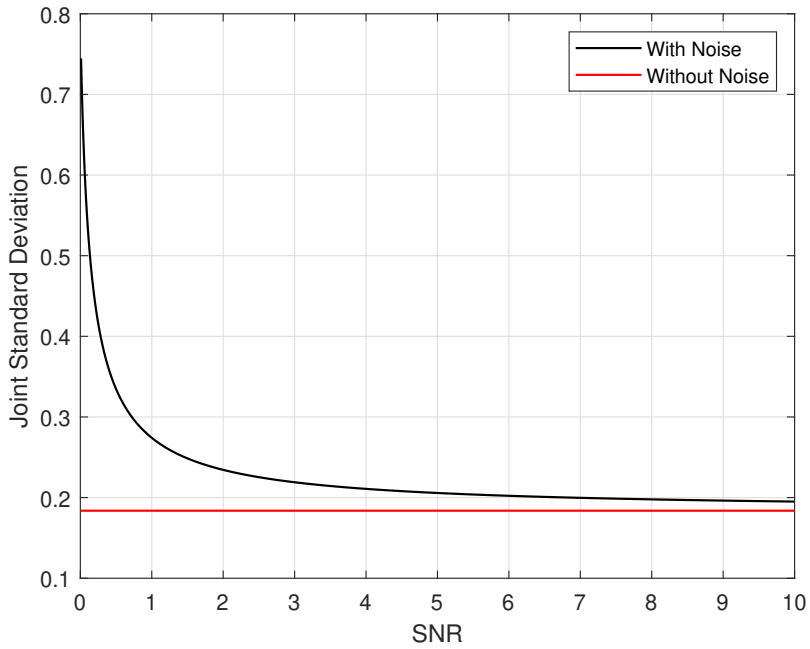

Figure 5.23: The joint estimation uncertainty at different SNR values from 0.01 to 10 with $\kappa = 0.93$. The line of the joint standard deviation without noise is plotted using Eq.5.192

As shown in Fig.5.23, the joint estimation uncertainty decreases when the signal to noise ratio increases. It can be seen that the error bound in the noisy case will approach the limit of the noiseless case when the SNR becomes infinitely large. Moreover, when the noise is much larger than the useful signal, the error becomes larger than that of the noiseless case.

We also plotted the product of two variances given in Eqs.5.196 as a function of the degree of entanglement, κ with 3 SNR values in Fig.5.24.

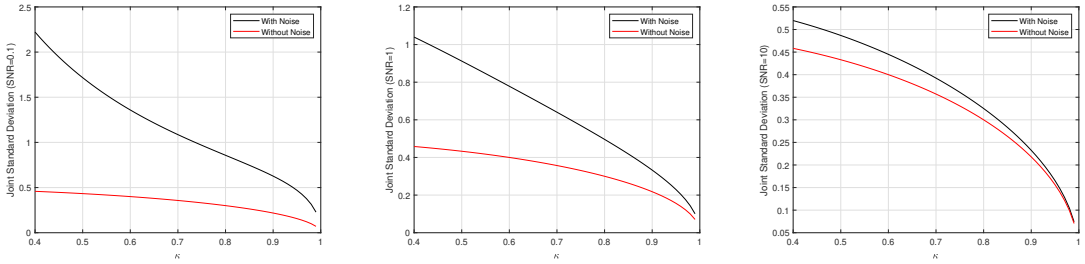

(a) SNR=0.1 (b) SNR=1 (c) SNR=10

Figure 5.24: The joint estimation uncertainty at different values of $\kappa \in [0.4, 0.99)$

In Fig.5.24(a), at a low SNR value, the error is significant at low degree of freedom. When the system becomes more entangled, the effect of the noise on the estimation error becomes less obvious. When the SNR value increases, the improvement due to the system entanglement on the error performance becomes less significant. Therefore, when the environment is very noisy and/or the useful signal is weak, employing a highly entangled signal will be highly preferred. When the SNR value increases, it is less desired to employ entangled signals due to its difficulty in generating entangled states.

5.4 Joint Estimation using the Ambiguity Function

In classical radar systems, early researchers introduced a function called the *ambiguity function* that captures some of the inherent resolution properties of a radar system. The ambiguity function was firstly introduced by Ville [78]; and generally identified with Woodward because of his pioneering work [79], [80]. Woodward was interested

in characterizing how well one could identify the target parameters of the time-delay (range) and Doppler frequency shift (velocity) based on the transmission of a known wavefunction, $s(t)$. He established the ambiguity function by first noting that a good waveform is one which could be used to distinguish between radar returns with different target parameters.

In radar systems, the received signal, $r(t)$ is composed of transmitted signal $s(t)$ and the noise $n(t)$

$$r(t) = \alpha s(t-\tau)e^{-i2\omega_d t} + n(t) \tag{5.198}$$

where α represents the attenuation that the signal experiences over the whole propagation process. τ and ω_d are the time delay and Doppler frequency shift, which are to be estimated. Here, $n(t)$ stands for the additive white Gaussian noise.

The ambiguity function is designed to measure the resemblance between received radar signal and the transmitted signals with different time delay $\Delta\tau$ and doppler shift $\Delta\omega$ as given in

$$f(\Delta\tau, \Delta\omega) = \left| \int r(t)s^*(t-\Delta\tau)e^{-i\Delta\omega t}dt \right|^2 \tag{5.199}$$

In the definition of the ambiguity function, $r(t)$ represents the signal containing the information of parameters to be estimated. The signal $s(t-\Delta\tau)e^{i\Delta\omega t}$ with a controllable time delay, $\Delta\tau$ and frequency shift $\Delta\omega$ is introduced, which is referred to as a reference signal. Then, the ambiguity function can reach its maximum value when the time delay and frequency shift in the reference signal are matched with the values of unknown parameters in the received signal. The implementation of the idea of

the ambiguity function in classical radar systems relies on the use of matched filter, which takes the received signal and the reference signal with known time shift and frequency shift.

The shape of the ambiguity function is usually determined by a plot of f over $\Delta\tau, \Delta\omega$. The simultaneous determination of time delay and frequency shift contains some error. The error in measurement will be proportional to the dimensions of the central spike of the ambiguity surface; that is, the larger the area of the spike, the less accurate the measurement. Therefore, in the classical radar systems, many researches have been devoted to designing the transmitted waveform $s(t)$ to obtain a desired sharp spike.

Feasibility of AF in QI

In quantum illumination, the time delay and Doppler frequency shift are incorporated in the wavefunctions of return signals. Therefore, the similar idea of *quantum ambiguity function* has been firstly mentioned in [81]. A pair of reference signal and idler photons are generated and will experience a known time delay and known frequency shift with its wavefunction $\psi_{\mathrm{si}}(t_s - \Delta\tau, t_i)\exp(-i\Delta\omega t_s)$. Then, this reference pair is correlated with the pair of the return signal and idler $\psi_{\mathrm{ri}}(t_r, t_i)$. Following the idea of the classical ambiguity function, the correlation between two wavefunctions is established.

In classical radar systems, the return signal $r(t)$ is deterministic and can be obtained directly from the signal reception. However, in quantum illumination, the complete information of the wavefunction cannot be obtained easily. Because the wavefuntion

in quantum systems provides the probabilistic information of photons, the measurement result of each photon gives its time arrival, which becomes deterministic and loses the probabilistic information. Therefore, in the quantum ambiguity function, the critical part is to obtain the accurate reconstruction of the wavefunction, $\tilde{\psi}_{\mathrm{ri}}(t_r, t_i)$. Furthermore, the implementation of the ambiguity function in classical radar systems uses a matched filter to directly combine the received signal and reference signal to generate the final result. However, in quantum illumination systems, the idea can only be applied to the *post-measurement results*. A function of the form of $\psi_{\mathrm{si}}(t_s, t_i)$ with a known time delay $\Delta\tau$ and frequency shift $\Delta\omega$ is used to match the reconstructed wavefunction. Then, the time delay and frequency shift of the best fitted function gives the estimation of the time delay and Doppler frequency shift experienced by the signal.

5.4.1 Practical Implementation of Wavefunction Reconstruction [82]

The temporal wavefunction of signal and idler photons as in Eq.5.172 contains both amplitude and phase information. Then, the reconstruction process contains the measurement of the joint temporal intensity (JTP), $|\psi_{\mathrm{ri}}(t_r, t_i)|^2$ and the joint temporal phase (JTP), $\arg(\psi_{\mathrm{ri}}(t_r, t_i))$. [82] has proposed a method to provide a full characterization of the two-photon wavefunction based on the phenomenon of interference between the SPDC state and a joint state of two coherent signals. The definition of the coherent state/signal can be found in Sec. 2.1.3. Here the SPDC outputs, represented by their annihilation operators, $\hat{\mathbf{a}}_s^v$ and $\hat{\mathbf{a}}_i^v$ are both vertically polarised. Both

coherent signals are horizontally polarised and denoted as $\hat{\mathbf{a}}_{c1}^{h}$ and $\hat{\mathbf{a}}_{c2}^{h}$. All beams are passed to a quarter- and a half-wave plate as shown in Fig.5.25, which apply a unitary transformation on these two outputs. Quarter-wave plate (QWP) ($\lambda/4$), which converts linearly polarized light into circularly polarized light. Half wave plate (HWP) ($\lambda/2$), which shifts the polarization direction of linearly polarized light. The waveplate works by shifting the phase between two perpendicular polarisation components of the light wave. A typical waveplate is a birefringent crystal with a chosen orientation and thickness. A pair consisting of one vertically polarised beam (signal or idler) and one horizontally polarised coherent beam is combined by the QWP and HWP, one of whose outputs is passed to a 50:50 beamsplitter. The BS will combine two outputs from two pairs and generate two outputs to be measured.

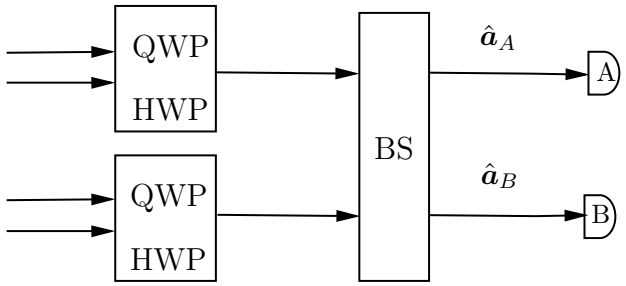

Figure 5.25: The schematic diagram of the interferometric measurement process.

The unitary transformation achieved by the quarter- and half-wave plates can be represented as [83]

$$\hat{\mathbf{U}} = \begin{bmatrix} \cos\theta & e^{i\phi}\sin\theta \\ e^{-i\phi}\sin\theta & -\cos\theta \end{bmatrix} \tag{5.200}$$

where θ and ϕ are the polar and azimuthal angle imposed by the quarter- and half-wave plate idler respectively.

Then, outputs from the QWP and HWP are, respectively,

$$\hat{\mathbf{a}}_1(t) = \cos\theta\hat{\mathbf{a}}^h_{c1}(t) + e^{i\phi}\sin\theta\hat{\mathbf{a}}^v_r(t) \tag{5.201a}$$

$$\hat{\mathbf{a}}_2(t) = e^{-i\phi}\sin\theta\hat{\mathbf{a}}^h_{c2}(t) - \cos\theta\hat{\mathbf{a}}^v_i(t) \tag{5.201b}$$

which are to be measured to reconstruct the wavefunction.

The joint state of the SPDC signal $|\psi_{\text{ri}}\rangle$ and two coherent states $|\alpha\rangle \triangleq |\alpha\rangle_{r1}|\alpha\rangle_{r2}$ is defined as $|\zeta\rangle \triangleq |\psi_{\text{ri}}\rangle \otimes |\alpha\rangle$. Here, $|\alpha\rangle$ denotes the coherent state (see Section 2.1.3) where α is the displacement applied on the vacuum state. The joint state of the received signal and idler can be defined by the joint wavefunction ψ_{ri}

$$|\psi_{\text{ri}}\rangle_{\text{ri}} = \int\int \psi_{\text{ri}}(t_r,t_i)\hat{\mathbf{a}}^\dagger_r(t_r)\hat{\mathbf{a}}^\dagger_i(t_i)\,|0\rangle_r\,|0\rangle_i\,dt_r dt_i \tag{5.202}$$

Then, the wavefunction can be defined as

$$\begin{aligned}
\psi_{\text{ri}}(t_r,t_i) &= \langle 0|\,\langle 0|\,\hat{\mathbf{a}}_i(t_i)\hat{\mathbf{a}}_r(t_r)\,|\psi_{\text{ri}}\rangle_{\text{ri}} \\
&= \langle 0|\,\langle 0|\,\hat{\mathbf{a}}_i(t_i)\hat{\mathbf{a}}_r(t_r)\int\int \psi_{\text{ri}}(t'_r,t'_i)\hat{\mathbf{a}}^\dagger_r(t'_r)\hat{\mathbf{a}}^\dagger_i(t'_i)\,|0\rangle_r\,|0\rangle_i\,dt'_r dt'_i \\
&= \langle 0|\,\langle 0|\,\hat{\mathbf{a}}_i(t_i)\hat{\mathbf{a}}_r(t_r)\psi_{\text{ri}}(t_r,t_i)\hat{\mathbf{a}}^\dagger_r(t_r)\hat{\mathbf{a}}^\dagger_i(t_i)\,|0\rangle_r\,|0\rangle_i \\
&= \psi_{\text{ri}}(t_r,t_i)\,\langle 0|\,\langle 0|\,\hat{\mathbf{a}}_i(t_i)\hat{\mathbf{a}}_r(t_r)\hat{\mathbf{a}}^\dagger_r(t_r)\hat{\mathbf{a}}^\dagger_i(t_i)\,|0\rangle_r\,|0\rangle_i \\
&= \psi_{\text{ri}}(t_r,t_i)\,\langle 0|\,\langle 0|\,[\hat{\mathbf{I}}_r(t_r)+\hat{\mathbf{n}}_r(t_r)][\hat{\mathbf{I}}_i(t_i)+\hat{\mathbf{n}}_i(t_i)]\,|0\rangle_r\,|0\rangle_i \\
&= \psi_{\text{ri}}(t_r,t_i)
\end{aligned} \tag{5.203}$$

The third equality becomes from the orthogonality that $\langle t_i|t'_i\rangle_i = \delta(t_i - t'_i)$ and $\langle t_r|t'_r\rangle_r = \delta(t_r - t'_r)$. Therefore, the only non-zero terms exist when $t_i = t'_i$ and

$t_r = t'_r$. The fifth equality becomes from the commutation relation and the definition of the number operator that $\hat{\mathbf{a}}\hat{\mathbf{a}}^\dagger = \hat{\mathbf{a}}^\dagger\hat{\mathbf{a}} + \hat{\mathbf{I}} = \hat{\mathbf{n}} + \hat{\mathbf{I}}$. Then the last equality becomes from that $\hat{\mathbf{n}}\,|0\rangle = 0\,|0\rangle$; hence, the non-zero term is $\langle 0|\,\langle 0|\,\hat{\mathbf{I}}_r(t_r)\hat{\mathbf{I}}_i(t_i)\,|0\rangle\,|0\rangle = 1$ given that $\langle 0|0\rangle = 1$.

Similarly, the two-photon wavefunction of the joint state $|\zeta\rangle$ at t_1 and t_2 is given as

$$\begin{aligned}\psi^{(\zeta)}_{AB}(t_1,t_2) &= \langle 0\,\langle 0|\,\langle 0|\,\langle 0|\,\hat{\mathbf{a}}_A(t_1)\hat{\mathbf{a}}_B(t_2)|\zeta\rangle \\ &= e^{-i\phi}\cos\theta\sin\theta\psi_c\,\langle 0|\,\langle 0|\psi_{\mathrm{ri}}\rangle - e^{i\phi}\sin\theta\cos\theta\psi_{\mathrm{ri}}(t_1,t_2)\,\langle 0|\,\langle 0|\alpha\rangle \\ &+ \sin^2\theta\psi_r(t_1)\psi_{c2} - \cos^2\theta\psi_{c1}\psi_i(t_2)\end{aligned} \tag{5.204}$$

The term ψ_c stands for the product of the ψ_{c1} and ψ_{c2}, which stand for the wavefunction of the coherent states $|\alpha\rangle_{c1}$ and $|\alpha\rangle_{c2}$ respectively, which are time-independent. ψ_r and ψ_i represent the wavefunction of the return signal and idler correspondingly. According to [84], there are two different cases of the SPDC output: (a) degenerate SPDC output in which two output photons are indistinguishable in all parameters (frequency, direction and polarization), (b) non-degenerate SPDC output in which two generated photons have different parameters. These two processes can be represented by having two different squeezing operators $\hat{\mathbf{S}}_a$ and $\hat{\mathbf{S}}_b$ respectively operating on the vacuum state $|0\rangle$, where $\hat{\mathbf{S}}_a(\xi) = \exp[(\xi\hat{\mathbf{a}}^2 - \xi^*\hat{\mathbf{a}}^{\dagger 2})/2]$ and $\hat{\mathbf{S}}_b = \exp[-\xi\hat{\mathbf{a}}_s\hat{\mathbf{a}}_i + \xi^*\hat{\mathbf{a}}_s^\dagger\hat{\mathbf{a}}_i^\dagger]$ with ξ being the squeezing parameter that determines the squeezing magnitude and phase. The two last two terms become 0[82]

With $\theta = \pi/4$ for simplicity, it becomes

$$\psi^{\zeta}_{AB}(t_1,t_2) = \frac{1}{2}e^{-i\phi}\psi_r\,\langle 0|\,\langle 0|\psi_{\mathrm{ri}}\rangle - \frac{1}{2}e^{i\phi}\psi_{\mathrm{ri}}(t_1,t_2)\,\langle 0|\,\langle 0|\alpha\rangle \tag{5.205}$$

The measurable second order correlation function, which is proportional to the measured intensity of the output is [82]

$$\begin{aligned} g_{AB}^{(2)} &\propto \mathrm{tr}[\hat{\mathbf{a}}_B^\dagger(t_2)\hat{\mathbf{a}}_A^\dagger(t_1)\hat{\mathbf{a}}_A(t_1)\hat{\mathbf{a}}_B(t_2)\,|\zeta\rangle\,\langle\zeta|] \\ &= \langle\zeta|\hat{\mathbf{a}}_B^\dagger(t_2)\hat{\mathbf{a}}_A^\dagger(t_1)\hat{\mathbf{a}}_A(t_1)\hat{\mathbf{a}}_B(t_2)|\zeta\rangle \\ &= |\gamma e^{-2i\phi} - \psi_{\mathrm{ri}}(t_1,t_2)|^2 \triangleq y(t_1,t_2) \end{aligned} \tag{5.206}$$

where $\gamma = \psi_c \frac{\langle 0|\psi_{\mathrm{ri}}\rangle}{\langle 0|\alpha\rangle}$ and ψ_c is the wavefunction of the coherent state.

At $\phi = 0$, $y_1(t_1,t_2) = g_{AB}^{(2)} = |\gamma - \psi_{\mathrm{ri}}(t_1,t_2)|^2$.

At $\phi = \pi/3$, $y_2(t_1,t_2) = g_{AB}^{(2)} = |(-\frac{1}{2} + \frac{i\sqrt{3}}{2})\gamma - \psi_{\mathrm{ri}}(t_1,t_2)|^2$.

At $\phi = 2\pi/3$, $y_3(t_1,t_2) = g_{AB}^{(2)} = |(-\frac{1}{2} - \frac{i\sqrt{3}}{2})\gamma - \psi_{\mathrm{ri}}(t_1,t_2)|^2$.

Then, at (t_1,t_2), γ can be obtained as

$$\gamma(t_1,t_2) = \frac{\sqrt{2}}{2}\sqrt{\bar{y}(t_1,t_2) + \sqrt{3\bar{y}(t_1,t_2) - \frac{2}{3}(y_1^2(t_1,t_2) + y_2^2(t_1,t_2) + y_3^2(t_1,t_2))}} \tag{5.207}$$

where $\bar{y}(t_1,t_2) = \frac{y_1+y_2+y_3}{3}$. Hence, the value of two-photon wavefunction ψ_{ri} at (t_1,t_2) is

$$\psi_{\mathrm{ri}}(t_1,t_2) = \frac{\bar{y}(t_1,t_2) - y_1(t_1,t_2)}{2\gamma(t_1,t_2)} + i\frac{y_2(t_1,t_2) - y_3(t_1,t_2)}{2\sqrt{2}\gamma(t_1,t_2)} \tag{5.208}$$

Then, the amplitude of the wavefunction is given by $\sqrt{\mathrm{Re}(\psi_{\mathrm{ri}})^2 + \mathrm{Im}(\psi_{\mathrm{ri}})^2}$ while the phase angle is given by $\arctan(\mathrm{Im}(\psi_{\mathrm{ri}})/\mathrm{Re}(\psi_{\mathrm{ri}}))$. However, the result of the actan function is limited to $(-\pi/2, \pi/2)$ while the true phase angle, $-(t_r - \bar{t}_r)\bar{\omega}_r - (t_i - \bar{t}_i)\bar{\omega}_i$, will exceed this range. Therefore, to estimate the phase information accurately, we

confine the phase to the range $-\pi/2 \leq (-(t_r - \bar{t}_r)\bar{\omega}_r - (t_i - \bar{t}_i)\bar{\omega}_i) \leq \pi/2$. By setting the measurement of the idler at $t_i = \bar{t}_i$, then the temporal measurement of the signal photon should be $-\frac{\pi}{2\bar{\omega}_r} + \bar{t}_r \leq t_r \leq \frac{\pi}{2\bar{\omega}_r} + \bar{t}_r$. Therefore, based on the estimation of $\bar{t}_r$ from the reconstruction of the JTI, this given period should be measured with a higher accuracy in order to obtain a more accurate estimation of the $\bar{\omega}_r$. This can be achieved by performing the temporal measurement with a higher resolution.

The information of the wavefunction at (t_r, t_i) can be obtained by performing the second-order correlation measurement of the output A at t_r and the output B at t_i with three different phase shifts $\phi = 0, \frac{\pi}{3}, \frac{2\pi}{2}$. This process will be repeated to construct the whole temporal wavefunction at different time instances.

At each time instance and phase shift, the experimental measurement of y contains some error, which is modeled by the Poisson statistics. Then, reconstruction of the wavefunction contains error due to the error propagation given in Eqs.5.207 and 5.208.

The numerical simulation of this interferometric measurement of the wavefunction of the SPDC signal is performed using Matlab and shown below.

5.4.2 Numerical Results

Theoretical Reconstruction

The original joint wavefunction of the signal and idler beams $\psi_{\text{si}}(t_s, t_i)$ can be constructed using the method above if no error is included in the measurement process as shown in the Fig.5.26. Fig.5.26a plots the amplitude of the theoretical signal and

idler joint wavefunction at t_s and t_i while Fig.5.26b plots the amplitude of the reconstructed wavefunction. The experimental values of σ_s^2 and σ_i^2 are both 12.57 $/(ps)^2$. Here, $\kappa = 0.93$ is assumed in the following section.

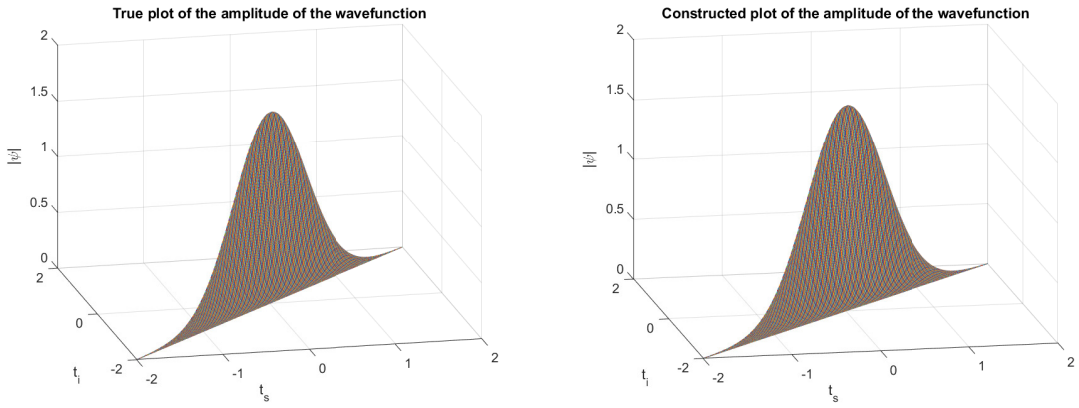

(a) The amplitude of true signal-idler wavefunction

(b) The amplitude of constructed wavefunction

Figure 5.26: The true and reconstructed wavefunction without error

The squared error between the true and reconstructed wavefunctions is shown in the following figure.

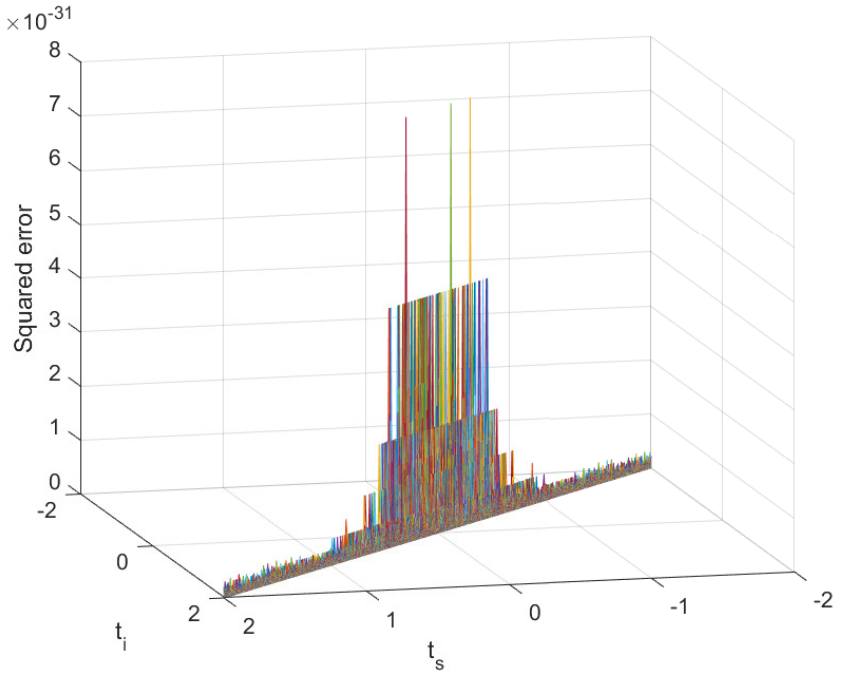

Figure 5.27: The difference between the true and reconstructed wavefunctions

It can be observed that the total squared error is around $6.18 * 10^{-28}$, which is negligible; therefore, it can be confirmed that applying this method can theoretically construct the wavefunction accurately.

The intensity measurement at detectors A and B in terms of the number of photons measured contains the quantum shot noise or quantum Poisson noise [85]. Therefore, the measured number of photons $\tilde{y}$ is governed by a Poisson distribution with its mean number of measured photons y. Then, the probability of measuring $\tilde{y}$ is given as

$$P(\tilde{y}) = \frac{y^{\tilde{y}}}{\tilde{y}!} e^{-y} \tag{5.209}$$

The final measured value of (t_r, t_i) can be obtained by taking the average of M

measurements $\tilde{y}(t_r, t_i) = \frac{1}{M}\sum_{m=1}^{M} \tilde{y}_m(t_r, t_i)$, which is expected to reduce the error. In our reconstruction here, we have M being $1, 10^2, 10^4, 10^5$.

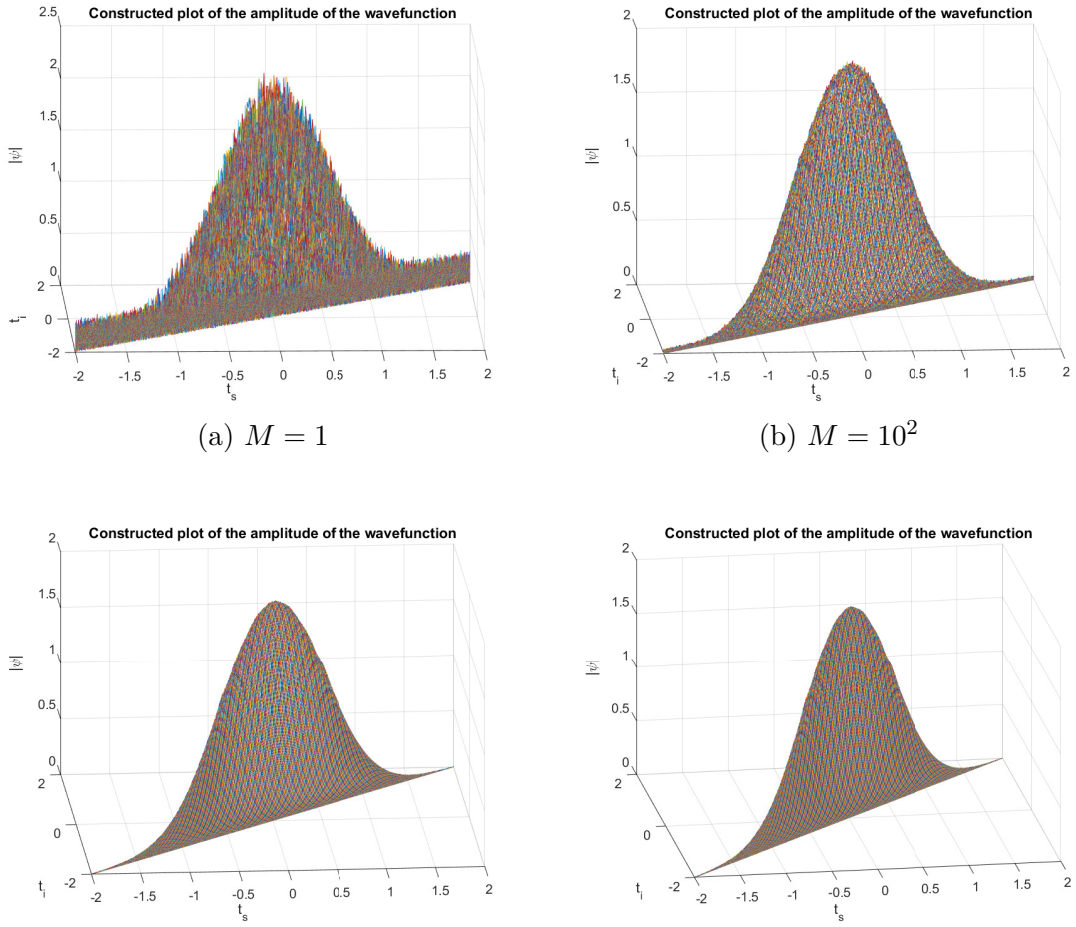

(a) $M = 1$ (b) $M = 10^2$

(c) $M = 10^4$ (d) $M = 10^5$

Figure 5.28: The reconstructed wavefunction with $M = 1, 10^2, 10^4, 10^5$ with error modeled by Poisson statistics

The error corresponding each value of M is shown in Fig.5.29.

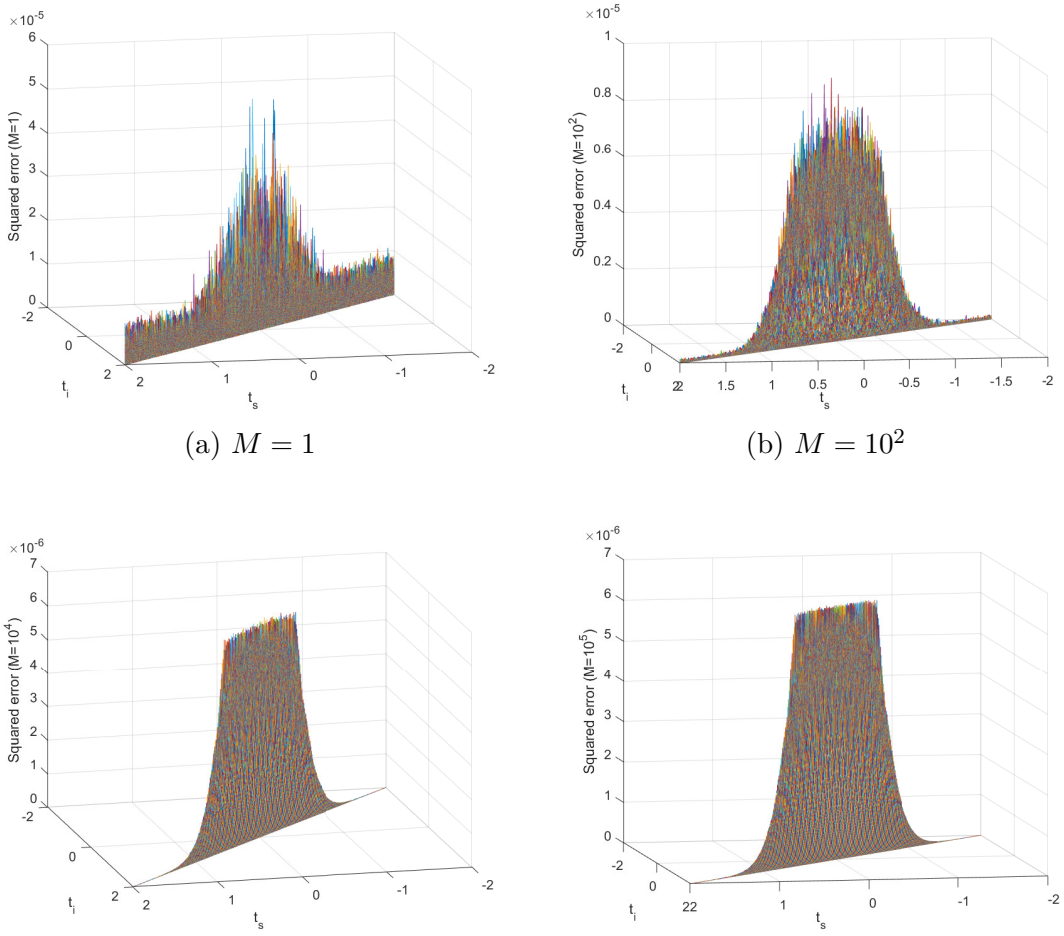

(a) $M = 1$ (b) $M = 10^2$

(c) $M = 10^4$ (d) $M = 10^5$

Figure 5.29: The reconstructed wavefunction with $M = 1, 10^2, 10^4, 10^5$ with error modeled by Poisson statistics

The total error in the reconstruction from 1 to 10^5 is listed in the Table.5.4.

M=	1	10	10^2	10^3	10^4	10^5
Squared Error	0.3561	0.0690	0.0407	0.0380	0.0378	0.0378

Table 5.4: The total squared error at different number of trials M

Increasing the number of trials from 1 to 10^3 can significantly reduce the error while this improvement is not obvious when M increases to a larger value. When M increases from 10^3 to 10^4, the total error only decreases about 0.0002; therefore, $M = 10^3$ will be adopted.

Ambiguity Function using Amplitude Reconstruction

The correlation between two theoretical wavefunctions at different velocity and range is

$$f_{\text{amp}}(v,d) = \int\int |\psi_{\text{ri}}(t_r,t_i)| \cdot |\psi_{\text{si}}^{(v,d)}(t_r,t_i)| dt_r dt_i \tag{5.210}$$

where ψ_{ri} is joint wavefunction of the return signal and idler photons. And $\psi_{\text{si}}^{(v,d)}$ denotes the wavefunction in Eq.5.172 with the known target distance d and known target velocity v. The corresponding time delay experienced is $2d/(c-v) = \tau_r(v,d)$. Then, the correlation function f_{amp} becomes

$$\begin{aligned} f_{\text{amp}}(\tau_r) &= \int\int |\psi_{\text{ri}}(t_r,t_i)| \cdot |\psi_{\text{si}}(t_r-\tau_r,t_i)| dt_r dt_i \\ &\propto \int\int \exp\left[-\sigma_s^2(t_r-\bar{t}_r)^2 - \sigma_i^2(t_i-\bar{t}_i)^2 + 2\kappa\sigma_s\sigma_i(t_r-\bar{t}_r)(t_i-\bar{t}_i)\right] \\ &\quad \cdot \exp\left[-\sigma_s^2(t_r-\bar{t}_s-\tau_r)^2 - \sigma_i^2(t_i-\bar{t}_i)^2 + 2\kappa\sigma_s\sigma_i(t_r-\bar{t}_r-\tau_r)(t_i-\bar{t}_i)\right] dt_r dt_i \\ &\propto \exp[-\frac{1}{2}\sigma_s^2(\bar{t}_r-\bar{t}_s-\tau_r)^2] \end{aligned} \tag{5.211}$$

Therefore, this function reaches its maximum value when $\bar{t}_r = \bar{t}_s + \tau_r$. This correlation function only concerns the amplitude of the wavefunction in Eq.5.172, which contains the information of the time delay. The information of the Doppler frequency shift is contained in the phase of the wavefunction.

The correlation function $f_{\text{amp}}(\tau_r)$ with variable velocity and range is computed as shown in Fig.5.30.

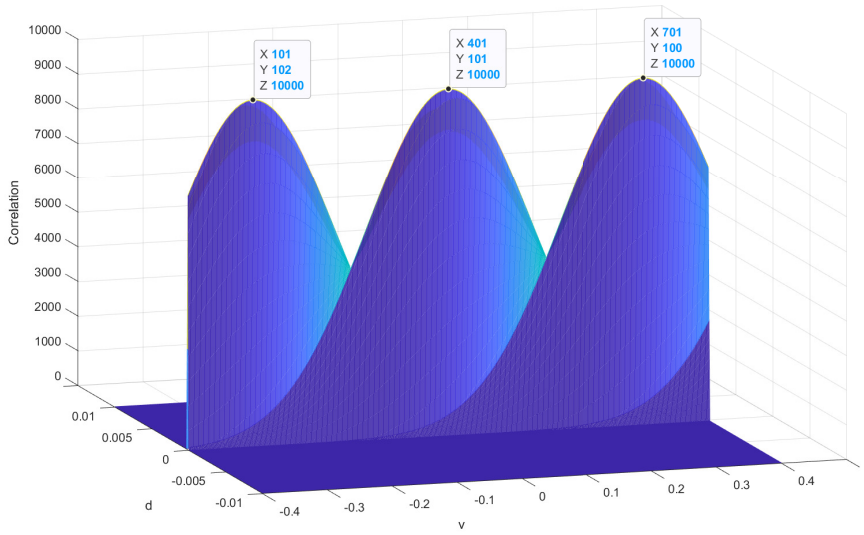

Figure 5.30: The correlation between two theoretical wavefunctions with different velocity and range

Fig.5.30 plots the correlation value at different combinations of estimated d and v. One combination of two values of d and v corresponds to one controlled time delay, $\tau_r = \frac{2d}{c-v}$, from which the correlation function is calculated. However, one value of, τ_r (corresponds to one value of the correlation function in Eq.(5.207)) can be achieved by multiple combinations of d and v. In this particular case, we examine the limited ranges of d and v in Fig.5.30 Within the limited ranges and with step sizes in these ranges being finite and discrete, we found three combinations of d and v ($d = 10^5 + 0.01m, v = 0.3m/s$, $d = 10^5 m, v = 0m/s$ and $d = 10^5 - 0.01m, v = -0.3m/s$) had the same time delay, τ_r. If the ranges of d and v are further expanded, we may find even more peaks. Such ambiguity makes the above method not useful.

We may, however, use the correlation function between the two wavefunctions with different $\bar{t}_r$ to first estimate the time delay of return photons, $\tilde{t}_r$, Then, the correlation function as a function of the controlled time delay τ_r is shown in Eq.5.207 and in Fig.5.31. In this figure, it is assumed that $\bar{t}_r = 0$ and τ_r in the reference signal and idler beams ranges from $-10ps$ to $10ps$. Moreover, it is assumed that the theoretical wavefunction is employed. It can be observed in Fig.5.31 that the correlation function reaches its unique maximum point when the time delays of these two functions are the same.

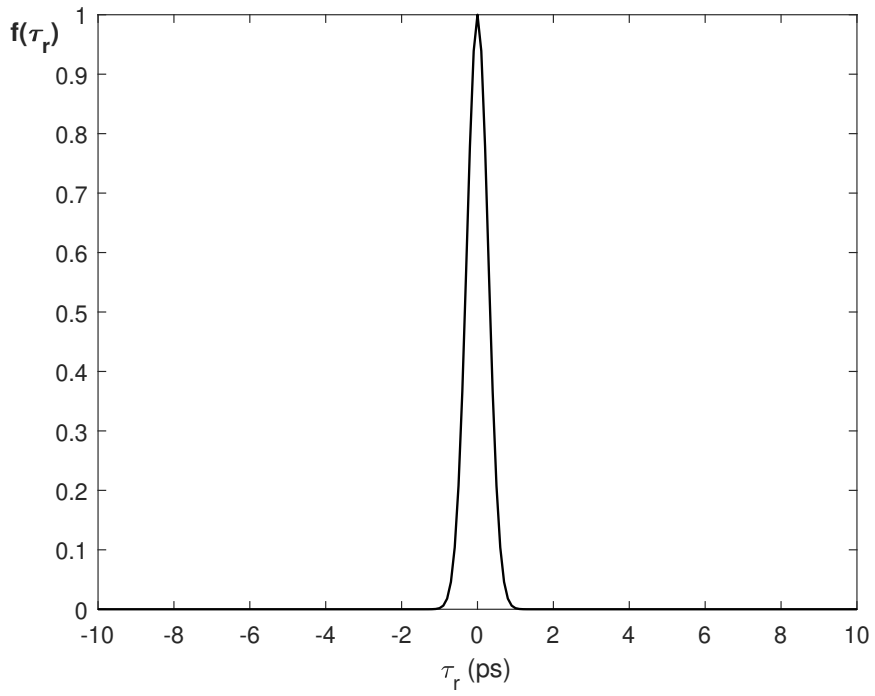

Figure 5.31: The correlation between the amplitude of the wavefunction with no time delay and the one with different time delay from -10ps to 10ps.

The reconstruction of the amplitude of the wavefunction as given in Eq.5.208 relies on the accurate measurements of y_1, y_2, y_3 at different time instances. Due to the error

introduced in the measurement process, the reconstructed amplitude of the wavefunction is affected, which is used to obtain the correlation function $f(\tau_r)$. When $M = 1$, as shown in Fig.5.29a, the reconstructed amplitude of the wavefunction is significantly affected by the measurement error. Then, the correlation function based on this reconstrcted wavefunction is investigated and shown in the blue line in Fig.5.32. Compared with the theoretical result in Fig.5.31, the sidelobe increases significantly. When M increases, the error in the reconstructed wavefunction becomes less significant. The sidelobe of the correlation function is suppressed when M increases as shown in Fig.5.32. In Fig.5.32, M increases from 1 to $10, 10^2, 10^3, 10^4$, it can be observed that when M increases from 1 to 10, the level of correlation at $\tau_r = 1$ps decreases sharply from 0.147 to 0.047. When M increases from 10 to 10^2, the level of correlation at $\tau_r = 1$ps reduces to 0.016. Moreover, this value becomes 0.006 for $M = 10^3$ and 0.004 for $M = 10^4$. Therefore, adopting $M = 10^3$ is desired, which can achieve a relatively low level of sidelobe.

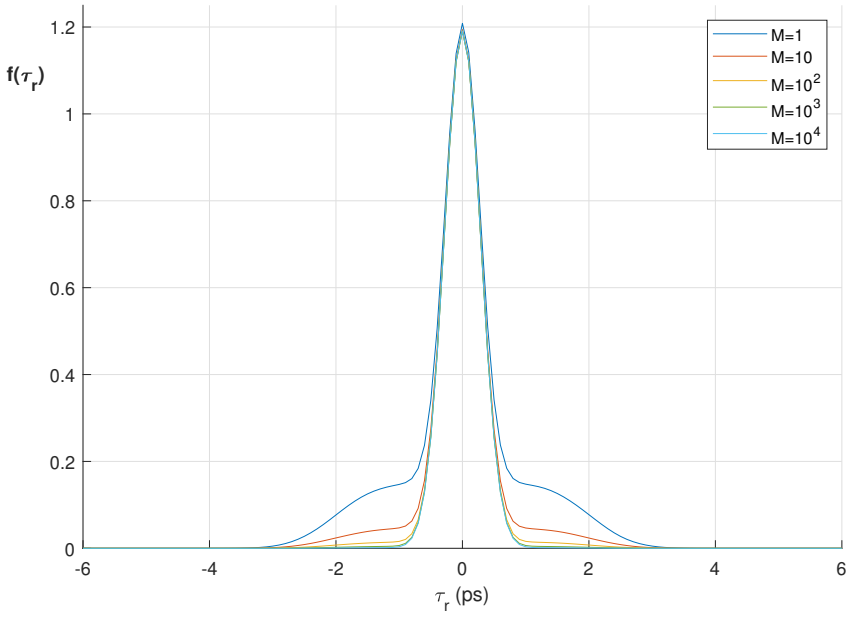

Figure 5.32: The correlation function at different time delays wih $M = 1, 10, 10^2, 10^3, 10^4$

Phase Reconstruction

The phase information in Eq.5.172 is $\arg(\psi_{\text{ri}}) = -(t_r - \bar{t}_r)\bar{\omega}_r - (t_i - \bar{t}_i)\bar{\omega}_i \triangleq \vartheta(t_r, t_i)$. If the time measurement of the idler beam is fixed at $\bar{t}_i$, then the measured phase information $\vartheta(t_r, t_i = \bar{t}_i) = -(t_r - \bar{t}_r)\bar{\omega}_r$ is a linear relationship with the time $(t_r - \bar{t}_r)$ whose slope provides an estimate of the central frequency $\bar{\omega}_r$. As stated above, the interested range of the time measurement is $t_r \in [-\frac{\pi}{2\bar{\omega}_r} + \bar{t}_r, \frac{\pi}{2\bar{\omega}_r} + \bar{t}_r]$ while $\bar{\omega}_r$ is given by $\frac{c-v}{c+v}\bar{\omega}_s$.

As the analysis in the description of the wavefunction reconstruction method, the reconstructed phase function is periodic and . If $v = 0m/s, d = 10^5 m$ is assumed

and the corresponding time delay is $\bar{t}_r = 6.6667 * 10^8$ ps, the measurement of the idler beam is fixed at $\bar{t}_i$. At the each value of t_r ranging from $\bar{t}_r - 2 * 10^{-3}$ ps to $\bar{t}_r + 2 * 10^{-3}$ ps with a step size 0.0001 ps, the return beam is measured and based on Eq.5.208, the wavefunction ψ_{ri} at (t_r, t_i) can be obtained in Eq.5.208, from which the phase information can be obtained. If no error is considered in this case, the reconstructed phase of the wavefuntion is shown in Fig.5.33 with $t_i = \bar{t}_i$. One period of the phase plot is $t_r \in [-\frac{\pi}{2\bar{\omega}_r} + \bar{t}_r, \frac{\pi}{2\bar{\omega}_r} + \bar{t}_r]$. Then, if $v = 0$ m/s, $\bar{\omega}_s = 2.2793 * 10^3$ rad/ps, then, the focused range of time measurement in the phase reconstruction will be $[\bar{t}_r - 0.0007, \bar{t}_r + 0.0007]$ in ps.Therefore, in the phase reconstruction process, the resolution of the time detection should be 0.0001ps.

With $v = 0, d = 10^5$,

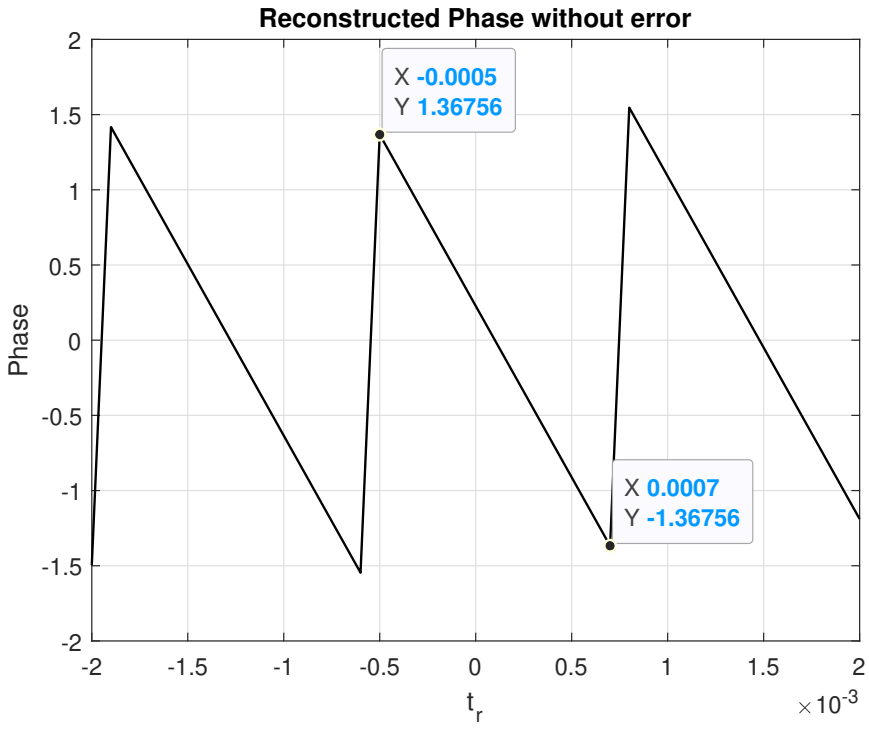

Figure 5.33: The reconstructed phase information over t_r without error

It can be observed in Fig.5.33 that the phase of the reconstructed wavefunction is periodic due to the periodicity of the arctan function. Within the period from $\bar{t}_r - 0.0007$ to $\bar{t}_r + 0.0007$, the slope of phase over time provides estimates of the frequency $\bar{\omega}_r$, which in this figure is $(1.36756 + 1.36756)/(12 * 0.0001) = 2.2793 * 10^3$ rad/ps. This is exactly the true value of the frequency.

The phase information of the wavefunction is obtained from Eq.5.208. Similar to the reconstruction of the amplitude of the wavefunction, the reconstruction of the phase of the wavefunction is also affected by the measurement inaccuracy as given in Eq.5.209. The reconstructed phase of wavefunction with different value of $M = 1, 10^2, 10^4, 10^5$.

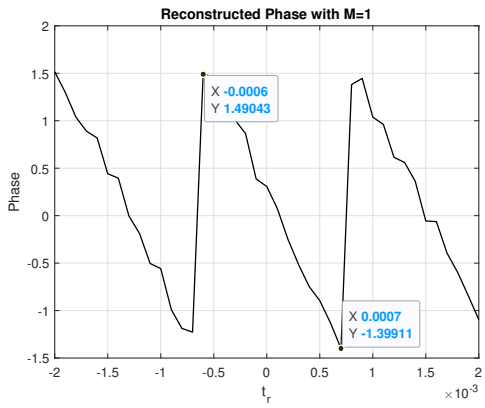

(a) $M = 1$. $\tilde{\omega}_r = 2222.7$ rad/ps

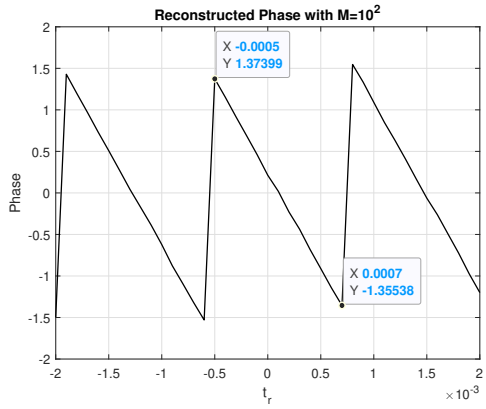

(b) $M = 10^2$. $\tilde{\omega}_r = 2274.5$ rad/ps

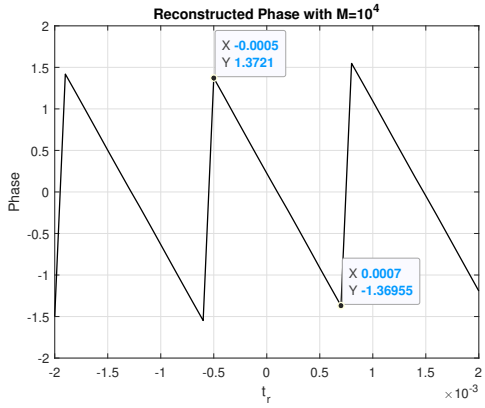

(c) $M = 10^4$. $\tilde{\omega}_r = 2284.7$ rad/ps

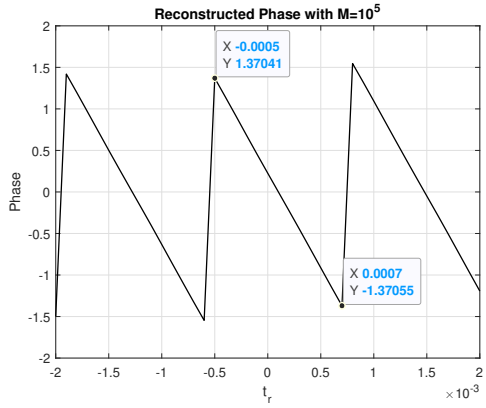

(d) $M = 10^5$. $\tilde{\omega}_r = 2284.1$ rad/ps

Figure 5.34: The reconstructed phase information with $M = 1, 10^2, 10^4, 10^5$ with error modeled by Poisson statistics

As shown in Fig.5.34, the phase information is heavily affected by the error introduced in the measurement process. Within one time segment $(\bar{t}_r - 5 * 10^{-4}, \bar{t}_r + 5 * 10^{-4})$ ps, the difference between the theoretical plot and the reconstructed plot with different M has been investigated and shown in the Table.5.5. Table.5.5 lists the sum of the squared error at $M = 1, 10, 10^2, 10^3$ and 10^4.

M=	1	10	10^2	10^3	10^4
	0.0803	0.016	0.0013	$3.17 * 10^{-4}$	$1.40 * 10^{-4}$

Table 5.5: The sum of the squared error between the theoretical plot and the reconstructed plot

As shown in the Table.5.5, the total error over the focused time period can be largely reduced by increasing the number of trials M. And this value becomes acceptably small when $M = 10^3$; therefore, similar to the conclusion in the analysis of the error in the reconstructed amplitude of the wavefunction, $M = 10^3$ is also suitable for the reconstruction of phase information.

Time and Frequency Estimation Method

Suppose we employ the joint wavefunction of the reference signal and the idler (which we designate the reference joint wavefunction) having same parameters $\sigma_s^2 = 12.57\text{rad/ps}, \sigma_i^2 = 12.57\text{rad/ps}, \kappa = 0.93$ as shown in Eq.5.172 for estimating the distance d and the velocity v of the target, and suppose we receive the same returned signal have the joint wavefunction, ψ_{ri}, of the returned signal and the idler as given by Eq. 5.172 with an unknown time delay and frequency shift. We want to estimate the distance and the velocity of the target using the above information. Now, suppose the interested range of the target parameters are $d \in [d_1, d_2]$ m and $v \in [v_1, v_2]$ m/s. It is assumed that the true distance and the true velocity of the target, denoted by (d_t, v_t), are within the two given ranges. Then, the time delay and frequency of the returned signal beam will be $\bar{\tau}_r = \frac{2d_t}{c-v_t}$ and $\bar{\omega}_r = \frac{c-v_t}{c+v_t}\bar{\omega}_s$. The aim of the estimation

problems in QI is to estimate $\bar{t}_r$ and $\bar{\omega}_r$, which will be used to further evaluate the parameters of the target, (d_t, v_t).

From the amplitude reconstruction section, we have learned that the parameter $\bar{t}_r$ can be estimated from the maximum point of the correlation function between $|\tilde{\psi}_{\text{ri}}|$ and $|\psi_{\text{si}}(\tau_r)|$ at different values of τ_r, where $\tilde{\psi}_{\text{ri}}$ is the joint wavefunction of the reconstructed returned signal and the idler (which we designate the *reconstructed joint wavefunction*), and $\psi_{\text{si}}(\tau_r)$ is the reference joint wavefunction. Thus, in our estimation procedure, the reference joint wavefunction with different time delays should first be obtained and stored for estimation analysis. Given that $d_t \in [d_1, d_2]$ m and $v \in [v_1, v_2]$ m/s, the minimum value of $\bar{t}_r$ will be $\bar{t}_r^{\min} = \frac{2d_1}{c-v_2} \times 10^{12}$ ps and the maximum value of $\bar{t}_r$ is $\bar{t}_r^{\max} = \frac{2d_2}{c-v_1} \times 10^{12}$ ps. As shown in Fig.5.31, without noise, the two joint wavefunctions will become uncorrelated when the time delay between them is larger than 2ps. This time-lapse becomes 3ps when the measurement error is taken into consideration as shown in Fig.5.32. Therefore, the controlled time delay increment in the reference joint wavefunction should be in 3ps steps. As given in Fig.5.26, the amplitude of the wavefunction will become zero when $t_r > \bar{t}_r + 2$ ps or $t_r < \bar{t}_r - 2$ ps. Therefore, at each value τ_r^i, the reference joint wavefunction $\psi_{\text{ri}}^{\tau_r^i}$ in the time range of $\tau_r^i - 2$ ps and $\tau_r^i + 2$ ps will be the section of interest. The reference joint wavefunction ψ_R^i corresponding to this time delay τ_r^i is given by

$$\psi_{\text{R}}^{\text{ß}}(t_r, t_i) = \begin{cases} \psi_{\text{ri}}^{\tau_r^i}(t_r, t_i), & \text{if } \tau_r^i - 2 \le t_r \le \tau_r^i + 2. \\ 0, & \bar{t}_r^{\min} - 2 \le t_r < \tau_r^i - 2 \text{ or } \tau_r^i + 2 < t_r \le \bar{t}_r^{\max} + 2. \end{cases} \tag{5.212}$$

The second step is to obtain the reconstructed joint wavefunction of the returned

signal and idler beam, $\tilde{\psi}_{\text{ri}}$ using the reconstruction method described in Section 5.5.1. The detection window of any returned signal is $t_r \in [\bar{t}_r^{\min} - 2, \bar{t}_r^{\max} + 2]$ ps with a time resolution 0.1 ps. The detection window of idler signal is $t_i \in [\bar{t}_i - 2, \bar{t}_i + 2]$ ps. From previous analysis, $M = 10^3$ is be adopted in the reconstruction process. Afterwards, the correlation between the reconstructed plot $\tilde{\psi}_{\text{ri}}$ and each of the theoretical plot ψ_{R}^i will be calculated as given as

$$f_{\text{amp}}(\tau_r^i) = \int_{\bar{t}_i - 2}^{\bar{t}_i + 2} \int_{\bar{t}_r^{\min} - 2}^{\bar{t}_r^{\max} + 2} \tilde{\psi}_{\text{ri}} \psi_R^{\tau_r^i} dt_r dt_i \tag{5.213}$$

Then, the time delay of the returned signal $\bar{t}_r$ will be estimated from the maximum value of the correlation function $f_{\text{amp}}(\tau_i)$,

$$\tilde{t}_r = \arg\max_{\tau_r^i} f_{\text{amp}}(\tau_r^i) \tag{5.214}$$

Here, $\tilde{t}_r$ denotes the estimated value of the time delay experienced by the returned signal.

After obtaining the estimate of the time delay, $\tilde{t}_r$, the phase characteristics of the wavefunction can be reconstructed. Due to the property of *actan* functions, the phase characteristics becomes a periodic function along t_r. Hence, the central point of the chosen range for the phase estimation is not critical but the range and the resolution are important. As stated above, the resolution should be 0.0001ps and the time duration of the measurement should be more than 0.0015 ps. In our case, the chosen range based on the estimated result $\tilde{t}_r$ is from $\tilde{t}_r - 0.0015$ ps to $\tilde{t}_r + 0.0015$ps with an increment 0.0001 ps. Then, the slope of the reconstructed phase plot gives the estimated frequency $\tilde{\omega}_r$.

Here, an example of this time and frequency estimation problem is provided. Suppose $d \in [(10^5 - 5)\text{m}, (10^5 + 5)\text{m}]$ and $v \in [-150\text{m/s}, 150\text{m/s}]$, $\bar{t}_r$ as defined in Eq.5.177 will be between $t_r^{\min} = 6.66633 \times 10^8$ ps to $t_r^{\max} = 6.667 \times 10^8$ ps. A a random value of d and v can be generated with its corresponding time delay $\bar{t}_r$. Then, the correlation function $f_{\text{amp}}(\tau_r)$ is plotted in Fig.5.35.

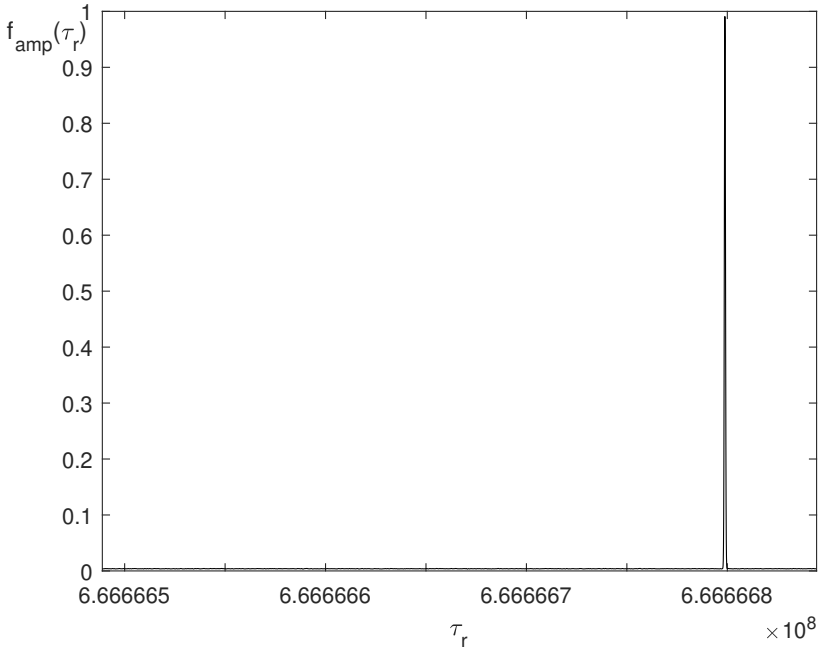

Figure 5.35: The correlation between the data of the theoretical wavefunction and the reconstructed wavefunction of the received and idler system with a time increment 0.1ps. The unit of τ_r is in ps. $M = 10^3$ is adopted.

From the peak of this correlation function $f_{\text{amp}}(\tau_r)$, the corresponding value of τ_r at this peak is $6.666666062889185 \times 10^8$ ps and the difference between the estimated time delay and true time delay $6.666666063074191 \times 10^8$ ps is $\tilde{t}_r - \bar{t}_r = -0.0185$ps. The normalized error as defined $\frac{\tilde{t}_r - \bar{t}_r}{\bar{t}_r}$ is -2.7751×10^{-11}. Now, using the estimated time delay $\tilde{t}_r$, the frequency of the returned signal can be estimated from the slope

of the reconstructed phase plot within $t_r \in (\tilde{t}_r - 0.0003, \tilde{t}_r + 0.0003)$. Then, the difference between the estimated frequency $\tilde{\omega}_r$ 2287.88576064177 rad/ps and the true frequency $\bar{\omega}_r$, 2279.26946064177 rad/ps, is $\tilde{\omega}_r - \bar{\omega}_r = 8.6163$ rad/ps. The normalized error $(\tilde{\omega}_r - \bar{\omega}_r)/\bar{\omega}_r$ in this case is 0.0038.

The numerical simulation is repeated for 10 times. At the each trial, a random value of distance and a random value of velocity are generated and known. Then, the wavefunction of the return signal and idler with a known time delay and known Doppler frequency shift is reconstructed using the above method. The time delay can be estimated from the peak of the correlation function.

The error of the time delay estimation in each trial has been computed as shown in Fig.5.36.

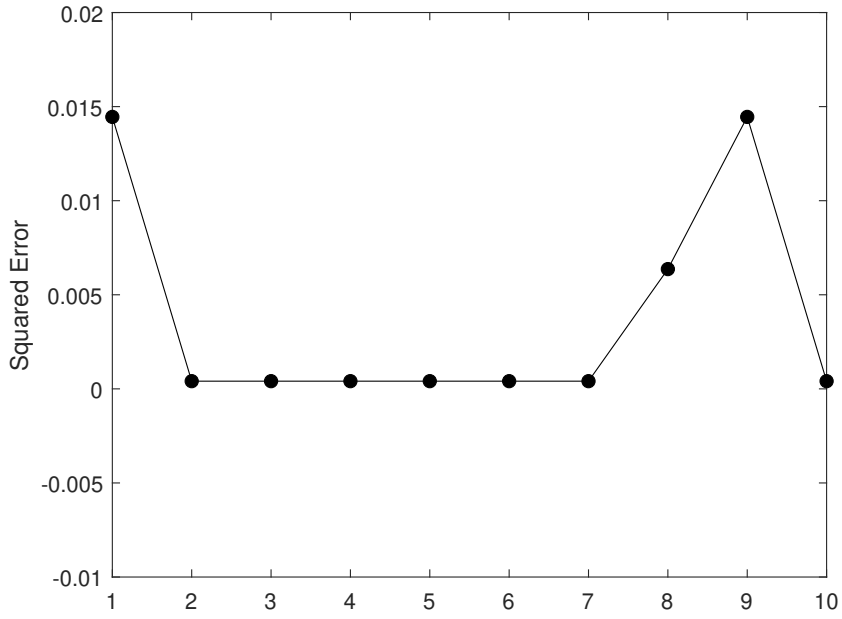

Figure 5.36: The error in estimating the time delay using the peak of the correlation function with $M = 10^3$

Fig.5.36 plots the squared error between the estimated time delay and the true time delay for 10 numerical experiments. The average squared error is 0.0038 ps^2, whose squared root value is 0.0616 ps. Given the estimated time delay $\tilde{t}_r$ with $M = 10^3$, the estimated frequecy of each trial is obtained and the absolute value of the difference between the estimated frequency and the true frequency is shown in Fig.5.37.

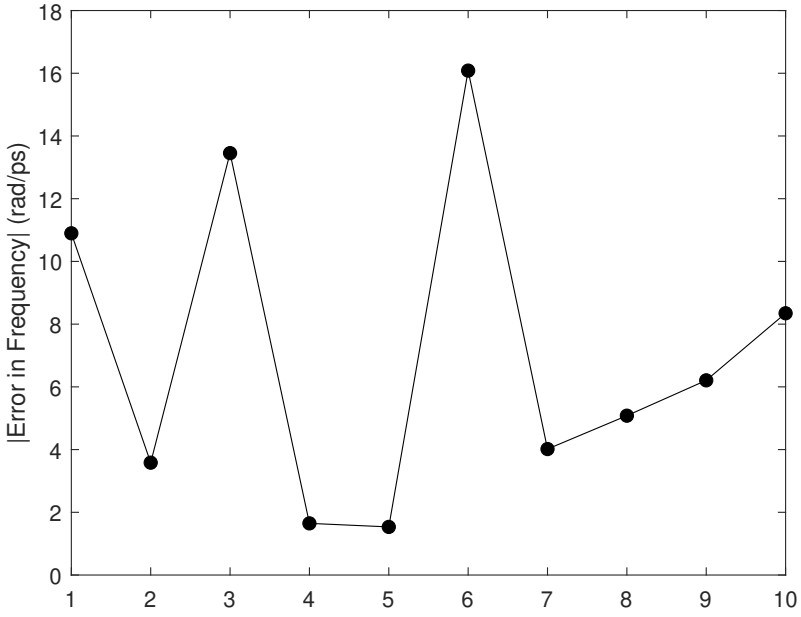

Figure 5.37: The error in estimating the frequency $M = 10^3$

Then, the averaged value of the absolute value of the error is 5.0401 rad/ps.

5.4.3 Summary

The joint intensity of the returned photon at t_1 and idler photon at t_2 is measured at three different phase angles $\phi = 0, \pi/3, 2\pi/3$, which give $y_1(t_1, t_2), y_2(t_1, t_2), y_3(t_1, t_2)$ respectively. The wavefunction at (t_1, t_2) as a complex number can be computed using these three measured results $y_1(t_1, t_2), y_2(t_1, t_2), y_3(t_1, t_2)$ based on Eq.5.208. The joint intensity of the returned photon and the idler photon is then measured over the interested time range: $t_1 \in [\bar{t}_r^{\min} - 2, \bar{t}_r^{\max} + 2]$ps with a step size 0.1ps and $t_2 \in [\bar{t}_i - 2, \bar{t}_i + 2]$ps with a step size 0.1ps. The amplitude and phase of each computed

value $y(t_1, t_2)$ are recorded respectively. Firstly, the amplitude of the measured result is focused. Given the discrete set of values measured at different time instances t_1, t_2, these are approximated by a joint Gaussian distribution as $|\tilde{\psi}_{\text{ri}}|$. This reconstruction of the amplitude of the wavefunction is used to compute the correlation with each reference wavefunction ψ_R^i in Eq.5.208. The best matched reference can be found, whose averaged time of the signal beam provides an estimated of τ_r, $\tilde{\tau}_r$. Secondly, the phase of the measured result is focused. At a fixed value of t_2, the phase of the measurement result is plotted at different values of t_1. This plot is approximated by a periodic linear function. The slope of the approximated function gives an estimate of $\bar{\omega}_r$, $\tilde{\omega}_r$. Then, with $\tilde{\omega}_r$ in Eq.5.174, the velocity of the target can be estimated $\tilde{v}$. Then, based on Eq.5.173, the target distance can be estimated using the estimated velocity and the time delay $\tilde{v}, \tilde{\tau}_r$.

5.5 Joint Estimation Method

5.5.1 Theoretical Description

The joint estimation method relies on the use of the SPDC output signal and idler beams which are governed by the wave functions in Eqs.5.169 and 5.170. A unitary transformation is applied on the SPDC signal and idler beams, which can preserve the Gaussian properties of the given system state. More specially, in this case, the applied unitary operator $\hat{\mathbf{B}}_{\text{si}}$ is given in Eq.5.215 which changes the joint state of having a signal photon at t_s and a idler photon at t_i to a time modified state with a

signal photon at $t_s + t_i$ and a idler photon at $\frac{t_s - t_i}{2}$.

$$\begin{aligned}\hat{\mathbf{B}}_{\mathrm{si}} &= \int\int |\frac{\omega_s + \omega_i}{2}\rangle_s \, |\omega_s - \omega_i\rangle_i \;\; {}_i\langle\omega_i|_s \, \langle\omega_s| \, d\omega_s d\omega_i \\ &= \int\int |t_s + t_i\rangle_s \, |\frac{t_s - t_i}{2}\rangle_i \;\; {}_i\langle t_i|_s \, \langle t_s| \, dt_s dt_i\end{aligned} \tag{5.215}$$

A systematic diagram of applying the joint estimation method on the SPDC outputs is shown in Fig.5.38. The practical implementation of this unitary operator can be found in Section 5.5.2.

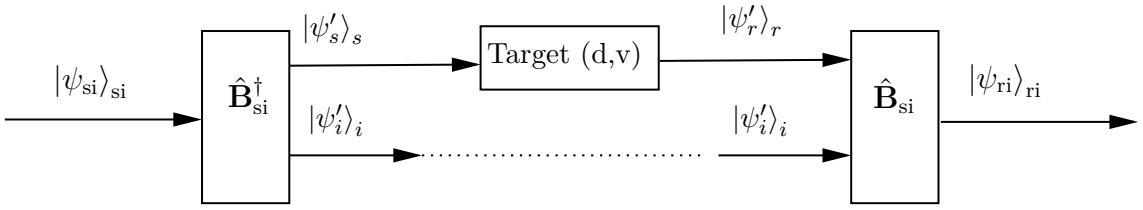

Figure 5.38: Systematic diagram of joint system estimation method relying on the unitary transformation and SPDC outputs.

If the input to this unitary transformation $\hat{\mathbf{B}}^{\dagger}_{si}$ is the SPDC wavefunction, the output becomes

$$\begin{aligned}|\psi'_{\mathrm{si}}\rangle &\triangleq \hat{\mathbf{B}}^{\dagger}_{si} \, |\psi_{\mathrm{si}}\rangle \\ &= \int\int \psi'_{\mathrm{si}}(t_s, t_i) \, |t_s\rangle_s \, |t_i\rangle_i \, t_s t_i\end{aligned} \tag{5.216}$$

where the new joint wavefunction $|\psi_{\mathrm{si}}\rangle'$ is given in the following

$$\begin{aligned}\psi'_{\mathrm{si}}(t_s, t_i) &\propto \exp\{-\frac{t_s^2}{16\tau_h^2} - \frac{i}{2}\omega_p t_s\} \cdot \exp\{-\frac{t_i^2}{\tau_r^2} - i\Delta\omega t_i\} \\ &= \psi'_{\mathrm{s}}(t_s) \cdot \psi'_{\mathrm{i}}(t_i)\end{aligned} \tag{5.217}$$

where $\omega_p = \bar{\omega}_s + \bar{\omega}_i$ and $\Delta\omega = \bar{\omega}_s - \bar{\omega}_i$. The new joint wavefunction $\psi'_{\mathrm{si}}(t_s, t_i)$ can be expressed as a direct product of the wavefunction of the signal beam ψ'_{s} and the

wavefunction of the idler beam ψ'_{i}. Then, the corresponding joint state becomes a tensor product of two independent states

$$\begin{aligned}
|\psi'_{\mathrm{si}}\rangle &= \int\int \psi'_{\mathrm{si}}(t_s, t_i)\,|t_s\rangle_s\,|t_i\rangle_i\,dt_s dt_i \\
&= \int\int \psi'_{\mathrm{s}}(t_s)\cdot\psi'_{\mathrm{i}}(t_i)\,|t_s\rangle_s\,|t_i\rangle_i\,dt_s dt_i \\
&= \int \psi'_{\mathrm{s}}(t_s)\,|t_s\rangle_s\,dt_s \cdot \int \psi'_{\mathrm{i}}(t_i)\,|t_i\rangle_i\,dt_i \\
&= |\psi'_{\mathrm{s}}\rangle_s \bigotimes |\psi'_{\mathrm{i}}\rangle_i
\end{aligned} \tag{5.218}$$

Therefore, the originally entangled signal and idler photons become unentangled and the joint wavefunction becomes the direct product of wavefunctions of the signal and idler. The unitary transformation $\hat{\mathbf{B}}_{\mathrm{si}}$ and $\hat{\mathbf{B}}^{\dagger}_{\mathrm{si}}$ can be implemented using the single-photon $\chi^{(2)}$ interactions and linear optics. Detailed implementation can be found in [86], [87].

Then, the transformed signal is sent to detect any possible target. Consequently, after encountering the target with a distance, d and a velocity v, the wavefunction of the returned signal with a time delay and Doppler frequency shift can be given as

$$\psi'_r(t_r) \propto \exp\left[-\frac{(t_r-\tau)^2}{16\tau_h^2} - \frac{i}{2}\omega'_p(t_r-\tau)\right] \tag{5.219}$$

where $\tau = \frac{2d}{c-v}$ is the time-delay and $\omega'_p = \frac{c-v}{c+v}\omega_p$ (is the shifted frequency).

The biphoton state at the receiver side is the joint state of the returned signal and

the retained idler beams

$$\begin{aligned}|\psi'_{ri}\rangle &= |\psi'_r\rangle_r \otimes |\psi'_i\rangle_i \\ &= \Big[\int \psi'_r(t_r)\,|t_r\rangle_r\,dt_r\Big] \otimes \Big[\int \psi'_i(t_i)\,|t_i\rangle_i\,dt_i\Big] \\ &= \int\int \psi'_r(t_r)\psi'_i(t_i)\,|t_r\rangle_r\,|t_i\rangle_i\,dt_r dt_i\end{aligned} \tag{5.220}$$

where

$$\psi'_i(t_i) \propto \exp\{-\frac{t_i^2}{\tau_r^2} - i\Delta\omega t_i\} \tag{5.221}$$

where t_i is the generation time of the idler photon and $\Delta\omega = \bar{\omega}_s - \bar{\omega}_i$.

At this step, all information about the target is contained in the received signal photon. Then, the unitary operator as defined in Eq.5.215 is applied at the receiver signal and idler, forming $\hat{\mathbf{B}}_{si}\,|\psi'_{\mathrm{ri}}\rangle$ so that the final idler beam is also related to the range and velocity of the target.

$$\begin{aligned}\hat{\mathbf{B}}_{ri}\,|\psi'_{ri}\rangle \propto \int\int &\exp\left[-\frac{[(t_r-\tau/2)+(t_i-\tau/2)]^2}{16\tau_h^2} - \frac{[(t_r-\tau/2)-(t_i-\tau/2)]^2}{4\tau_r^2}\right] \\ &\cdot \exp\left[-\frac{i}{2}(t_r-\tau/2)\cdot\frac{2c}{c-v}\bar{\omega}_s - \frac{i}{2}(t_i-\tau/2)\cdot\frac{2c}{c-v}\bar{\omega}_i\right]|t_r\rangle_r\,|t_i\rangle_i\,dt_r dt_i \\ &\triangleq |\psi_{\mathrm{ri}}\rangle\end{aligned} \tag{5.222}$$

Then, in Eq.5.222, the averaged time of arrival of either returned signal and idler is delayed with $\tau/2$. Also, the averaged frequency of the final returned signal $\frac{2c}{c-v}\bar{\omega}_s$ and idler beams $\frac{2c}{c-v}\bar{\omega}_i$ is associated with the target velocity. We employ the time

measurement operator $\hat{\mathbf{t}}_r$ as defined

$$\hat{\boldsymbol{t}}_r = \int t_r \left|t_r\right\rangle \left\langle t_r\right| dt_r \tag{5.223}$$

which is applied on the final returned signal beam. The frequency measurement operator $\hat{\boldsymbol{\omega}}_i$ is also employed which is defined as

$$\hat{\boldsymbol{\omega}}_i = \int \omega_i \left|\omega_i\right\rangle \left\langle \omega_i\right| d\omega_i \tag{5.224}$$

This frequency operator is applied on the final idler beam.

The expected result of applying the time measurement operator $\hat{\mathbf{t}}_r$ on the returned final returned signal is given as

$$\tilde{t}_r \triangleq \mathrm{tr}(\hat{\mathbf{t}}_r \boldsymbol{\rho}_r) \tag{5.225}$$

where $\boldsymbol{\rho}_r$ represents the returned signal that can be obtained by performing the partial trace on the joint state of the returned signal and idler, $\boldsymbol{\rho}_{\mathrm{ri}}$ over the idler beam

$$\boldsymbol{\rho}_{\mathrm{r}} = \mathrm{tr}_i(\left|\psi_{\mathrm{ri}}\right\rangle \left\langle \psi_{\mathrm{ri}}\right|) = \int \left\langle t_i|\psi_{\mathrm{ri}}\right\rangle \left\langle \psi_{\mathrm{ri}}|t_i\right\rangle dt_i \tag{5.226}$$

Then, the expected output of the time operator is

$$\tilde{t}_r = \frac{\tau}{2} \tag{5.227}$$

The expected value of applying the frequency operator $\hat{\omega}_i$ on the idler beam is defined as

$$\tilde{\omega}_i = \mathrm{tr}(\hat{\boldsymbol{\omega}}_i \boldsymbol{\rho}_i) \tag{5.228}$$

where $\boldsymbol{\rho}_i$ can be obtained as

$$\boldsymbol{\rho}_{\mathrm{i}} = \mathrm{tr}_r(|\Psi\rangle_{\mathrm{ri}} \langle\Psi|_{\mathrm{ri}}) = \int \langle\omega_r|\Psi_{\mathrm{ri}}\rangle \langle\Psi_{\mathrm{ri}}|\omega_r\rangle \, d\omega_r \tag{5.229}$$

Then, the expected output of the frequency operator is

$$\tilde{\omega}_i = \bar{\omega}_i - \frac{v}{c+v}\omega_p \tag{5.230}$$

Therefore, from the time measurement and the frequency measurement, both the time delay and the velocity-related frequency can be estimated. In the above method, the use of the unitary operator $\hat{\mathbf{B}}^{\dagger}$ to disentangle the signal and idler and then to re-entangle using $\hat{\mathbf{B}}$ are necessary this is because two resulting beams after being disentangled still share common parameters $\bar{t}_s$ and $\bar{t}_i$. The separated signal beam being sent out is returned with the information of the time delay and Doppler frequency shift, which is embedded in the parameter of this separated signal beam. The unitary operator $\hat{\mathbf{B}}$ then recombines the return signal and idler beams such that both beams still share common parameters $\bar{t}_r$ and $\bar{t}_i$.

5.5.2 Numerical Results

Practically, one signal photon and one idler photon will be generated at the time t_s and t_i with the probability $|\psi_{\mathrm{si}}(t_s, t_i)|^2$ and the frequencies of the generated signal and idler are ω_s and ω_i with the probability $|\Psi_{\mathrm{si}}(\omega_s, \omega_i)|^2$. After applying the unitary transformation $\hat{\mathbf{B}}_{\mathrm{si}}$, the signal photon shifted to $(t_s + t_i)$ and with the frequency $(\omega_s + \omega_i)/2$ is sent outwards. The unitary transformation $\hat{\mathbf{B}}_{\mathrm{si}}^{\dagger}$ will be applied on the

returned signal photon and retained idler, which will generate a signal photon at the time $t_s + \tau/2$ and a idler photon with the frequency $\frac{c}{c+v}\omega_i - \frac{v}{c+v}\omega_s$. Then, the arrival time of the return signal photon and the frequency of the idler photon are measured.

When a large number of signal and idler photons, M, are generated sequentially, the arrival time of each return time is measured and then the histogram of t_r can be obtained as $\{P(t_n)\}$ with $t_n = t_{\min} + (n-1) * \Delta T$. When M increases to a sufficiently large number, the histogram will become $|\psi_r(t_r)|^2$ which is given as

$$|\psi(t_r)|^2 \propto \exp\Big[- \frac{(t_r - \tau/2)^2}{(\tau_r^2 + 4\tau_h^2)}\Big] \tag{5.231}$$

The estimated result based on the obtained histogram is given as

$$t_{\text{est}} = \sum t_n P(t_n) \tag{5.232}$$

When $M = 10^3$, the histogram of the measured time of the returned signal and the histogram of the measured frequency of the idler are shown in Fig.5.39.

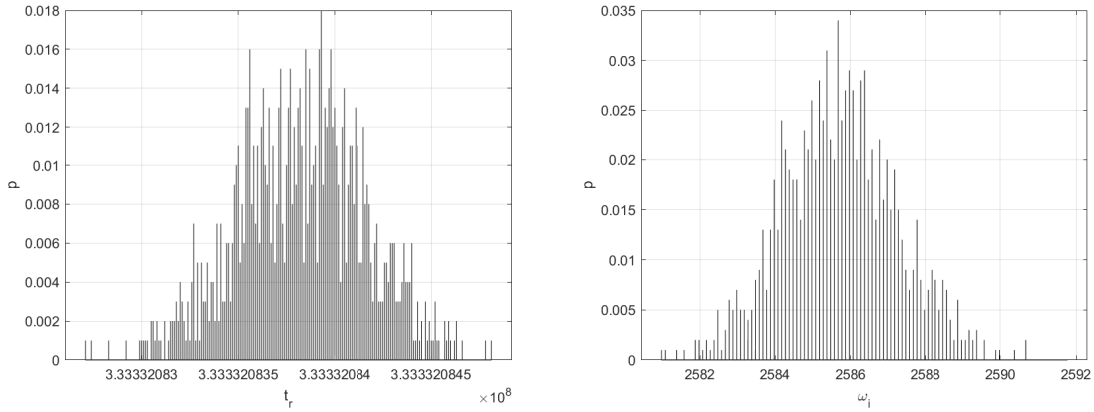

(a) The histogram of the time of arrival of return photons.

(b) The histogram of the frequency of idler photons.

Figure 5.39: Time and frequency histograms at $M = 10^3$

The difference between the estimated time delay and the true value is 0.0025 ps while the error in the frequency estimation is 2.5809 rad/ps.

When $M = 10^5$,

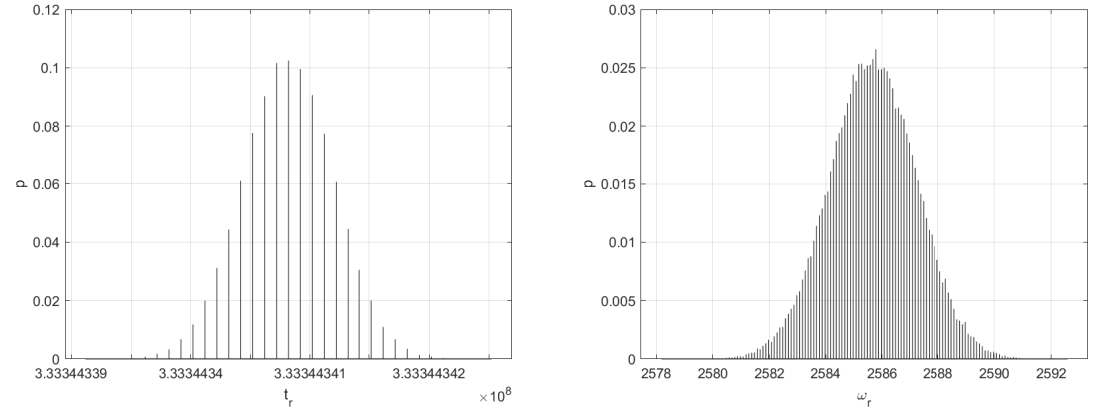

(a) The histogram of the time of arrival of return photons.

(b) The histogram of the frequency of idler photons.

Figure 5.40: Time and frequency histograms at $M = 10^5$

The difference between the estimated value t_{est} and theoretical value of $\tau/2$ is 0.0015ps. The difference between the estimated value and theoretical value of $\bar{\omega}_i - \frac{v}{c+v}\omega_p$ is 0.0183 rad/ps. Correspondingly, the range and velocity can be estimated using the estimated time and frequency.

Chapter 6

Conclusions and Future Study

6.1 Conclusions

Quantum illumination (QI), which is one special type of quantum radar system, relies on the phenomenon of quantum entanglement to enhance the performance of the target detection and parameter estimation over classical radar systems. The QI system commonly uses the entangled signal and idler beams generated by the spontaneous parametric down-conversion (SPDC) process to probe the interested region. This thesis investigates the application of QI as a quantum radar system to the practical problems of target detection and target range and velocity estimation.

The target detection problem in QI discriminates between two Gaussian states under two hypotheses. Each Gaussian state is fully characterized by its mean vector and covariance matrix. The entanglement between the signal and idler beams reflects on

the off-diagonal terms of the covariance matrix. Researchers have shown the superior performance bound of quantum illumination in terms of the probability of error of target detection, which can achieve 6 dB improvement in the error exponent compared with the classical illumination systems [9]. However, previously proposed quantum detector designs cannot achieve this desired performance. The first practical detector design proposed in [47] employed one optical parametric amplifier (OPA) which could introduce a 3 dB improvement.

In this thesis, dual-OPA detector design consisting of two optimized OPAs has been proposed. The adjustment between the power gains of two OPAs further decreases the probability of error in the one-OPA design. A comprehensive analysis of the noise effect and linearity constraint of OPAs on the detector performance of the amplifiers has also been included. However, results from the analysis this two-OPA design show that the optimal bound cannot be reached.

In this thesis, it was noted that both the one-OPA and two-OPA designs depend on the difference of the measured system output intensity, which uses the partial knowledge of the difference of the covariance matrices of two Gaussian states. Thus, another quantum detector was proposed such that the information of the complete covariance matrix of the Gaussian states was exploited. Here, the covariance matrix of the return signal and idler beams was first constructed by a homodyne detector with a quarter-wave plate and a half-wave plate. For H_0 (no target), the corresponding covariance matrix $\tilde{\mathbf{\Gamma}}_0$ was first constructed. Then, the distance between $\tilde{\mathbf{\Gamma}}_0$ and a reconstructed covariance matrix $\tilde{\mathbf{\Gamma}}$ was calculated and used as our test statistic. This distance value was then compared with the pre-determined threshold value which was established

based on the constant false alarm rate (CFAR) criteria. For distance measure between two covariance matrices, we first employed the most commonly used Euclidean distance (ED). However, since covariance matrices are Hermitian and positive semi-definite and therefore form a manifold in the signal space, a Riemannian distance (RD) was then thought to be more appropriate in this case. We further developed and applied a weighted Riemannian distance (WRD) aiming at optimally using the prior information of the measured covariance matrices of noise only, and employed WRD as a performance-improving measure. The performance of the CM detector using all the three ED, RD and WRD distance measures was explored. Among them, the CM detector using the WRD achieved the best detection performance followed closely by the use of the RD. It was further found that the error probability of any of the CM detectors is below the upper bound evaluated for an optimal detector design.

So far, very few papers have been published suggesting range and velocity estimation using quantum illumination. In this thesis, we investigated the problem of target parameter estimation using the model of QI. Our study on target parameter estimation is focused on the estimation of the target range and the target velocity. Accuracy in the estimation of these parameters in classical statistical signal processing, are measured in terms of the standard deviation which, for a unbiased estimate, is lower bounded by the classical Cramer-Rao bound. This concept has been extended to the quantum estimation problem. Here, as in the classical case, the range and the velocity of a target involves the simultaneous estimation of the averaged time of arrival and averaged frequency of the return signal. Inspired by [23], in which the quantum Cramer-Rao bound of this multiparameter estimation problem was developed, in this

thesis, the lower bound of the joint standard deviation in the simultaneous estimation of two systematic parameters, i.e., the averaged time of arrival and averaged frequency of the return signal, was derived. In the noiseless case, it was found to be governed by the entanglement factor κ.

Then, this thesis has derived the joint wavefunction of the return signal and idler when the wavefunction of any external effect is modeled by a Gaussian function. Afterwards, the corresponding quantum Cramer-Rao bound with this inaccuracy consideration has been obtained which depends on the Signal-to-Noise ratio. Results have shown that the impact of the noise on the measurement accuracy becomes less significant when the degree of the entanglement in the system increases.

This thesis has investigated two estimation methods. The first method exploited the reconstruction of the temporal wavefunction of the returned signal and idler beams. The information of these two parameters is incorporated in the phase and amplitude of the temporal wavefunction of the returned signal and idler beams. Hence, the first estimation method proposed in this thesis is based on the reconstruction of the phase and amplitude of the wavefunction. The wavefunction can be reconstructed reliably by combining the returned signal-idler pair and a pair of coherent signals. The error in the reconstruction can be lowered to be negligible when the number of trials is 10^3. The time delay could be estimated from the ambiguity function between the reconstructed wavefunction and the reference wavefunction. Then, given the estimated time delay, the Doppler frequency can be estimated from the slope of the reconstructed phase information of the wavefunction.

The second estimation method proposed in this thesis performed the unitary transformation on both the SPDC signal and idler beams and the returned signal and idler beams. Then, the averaged time of arrival of both the final returned signal and idler beams contained the information of the time delay due to the propagation process. Moreover, the averaged frequency of both beams was affected by the target velocity. Therefore, the estimation of the time delay is performed on the final signal beam and the estimation of the Doppler frequency is carried out on the final idler beam simultaneously. The second estimation method could achieve higher accuracy and requires lower detection resolution.

6.2 Future Study

Current research [7], [8] on QI employs a simplified model to describe the whole propagation process of the signal photon beam such that

$$\hat{\mathbf{a}}_r = \sqrt{\eta}\hat{\mathbf{a}}_s + \sqrt{1-\eta}\hat{\mathbf{a}}_b \tag{6.233}$$

where $\hat{\mathbf{a}}_r$, $\hat{\mathbf{a}}_s$ and $\hat{\mathbf{a}}_b$ represent respectively the annihilation operators of the received signal, the original transmitted signal and the background noise. The scalar parameter, η, called the *system transmissivity*, encompasses the effects of propagation loss, interference and scattering and also the target interaction. Current research successes demonstrate that QI has performance superior to classical radars for detecting weak targets under very noisy conditions. However, the analysis and design of the detectors are based on the simplified signal model of Eq.6.233, which describes the state of

the returned signal simply as a scaled version of the state of the originally transmitted signal, omitting the actual channel interference and scattering effects that may lead to the loss of entanglement between signal and idler photons. Thus, in practice, the application of the above target detectors in quantum radar may result in serious deterioration of performance.

Then, the development of a comprehensive model which describes the real-time transmission of the signal photon through an interfering, attenuating, and scattering medium, enabling the investigation of the entanglement decoherence during the propagation process should be focused.

Since the loss of entanglement between the received signal photon and the idler photon may cause serious performance deterioration of the detector, we seek for the possible recovery of the entanglement by passing the received signal through a different interfering medium, i.e., an *entanglement restorer*, which may *equalize* the loss in entanglement due to propagation. The equalized returned signal photon is then passed on for detection. It is hoped that the deterioration of performance of the CM detector may also be recovered.

Bibliography

[1] M. Skolnik, Introduction to Radar System. McGraw-Hill, New York, 2001.

[2] M. Lanzagorta and J. Uhlmann, "Opportunities and challenges of quantum radar," IEEE Aerospace and Electronic Systems Magazine, vol. 35, no. 11, pp. 38–56, 2020.

[3] M. Lanzagorta, Quantum Radar. Morgan and Claypool, San Rafael, CA, USA, 2012.

[4] L. Maccone and C. Ren, "Quantum radar," Physical Review Letters, vol. 124, no. 20, p. 200 503, 2020.

[5] B. Balaji, "Quantum radar: Snake oil or good idea?" Proc. Int. Carnahan Conf. Secur. Technol pp. 1–7, Oct., 2018.

[6] M. Lanzagorta and J. Uhlmann, "Opportunities and challenges of quantum radar," IEEE A&E Systems Magazine, pp. 38–56, November 2020.

[7] S. Lloyd, "Enhanced sensitivity of photodetection via quantum illumination," Science, vol. 321, no. 5895, pp. 1463–1465, 2008.

[8] S.-H. Tan, B. I. Erkmen, V. Giovannetti, et al., "Quantum illumination with gaussian states," Physical review letters, vol. 101, no. 25, p. 253 601, 2008.

[9] S. Guha and B. I. Erkmen, "Gaussian-state quantum-illumination receivers for target detection," Physical Review A, vol. 80, no. 5, p. 052 310, 2009.

[10] S. Zhang, X. Zou, J. Shi, J. Guo, and G. Guo, "Quantum illumination in the presence of photon loss," Physical Review A, vol. 90, no. 052308, 2014.

[11] S. Barzanjeh, S. Guha, C. Weedbrook, D. Vitali, J. H. Shapiro, and S. Pirandola, "Microwave quantum illumination," Physical Review Letters, vol. 114, no. 080503, 2015.

[12] K. Liu, Q.-W. Zhang, Y.-J. Gu, and Q.-L. Li, "Discrete-variable quantum illumination with ancillary degrees of freedom," Physical Review A, vol. 95, no. 042317, 2017.

[13] J. Shapiro, "The quantum illumination story," IEEE Aerospace and Electronic Systems Maga vol. 35, no. 4, pp. 8–20, 2020.

[14] F. Wong, J. Shapiro, and T. Kim, "Efficient generation of polarization-entangled photons in a nonlinear crystal," Laser physics, vol. 16, no. 11, pp. 1517–1524, 2006.

[15] R. Demkowicz-Dobrzanski and L. Maccone, "Using entanglement against noise in quantum metrology," Physical Review Letters, vol. 113, no. 250801, 2014.

[16] Z. Zhang, S. Mouradian, F. Wong, and J. H. Shapiro, "Entanglement-enhanced sensing in a lossy and noisy environment," Physical Review Letters, vol. 114, no. 110506, 2015.

[17] Q. Zhuang, Z. Zhang, and J. H. Shapiro, "Optimum mixed-state discrimination for noisy entanglement-enhanced sensing," Physical review letters, vol. 118, no. 4, p. 040 801, 2017.

[18] Q. Zhuang, Z. Zhang, and J. Shapiro, "Entanglement-enhanced neyman-pearson target detection using quantum illumination," J. Opt. Soc. Am. B, vol. 34, no. 8, pp. 1567–1572, 2017.

[19] S. Barzanjeh, S. Pirandola, D. Vitali, and J. M. Fink, "Microwave quantum illumination using a digital receiver," Science Advances, vol. 6, no. 19, eabb0451, 2020.

[20] G. Sorelli, F. Grosshans, and F. Boust, "Detecting a target with quantum entanglement," Research Report, ONERA, hal-02877841f, pp. 1–30, 2020.

[21] S. Gallot, D. Hulin, and J. Lafontaine, Riemannian Geometry. Springer, 2004.

[22] Y. Li and K. M. Wong, "Riemannian distances for signal classification by power spectral density," IEEE Journal of Selected Topics in Signal Processing, vol. 7, no. 4, pp. 655–669, 2013.

[23] Z. Huang, C. Lupo, and P. Kok, "Quantum-limited estimation of range and velocity," PRX Quantum, vol. 2, no. 3, p. 030 303, 2021.

[24] P. A. M. Dirac, "A new notation for quantum mechanics," in Mathematical Proceedings of the Cambridge University Press, vol. 35, 1939, pp. 416–418.

[25] S. L. Braunstein and P. Van Loock, "Quantum information with continuous variables," Reviews of modern physics, vol. 77, no. 2, p. 513, 2005.

[26] S. Pirandola, A. Serafini, and S. Lloyd, "Correlation matrices of two-mode bosonic systems," Physical Review A, vol. 79, no. 5, p. 052 327, 2009.

[27] J. Williamson, "On the algebraic problem concerning the normal forms of linear dynamical systems," American journal of mathematics, vol. 58, no. 1, pp. 141–163, 1936.

[28] K. D. Ikramov, "On the symplectic eigenvalues of positive definite matrices," Moscow University Computational Mathematics and Cybernetics, vol. 42, pp. 1–4, 2018.

[29] A. Einstein, B. Podolsky, and N. Rosen, "Can quantum-mechanical description of physical reality be considered complete?" Physical review, vol. 47, no. 10, p. 777, 1935.

[30] L.-M. Duan, G. Giedke, J. I. Cirac, and P. Zoller, "Inseparability criterion for continuous variable systems," Physical review letters, vol. 84, no. 12, p. 2722, 2000.

[31] A. Peres, "Separability criterion for density matrices," Physical Review Letters, vol. 77, no. 8, p. 1413, 1996.

[32] R. Simon, "Peres-horodecki separability criterion for continuous variable systems," Physical Review Letters, vol. 84, no. 12, p. 2726, 2000.

[33] K. Życzkowski, P. Horodecki, A. Sanpera, and M. Lewenstein, "Volume of the set of separable states," Physical Review A, vol. 58, no. 2, p. 883, 1998.

[34] G. Vidal and R. F. Werner, "Computable measure of entanglement," Physical Review A, vol. 65, no. 3, p. 032 314, 2002.

[35] C. H. Bennett, D. P. DiVincenzo, J. A. Smolin, and W. K. Wootters, "Mixed-state entanglement and quantum error correction," Physical Review A, vol. 54, no. 5, p. 3824, 1996.

[36] G. Giedke, M. M. Wolf, O. Krüger, R. F. Werner, and J. I. Cirac, "Entanglement of formation for symmetric gaussian states," Physical review letters, vol. 91, no. 10, p. 107 901, 2003.

[37] B. Jin, D. Mishra, and C. Argyropoulos, "Efficient single-photon pair generation by spontaneous parametric down-conversion in nonlinear plasmonic metasurfaces," Nanoscale, vol. 13, no. 47, pp. 19 903–19 914, 2021.

[38] V. Giovannetti, S. Lloyd, and L. Maccone, "Quantum-enhanced measurements: Beating the standard quantum limit," Science, vol. 306, no. 5700, pp. 1330–1336, 2004.

[39] L. Accardi, A. Frigerio, and V. Gorini, Quantum probability and applications to the quantum
Springer, 2006, vol. 1055.

[40] V. Braginsky and F. Y. Khalili, Quantum measurement, cambridge university press, 1992.

[41] R. Loudon, The quantum theory of light. OUP Oxford, 2000.

[42] F. Fei, X. Jiang-meng, M. Jing-ting, L. Zun-long, and Z. Wei-jie, "Quantum lidar based on squeezed sates of light," Acta Photonica SINICA, vol. 46, no. 5, 2017.

[43] A. D. McAulay, Military laser technology for defense: Technology for revolutionizing 21st cen
John Wiley & Sons, 2011.

[44] G. Burdge, G. Deibner, J. Shaprio, et al., "Quantum sensors program," HARRIS CORP MELBOURNE FL, Tech. Rep., 2009.

[45] R. Gallego Torromé, "Quantum illumination with multiple entangled photons," Advanced Quantum Technologies, vol. 4, no. 11, p. 2 100 101, 2021.

[46] V. Giovannetti, S. Lloyd, and L. Maccone, "Quantum-enhanced positioning and clock synchronization," Nature, vol. 412, no. 6845, pp. 417–419, 2001.

[47] S. Guha, "Receiver design to harness quantum illumination advantage," in 2009 IEEE International Symposium on Information Theory, IEEE, 2009, pp. 963–967.

[48] E. Lopaeva, I. R. Berchera, I. P. Degiovanni, S. Olivares, G. Brida, and M. Genovese, "Experimental realization of quantum illumination," Physical review letters, vol. 110, no. 15, p. 153 603, 2013.

[49] Z. Zhang, S. Mouradian, F. N. Wong, and J. H. Shapiro, "Entanglement-enhanced sensing in a lossy and noisy environment," Physical review letters, vol. 114, no. 11, p. 110 506, 2015.

[50] B. Balaji and D. England, "Quantum illumination: A laboratory investigation," in 2018 International Carnahan Conference on Security Technology (ICCST), IEEE, 2018, pp. 1–4.

[51] S. Barzanjeh, S. Guha, C. Weedbrook, D. Vitali, J. H. Shapiro, and S. Pirandola, "Microwave quantum illumination," Physical review letters, vol. 114, no. 8, p. 080 503, 2015.

[52] C. S. Chang, M. Simoen, J. Aumentado, et al., "Generating multimode entangled microwaves with a superconducting parametric cavity," Physical Review Applied, vol. 10, no. 4, p. 044 019, 2018.

[53] B. Yurke, L. Corruccini, P. Kaminsky, et al., "Observation of parametric amplification and deamplification in a josephson parametric amplifier," Physical Review A, vol. 39, no. 5, p. 2519, 1989.

[54] N. Messaoudi, C. W. Chang, A. Vadiraj, J. Bourassa, B. Balaji, and C. Wilson, "Quantum-enhanced noise radar," Bulletin of the American Physical Society, vol. 65, 2020.

[55] D. Luong, C. S. Chang, A. Vadiraj, A. Damini, C. M. Wilson, and B. Balaji, "Receiver operating characteristics for a prototype quantum two-mode squeezing radar," IEEE Transactions on Aerospace and Electronic Systems, vol. 56, no. 3, pp. 2041–2060, 2019.

[56] S. Pirandola and S. Lloyd, "Computable bounds for the discrimination of gaussian states," Physical Review A, vol. 78, no. 1, p. 012 331, 2008.

[57] G. Adesso, S. Ragy, and A. R. Lee, "Continuous variable quantum information: Gaussian states and beyond," Open Systems & Information Dynamics, vol. 21, no. 01n02, p. 1 440 001, 2014.

[58] K. M. Audenaert, J. Calsamiglia, R. Munoz-Tapia, et al., "Discriminating states: The quantum chernoff bound," Physical review letters, vol. 98, no. 16, p. 160 501, 2007.

[59] R. Stolen and J. Bjorkholm, "Parametric amplification and frequency conversion in optical fibers," IEEE Journal of Quantum Electronics, vol. 18, no. 7, pp. 1062–1072, 1982.

[60] C. Hong, S. Friberg, and L. Mandel, "Conditions for nonclassical behavior in the light amplifier," JOSA B, vol. 2, no. 3, pp. 494–496, 1985.

[61] V. D'Auria, S. Fornaro, A. Porzio, S. Solimeno, S. Olivares, and M. Paris, "Full characterization of gaussian bipartite entangled states by a single homodyne detector," Physical review letters, vol. 102, no. 2, p. 020 502, 2009.

[62] G. M. D'Ariano, M. G. Paris, and M. F. Sacchi, "Quantum tomography," Advances in Imaging and Electron Physics, vol. 128, pp. 206–309, 2003.

[63] L. Franks, Signal Theory. Prentice-Hall, 1969.

[64] G. H. Golub and C. F. Van Loan, Matrix Computations. 3rd Ed., Johns Hopkins University Press, 1996.

[65] L. Haff, "An identity for the wishart distribution with applications," Journal of Multivariate A vol. 9, no. 4, pp. 531–544, 1979.

[66] M. Kendall and A. Stuart, The Advanced Theory of Statistics. Charles Griffin & Co., Ltd, 1961, vol. I.

[67] M. Arnaudon, F. Barbaresco, and L. Yang, "Riemannian medians and means with applications to radar signal processing," IEEE Journal of Selected Topics in Signal Proce vol. 7, no. 4, pp. 595–604, 2013.

[68] M. Moakher, "A differential geometric approach to the geometric mean of symmetric positive-definite matrices," SIAM Journal on Matrix Analysis and Applications, vol. 26, no. 3, pp. 735–747, 2005.

[69] K. M. Wong, J.-K. Zhang, J. Liang, and H. Jiang, "Mean and median of psd matrices on a riemannian manifold: Application to detection of narrow-band sonar signals," IEEE Transactions on Signal Processing, vol. 65, no. 24, pp. 6536–6550, 2017.

[70] C. W. Helstrom, "Quantum detection and estimation theory," Journal of Statistical Physics, vol. 1, pp. 231–252, 1969.

[71] A. S. Holevo, Probabilistic and statistical aspects of quantum theory. Springer Science & Business Media, 2011, vol. 1.

[72] G. Casella and R. Berger, Statistical inference. vol. 2 duxbury pacific grove, 2002.

[73] S. L. Braunstein and C. M. Caves, "Statistical distance and the geometry of quantum states," Physical Review Letters, vol. 72, no. 22, p. 3439, 1994.

[74] M. G. Paris, "Quantum estimation for quantum technology," International Journal of Quantur vol. 7, no. supp01, pp. 125–137, 2009.

[75] W. P. Grice and I. A. Walmsley, "Spectral information and distinguishability in type-ii down-conversion with a broadband pump," Physical Review A, vol. 56, no. 2, p. 1627, 1997.

[76] I. Ali-Khan, C. J. Broadbent, and J. C. Howell, "Large-alphabet quantum key distribution using energy-time entangled bipartite states," Physical review letters, vol. 98, no. 6, p. 060 503, 2007.

[77] A. S. Holevo, "One-mode quantum gaussian channels: Structure and quantum capacity," Problems of Information Transmission, vol. 43, pp. 1–11, 2007.

[78] J. Ville, "Theorie et application dela notion de signal analysis," Câbles et transmissions, vol. 2, no. 1, pp. 61–74, 1948.

[79] P. M. Woodward, "Radar ambiguity analysis," ROYAL RADAR ESTABLISHMENT MALVERN (UNITED KINGDOM), Tech. Rep., 1967.

[80] P. M. Woodward, Probability and information theory, with applications to radar: internation Elsevier, 2014, vol. 3.

[81] K. Durak, N. Jam, and C. Dindar, "Object tracking and identification by quantum radar," in Quantum Technologies and Quantum Information Science V, SPIE, vol. 11167, 2019, pp. 41–49.

[82] F. A. Beduini, J. A. Zielińska, V. G. Lucivero, Y. A. de Icaza Astiz, and M. W. Mitchell, "Interferometric measurement of the biphoton wave function," Physical review letters, vol. 113, no. 18, p. 183 602, 2014.

[83] U. Schilling, J. von Zanthier, and G. S. Agarwal, "Measuring arbitrary-order coherences: Tomography of single-mode multiphoton polarization-entangled states," Physical Review A, vol. 81, no. 1, p. 013 826, 2010.

[84] A. I. Lvovsky, "Squeezed light," Photonics: Scientific Foundations, Technology and Applicatio vol. 1, pp. 121–163, 2015.

[85] A. A. Clerk, M. H. Devoret, S. M. Girvin, F. Marquardt, and R. J. Schoelkopf, "Introduction to quantum noise, measurement, and amplification," Reviews of Modern Physics vol. 82, no. 2, p. 1155, 2010.

[86] M. Y. Niu, B. C. Sanders, F. N. Wong, and J. H. Shapiro, "Unity-efficiency parametric down-conversion via amplitude amplification," Physical Review Letters, vol. 118, no. 12, p. 123 601, 2017.

[87] M. Y. Niu, I. L. Chuang, and J. H. Shapiro, "Qudit-basis universal quantum computation using χ (2) interactions," Physical review letters, vol. 120, no. 16, p. 160 502, 2018.

Appendix A

Quantum Detection

A.1 Mean and Covariance Matrix

The mean vector $\bar{\mathbf{v}}_c$ can be derived as following

$$\hat{\mathbf{v}}_c = [\hat{\mathbf{a}}_s \ \hat{\mathbf{a}}_i \ \hat{\mathbf{a}}_s^\dagger \ \hat{\mathbf{a}}_i^\dagger] \tag{A.234}$$

The first element in the vector $\bar{v}_c$ is

$$\begin{aligned}
\langle \hat{\mathbf{a}}_s \rangle_{\boldsymbol{\rho}_{\text{si}}} &= \text{tr}(\hat{\mathbf{a}}_s \boldsymbol{\rho}_{\text{si}}) = \text{tr}(\hat{\mathbf{a}}_s \left|\psi\right\rangle_{\text{si}} \langle\psi|) = \text{tr}(\langle\psi| \hat{\mathbf{a}}_s \left|\psi\right\rangle_{\text{si}}) = \langle\psi|\hat{\mathbf{a}}_s|\psi\rangle \\
&= [\sum_{n=0}^{\infty} \sqrt{\frac{N_s^n}{(N_s+1)^{n+1}}} \langle n|_i \langle n|_s] \hat{\mathbf{a}}_s [\sum_{m=0}^{\infty} \sqrt{\frac{N_s^m}{(N_s+1)^{m+1}}} \left|m\right\rangle_s \left|m\right\rangle_i] \\
&= \sum_{n,m}^{\infty} [\frac{N_s^{n+m}}{(N_s+1)^{n+m+2}} \langle n|_i \langle n|_s \sqrt{m} \left|m-1\right\rangle_s \left|m\right\rangle_i]
\end{aligned} \tag{A.235}$$

Due to the orthogonality of number states $\langle n|m\rangle = \delta(n-m)$, the inner product $\langle n|m-1\rangle_s$ can be non-zero if and only if $n = m-1$. However, if $n = m-1$, in the idler system, $\langle n|m\rangle_i = \langle m-1|m\rangle_i$ must be zero. Therefore, the final result will become zero. Other three elements in $\bar{v}_c$ can be derived in the same manner whose results are also zero.

The derivation of the covariance matrix $\mathbf{\Gamma}$ in Eq.4.63 is included.

$$\hat{\mathbf{v}}_c \cdot \hat{\mathbf{v}}_c^\dagger = \begin{bmatrix} \hat{\mathbf{a}}_s \\ \hat{\mathbf{a}}_i \\ \hat{\mathbf{a}}_s^\dagger \\ \hat{\mathbf{a}}_i^\dagger \end{bmatrix} \cdot \begin{bmatrix} \hat{\mathbf{a}}_s^\dagger & \hat{\mathbf{a}}_i^\dagger & \hat{\mathbf{a}}_s & \hat{\mathbf{a}}_i \end{bmatrix} \tag{A.236}$$

The 11th element is $\langle \hat{\mathbf{a}}_s \hat{\mathbf{a}}_s^\dagger \rangle = \langle \hat{\mathbf{a}}_s^\dagger \hat{\mathbf{a}}_s + \hat{\mathbf{I}} \rangle = \langle \hat{\mathbf{a}}_s^\dagger \hat{\mathbf{a}}_s \rangle + 1 = \langle \hat{\mathbf{n}}_s \rangle + 1 = N_s + 1$. The 22th element is $\langle \hat{\mathbf{a}}_i \hat{\mathbf{a}}_i^\dagger \rangle = N_s + 1$. The 33th element is $\langle \hat{\mathbf{a}}_s^\dagger \hat{\mathbf{a}}_s \rangle = N_s$ and 44th element is $\langle \hat{\mathbf{a}}_i^\dagger \hat{\mathbf{a}}_i \rangle = N_s$.

The 12th element $\langle \hat{\mathbf{a}}_s \hat{\mathbf{a}}_i^\dagger \rangle$ is

$$\begin{aligned}
\langle \hat{\mathbf{a}}_s \hat{\mathbf{a}}_i^\dagger \rangle &= \mathrm{tr}(\boldsymbol{\rho}_{si} \hat{\mathbf{a}}_s \hat{\mathbf{a}}_i^\dagger) = \mathrm{tr}(|\psi\rangle_{\mathrm{si}} \langle\psi|_{\mathrm{si}} \hat{\mathbf{a}}_s \hat{\mathbf{a}}_i^\dagger) = \mathrm{tr}(\langle\psi|_{\mathrm{si}} \hat{\mathbf{a}}_s \hat{\mathbf{a}}_i^\dagger |\psi\rangle_{\mathrm{si}}) = \langle\psi|_{\mathrm{si}} \hat{\mathbf{a}}_s \hat{\mathbf{a}}_i^\dagger |\psi\rangle_{\mathrm{si}} \\
&= [\sum_{n=0}^{\infty} \sqrt{\frac{N_s^n}{(N_s+1)^{n+1}}} \langle n|_i \langle n|_s] \hat{\mathbf{a}}_s \hat{\mathbf{a}}_i^\dagger [\sum_{m=0}^{\infty} \sqrt{\frac{N_s^m}{(N_s+1)^{m+1}}} |m\rangle_s |m\rangle_i] \\
&= \sum_{n=0}^{\infty} \sum_{m=0}^{\infty} \sqrt{\frac{N_s^{n+m}}{(N_s+1)^{n+m+2}}} \langle n|_i \langle n|_s [\hat{\mathbf{a}}_s \hat{\mathbf{a}}_i^\dagger |m\rangle_s |m\rangle_i] \\
&= \sum_{n=0}^{\infty} \sum_{m=0}^{\infty} \sqrt{\frac{N_s^{n+m}}{(N_s+1)^{n+m+2}}} \langle n|_i \langle n|_s \sqrt{m(m+1)} |m-1\rangle_s |m+1\rangle_i
\end{aligned} \tag{A.237}$$

Given that $\langle n|m\rangle = \delta(n-m)$, the inner product $\langle n|m-1\rangle_s$ can be non-zero if and

only if $m-1=n$. However, the term $\langle n|m+1\rangle_i = \langle n|n+2\rangle = 0$. Therefore, this term becomes 0.

The 13th element is

$$\begin{aligned}\langle \hat{\mathbf{a}}_s\hat{\mathbf{a}}_s\rangle &= \mathrm{tr}(\boldsymbol{\rho}_{\mathrm{si}}\hat{\mathbf{a}}_s\hat{\mathbf{a}}_s) = \mathrm{tr}(|\psi\rangle_{\mathrm{si}}\langle\psi|_{\mathrm{si}}\hat{\mathbf{a}}_s\hat{\mathbf{a}}_s) = \mathrm{tr}(\langle\psi|_{\mathrm{si}}\hat{\mathbf{a}}_s\hat{\mathbf{a}}_i^{\dagger}|\psi\rangle_{\mathrm{si}}) = \langle\psi|_{\mathrm{si}}\hat{\mathbf{a}}_s\hat{\mathbf{a}}_s|\psi\rangle_{\mathrm{si}} \\ &= [\sum_{n=0}^{\infty}\sqrt{\frac{N_s^n}{(N_s+1)^{n+1}}}\langle n|_i\langle n|_s]\hat{\mathbf{a}}_s\hat{\mathbf{a}}_s[\sum_{m=0}^{\infty}\sqrt{\frac{N_s^m}{(N_s+1)^{m+1}}}|m\rangle_s|m\rangle_i] \\ &= \sum_{n=0}^{\infty}\sum_{m=0}^{\infty}\sqrt{\frac{N_s^{n+m}}{(N_s+1)^{n+m+2}}}\langle n|_i\langle n|_s[\hat{\mathbf{a}}_s\hat{\mathbf{a}}_s|m\rangle_s|m\rangle_i] \\ &= \sum_{n=0}^{\infty}\sum_{m=0}^{\infty}\sqrt{\frac{N_s^{n+m}}{(N_s+1)^{n+m+2}}}\langle n|_i\langle n|_s\sqrt{m(m-1)}|m-2\rangle_s|m\rangle_i\end{aligned} \tag{A.238}$$

In order to become non-zero, $m-2=n$. However, $\langle n|m\rangle_i = \langle n|n+2\rangle_i = 0$. Therefore, this term becomes 0.

The 14th element is

$$\begin{aligned}\langle \hat{\mathbf{a}}_s\hat{\mathbf{a}}_i\rangle &= \mathrm{tr}(\boldsymbol{\rho}_{\mathrm{si}}\hat{\mathbf{a}}_s\hat{\mathbf{a}}_i) = \mathrm{tr}(|\psi\rangle_{\mathrm{si}}\langle\psi|_{\mathrm{si}}\hat{\mathbf{a}}_s\hat{\mathbf{a}}_i) = \mathrm{tr}(\langle\psi|_{\mathrm{si}}\hat{\mathbf{a}}_s\hat{\mathbf{a}}_i|\psi\rangle_{\mathrm{si}}) = \langle\psi|_{\mathrm{si}}\hat{\mathbf{a}}_s\hat{\mathbf{a}}_i|\psi\rangle_{\mathrm{si}} \\ &= [\sum_{n=0}^{\infty}\sqrt{\frac{N_s^n}{(N_s+1)^{n+1}}}\langle n|_i\langle n|_s]\hat{\mathbf{a}}_s\hat{\mathbf{a}}_i[\sum_{m=0}^{\infty}\sqrt{\frac{N_s^m}{(N_s+1)^{m+1}}}|m\rangle_s|m\rangle_i] \\ &= \sum_{n=0}^{\infty}\sum_{m=0}^{\infty}\sqrt{\frac{N_s^{n+m}}{(N_s+1)^{n+m+2}}}\langle n|_i\langle n|_s[\hat{\mathbf{a}}_s\hat{\mathbf{a}}_i|m\rangle_s|m\rangle_i] \\ &= \sum_{n=0}^{\infty}\sum_{m=0}^{\infty}\sqrt{\frac{N_s^{n+m}}{(N_s+1)^{n+m+2}}}\langle n|_i\langle n|_s m|m-1\rangle_s|m-1\rangle_i\end{aligned} \tag{A.239}$$

For non-zero inner products, $m-1=n$ or $m=n+1$. Then, the result becomes

$$\langle \hat{\mathbf{a}}_s\hat{\mathbf{a}}_i\rangle = \sum_{n=0}^{\infty}\sqrt{\frac{N_s^{2n+1}}{(N_s+1)^{2n+3}}}(n+1) = \sqrt{N_s(N_s+1)} \tag{A.240}$$

The 23th element is $\langle \hat{\mathbf{a}}_i \hat{\mathbf{a}}_s \rangle$ which gives the same result as $\langle \hat{\mathbf{a}}_s \hat{\mathbf{a}}_i \rangle$ because these two operators are commute $[\hat{\mathbf{a}}_s, \hat{\mathbf{a}}_i] = \mathbf{0}$.

The 24th element is $\langle \hat{\mathbf{a}}_i \hat{\mathbf{a}}_i \rangle$, which gives the same result as 13th element, $\langle \hat{\mathbf{a}}_s \hat{\mathbf{a}}_s \rangle$ because the signal and idler systems are identical in the SPDC output.

The 34th element is $\langle \hat{\mathbf{a}}_s^\dagger \hat{\mathbf{a}}_i \rangle$ which gives the same result as the 12th element, $\langle \hat{\mathbf{a}}_s \hat{\mathbf{a}}_i^\dagger \rangle$ because the signal and idler systems are identical in the SPDC output.

Moreover, the covariance matrix is symmetric; hence, the covariance matrix is

$$\mathbf{\Gamma} = \begin{bmatrix} N_s + 1 & 0 & 0 & \sqrt{N_s(N_s+1)} \\ 0 & N_s + 1 & \sqrt{N_s(N_s+1)} & 0 \\ 0 & \sqrt{N_s(N_s+1)} & N_s & 0 \\ \sqrt{N_s(N_s+1)} & 0 & 0 & N_s \end{bmatrix} \tag{A.241}$$

A.2 Theorem on Two Matrices A and B

Let $\mathbf{P}$ be the projector on the range of $(\mathbf{a}-\mathbf{b})_+$ where $(\mathbf{a}-\mathbf{b})_+ = \frac{\mathbf{1}}{\mathbf{2}}[|\mathbf{a}-\mathbf{b}|+(\mathbf{a}-\mathbf{b})]$. Then, the lemma in [58] has been developed

Lemma A.2.1 *Let* $\mathbf{a}, \mathbf{b} \geq \mathbf{0}$ *and* $0 \leq t \leq 1$ *and* $\boldsymbol{P}$ *be the projector on the range of* $(\boldsymbol{a} - \boldsymbol{b})_+$. *Then,*

$$\mathrm{tr}(\boldsymbol{P}\boldsymbol{b}(\boldsymbol{a}^{\boldsymbol{t}} - \boldsymbol{b}^{\boldsymbol{t}})) \geq 0 \tag{A.242}$$

Then let $\boldsymbol{a} = \boldsymbol{A}^{1-s}$ and $\boldsymbol{b} = \boldsymbol{B}^{1-s}$ and $t = s/(1-s)$, which gives

$$\mathrm{tr}[\boldsymbol{P}\boldsymbol{B}^{1-s}(\boldsymbol{A}^s - \boldsymbol{B}^s)] \geq 0 \tag{A.243}$$

Substracting both sides from $\mathrm{tr}[\boldsymbol{P}(\boldsymbol{A}-\boldsymbol{B})]$ gives

$$\mathrm{tr}[\boldsymbol{A}^s\boldsymbol{P}(\boldsymbol{B}^{1-s} - \boldsymbol{A}^{1-s})] \geq -\mathrm{tr}[\boldsymbol{P}(\boldsymbol{A}-\boldsymbol{B})] \tag{A.244}$$

Given that $\boldsymbol{P}$ is the projector onto $(\boldsymbol{a}-\boldsymbol{b})_+ = (\boldsymbol{A}^{1-s} - \boldsymbol{B}^{1-s})_+$. Then, the LHS of the inequality becomes

$$\mathrm{tr}[\boldsymbol{A}^s(\boldsymbol{A}^{1-s} - \boldsymbol{B}^{1-s})_+] \leq \mathrm{tr}[\boldsymbol{P}(\boldsymbol{A}-\boldsymbol{B})] \tag{A.245}$$

Because $\mathbf{a} = \mathbf{A}^{1-s} \geq 0$, then $\mathbf{A}^s$ is positive semidefinite $\mathbf{A}^s \geq 0$.Then the LHS is lower bounded by

$$\mathrm{tr}[\boldsymbol{A}^s(\boldsymbol{A}^{1-s} - \boldsymbol{B}^{1-s})] \leq \mathrm{tr}[\boldsymbol{A}^s(\boldsymbol{B}^{1-s} - \boldsymbol{B}^{1-s})_+] \tag{A.246}$$

This lower bound is $\mathrm{tr}[\boldsymbol{A} - \boldsymbol{A}^s\boldsymbol{B}^{1-s}]$. Moreover, because for any self-joint $\mathbf{H}$, $\mathrm{tr}(\mathbf{H}_+)$ is the maximum of $\mathrm{tr}(\mathbf{QH})$ over all self-joint projectors $\mathbf{Q}$. Then, the LHS of the above inequality is upper bounded by $\mathrm{tr}[(\mathbf{A}-\mathbf{B})_+]$. Then

$$\mathrm{tr}[\boldsymbol{A} - \boldsymbol{A}^s\boldsymbol{B}^{1-s}] \leq \mathrm{tr}[(\mathbf{A}-\mathbf{B})_+] = \frac{\mathbf{1}}{\mathbf{2}}\mathrm{tr}[(\mathbf{A}-\mathbf{B}) + |\mathbf{A}-\mathbf{B}|] \tag{A.247}$$

Subtracting both sides by $\mathrm{tr}(\mathbf{A})$ and taking the negative gives

$$\frac{1}{2}\mathrm{tr}[\mathbf{A}+\mathbf{B}-|\mathbf{A}-\mathbf{B}|] \leq \mathrm{tr}(\boldsymbol{A}^{\mathbf{s}}\boldsymbol{B}^{\mathbf{1-s}}) \tag{A.248}$$

Then, with $\mathbf{A}=\pi_1\boldsymbol{\rho}_1, \mathbf{B}=\pi_0\boldsymbol{\rho}_0$, this inequality becomes

$$\frac{1}{2}\mathrm{tr}[\pi_{\mathbf{1}}\boldsymbol{\rho}_{\mathbf{1}}+\pi_{\mathbf{0}}\boldsymbol{\rho}_{\mathbf{0}}-|\pi_{\mathbf{1}}\boldsymbol{\rho}_{\mathbf{1}}-\pi_{\mathbf{0}}\boldsymbol{\rho}_{\mathbf{0}}|] \leq \mathrm{tr}[(\pi_{\mathbf{1}}\boldsymbol{\rho}_{\mathbf{1}})^{\mathbf{s}}(\pi_{\mathbf{0}}\boldsymbol{\rho}_{\mathbf{0}})^{\mathbf{1-s}}] \tag{A.249}$$

The minimum probability of error is upper bounded by

$$\begin{aligned} P_{\mathrm{e,min}} &\leq \inf_{0\leq s\leq 1} \mathrm{tr}((\pi_1\boldsymbol{\rho}_1)^s(\pi_0\boldsymbol{\rho}_0)^{1-s}) \\ &= \inf_{0\leq s\leq 1} \pi_1^s\pi_0^{1-s}\mathrm{tr}(\boldsymbol{\rho}_1^s\boldsymbol{\rho}_0^{1-s}) \\ &\leq \frac{1}{2}\inf_{0\leq s\leq 1} \mathrm{tr}(\boldsymbol{\rho}_1^s\boldsymbol{\rho}_0^{1-s}) \end{aligned} \tag{A.250}$$

The last inequality comes from that $\pi_1^s\pi_0^{1-s}=\pi_1^s(1-\pi_1)^{1-s}$ is maximum

$$\frac{d}{d\pi_1}\pi_1^s(1-\pi_1)^{1-s} = s\pi_1^{s-1}(1-\pi_1)^{1-s}-(1-s)(1-\pi_1)^{-s}\pi_1^s = 0 \tag{A.251}$$

This gives $\pi_1=\frac{1}{2}$ and then $\pi_0=\frac{1}{2}$ correspondingly.

In the M-mode system state, $\boldsymbol{\rho}_0$ is replaced by $\boldsymbol{\rho}_0^{\otimes M}$ and $\boldsymbol{\rho}_1$ is replaced by $\boldsymbol{\rho}_1^{\otimes M}$. The

error bound becomes

$$\begin{aligned} P_{\text{e,min}} &\leq \frac{1}{2} \inf_{0\leq s\leq 1} \text{tr}[(\boldsymbol{\rho}_1^{\otimes M})^s (\boldsymbol{\rho}_0^{\otimes M})^{1-s}] \\ &= \frac{1}{2} \inf_{0\leq s\leq 1} \text{tr}[(\boldsymbol{\rho}_1^{s})^{\otimes M} (\boldsymbol{\rho}_0^{1-s})^{\otimes M}] \\ &= \frac{1}{2} \inf_{0\leq s\leq 1} \text{tr}[(\boldsymbol{\rho}_1^{s}\boldsymbol{\rho}_0^{1-s})^{\otimes M}] \\ &= \frac{1}{2} \inf_{0\leq s\leq 1} \text{tr}(\boldsymbol{\rho}_1^{s}\boldsymbol{\rho}_0^{1-s}) \cdot \text{tr}(\boldsymbol{\rho}_1^{s}\boldsymbol{\rho}_0^{1-s}) \cdots \text{tr}(\boldsymbol{\rho}_1^{s}\boldsymbol{\rho}_0^{1-s}) \\ &= \frac{1}{2} \inf_{0\leq s\leq 1} \text{tr}(\boldsymbol{\rho}_1^{s}\boldsymbol{\rho}_0^{1-s})^M \end{aligned} \tag{A.252}$$

The second equation becomes from the property of the Kronecker product that $(\mathbf{A}^{\otimes M})^N = (\boldsymbol{A} \otimes \boldsymbol{A} \otimes \cdots \otimes \boldsymbol{A})^N = \boldsymbol{A}^N \otimes \boldsymbol{A}^N \otimes \cdots \otimes \boldsymbol{A}^N = (\boldsymbol{A}^N)^{\otimes M}$. The third equation becomes from the property of the Kronecker product that $\mathbf{A}^{\otimes M}\boldsymbol{B}^{\otimes M} = (\boldsymbol{A}\otimes\boldsymbol{A}\otimes\cdots\otimes\boldsymbol{A})(\boldsymbol{B}\otimes\boldsymbol{B}\otimes\cdots\otimes\boldsymbol{B}) = (\boldsymbol{AB})\otimes(\boldsymbol{AB})\otimes\cdots\otimes(\boldsymbol{AB}) = (\boldsymbol{AB})^{\otimes M}$. The fourth equation becomes from the property of the Kronecker product that $\text{tr}(\boldsymbol{A}^{\otimes M}) = \text{tr}(\boldsymbol{A} \otimes \boldsymbol{A} \otimes \cdots \otimes \boldsymbol{A}) = \text{tr}(\boldsymbol{A}) \cdot \text{tr}(\boldsymbol{A}) \cdots \text{tr}(\boldsymbol{A}) = \text{tr}(\boldsymbol{A})^M$.

A.3 Theorem on Quantum Chernoff Bound

As given in the Eq.4.79,the quantum error exponent is given by

$$Q_s = \text{tr}(\boldsymbol{\rho}_0^{s}\boldsymbol{\rho}_1^{1-s}) \tag{A.253}$$

A n-mode Gaussian state with the density operator $\boldsymbol{\rho}$ can be transformed to the tensor product of n independent thermal states as shown in Eq.4.72

$$\boldsymbol{\rho} = \hat{\mathbf{U}}[\bigotimes_{k=1}^{n} \boldsymbol{\rho}_{\mathrm{th}}(v_k)]\hat{\mathbf{U}}^{\dagger} \tag{A.254}$$

where $\hat{\mathbf{U}}$ is the unitary operator and $\boldsymbol{\rho}_{\mathrm{th}}$ is the density operator of the thermal states and v_k is the symplectic eigenvalue of the covariance matrix of $\boldsymbol{\rho}$. Then, the density operator to the power of s can be obtained

$$\boldsymbol{\rho}^s = \hat{\mathbf{U}}[\bigotimes_{k=1}^{n} (\boldsymbol{\rho}_{\mathrm{th}}(v_k))^s]\hat{\mathbf{U}}^{\dagger} \tag{A.255}$$

given that $\hat{\mathbf{U}}^{\dagger}\hat{\mathbf{U}} = \hat{\mathbf{I}}$.

As defined in Eq.4.73,

$$\boldsymbol{\rho}_{\mathrm{th}}(v_k) = \frac{2}{v_k + 1} \sum_{j=0}^{\infty} \left(\frac{v_k - 1}{v_k + 1}\right)^j |j\rangle_k \langle j|$$

Let $\eta_k = \frac{v_k - 1}{v_k + 1}$ and then,

$$\boldsymbol{\rho}_{\mathrm{th}}(\eta_k) = (1 - \eta_k) \sum_{j=0}^{\infty} \eta_k^j |j\rangle_k \langle j| \tag{A.256}$$

And

$$\boldsymbol{\rho}_{\mathrm{th}}^s(\eta_k) = (1 - \eta_k)^s \sum_{j=0}^{\infty} (\eta_k^s)^j |j\rangle_k \langle j| = \frac{(1 - \eta_k)^s}{1 - \eta_k^s} \boldsymbol{\rho}_{\mathrm{th}}(\eta_k^s) \tag{A.257}$$

Here the term $\frac{(1-\eta_k)^s}{1-\eta_k^s}$ can be written as by substituting $\eta_k = \frac{v_k-1}{v_k+1}$

$$\frac{(1-\eta_k)^s}{1-\eta_k^s} = \frac{2^s}{(v_k+1)^s-(v_k-1)^s} \triangleq G_s(v_k) \tag{A.258}$$

Moreover, due to the relationship between η_k and v_k, the new symplectic eigenvalue $\tilde{v}_k$ corresponding to η_k^s is

$$\tilde{v}_k = \frac{1+\eta_k^s}{1-\eta_k^s} = \frac{(v_k+1)^s+(v_k-1)^s}{(v_k+1)^s-(v_k-1)^s} \triangleq F_s(v_k) \tag{A.259}$$

Then, the density operator to the power of s can be written as

$$\boldsymbol{\rho}^s = \mathrm{tr}(\boldsymbol{\rho}^s)\boldsymbol{\rho}(s) \tag{A.260}$$

where $\mathrm{tr}(\boldsymbol{\rho}^s) = \prod_{k=1}^n G_s(v_k)$. Since v_k are the symplectic eigenvalues of the system state $\boldsymbol{\rho}$, therefore, so are $F_s(v_k)$. This is the lemma developed in [56].

Therefore, the quantum error exponent becomes

$$\begin{aligned} Q_s &= \mathrm{tr}(\boldsymbol{\rho}_0^s)\mathrm{tr}(\boldsymbol{\rho}_1^{1-s})\mathrm{tr}(\boldsymbol{\rho}_0(s)\boldsymbol{\rho}_1(1-s)) \\ &= \prod_{k=1}^n G_s(\alpha_k)G_{1-s}(\beta_k)\mathrm{tr}(\boldsymbol{\rho}_0(s)\boldsymbol{\rho}_1(1-s)) \end{aligned} \tag{A.261}$$

where α_k and β_k are the symplectic eigenvalues of $\boldsymbol{\Gamma}_0^p$ and $\boldsymbol{\Gamma}_1^p$ respectively.

The term $\mathrm{tr}(\boldsymbol{\rho}_0(s)\boldsymbol{\rho}_1(1-s))$ is given as the

$$\mathrm{tr}(\boldsymbol{\rho}_0(s)\boldsymbol{\rho}_1(1-s)) = \frac{1}{\pi^n}\int \chi_{0,s}(\boldsymbol{\xi})\chi_{1,1-s}(-\boldsymbol{\xi})d^n\boldsymbol{\xi} \tag{A.262}$$

where $\chi(\boldsymbol{\xi})$ is the characteristic function of the density operator.

$$\chi_{0,s} = \exp[-\frac{1}{2}\boldsymbol{\xi}^T\mathbf{V}_0(s)\boldsymbol{\xi} + i\bar{\mathbf{y}}_0^T\boldsymbol{\xi}] \tag{A.263a}$$

$$\chi_{1,1-s} = \exp[-\frac{1}{2}\boldsymbol{\xi}^T\mathbf{V}_1(1-s)\boldsymbol{\xi} + i\bar{\mathbf{y}}_1^T\boldsymbol{\xi}] \tag{A.263b}$$

The covariance matrix corresponding to $\boldsymbol{\rho}_0(s)$ and $\boldsymbol{\rho}_1(1-s)$ are

$$\mathbf{V}_0(s) = \mathbf{S}_0[\bigoplus_{k=1}^{n} F_s(\alpha_k)\boldsymbol{I}_2]\mathbf{S}_0^T \tag{A.264a}$$

$$\mathbf{V}_1(1-s) = \mathbf{S}_1[\bigoplus_{k=1}^{n} F_{1-s}(\beta_k)\boldsymbol{I}_2]\mathbf{S}_1^T \tag{A.264b}$$

Then, for the system states $\boldsymbol{\rho}_0(s)$ and $\boldsymbol{\rho}_1(1-s)$, they have the mean $\bar{\mathbf{y}}_0, \bar{\mathbf{y}}_1$ and covariances in the Eqs.A.264 and then $\mathrm{tr}(\boldsymbol{\rho}_0(s)\boldsymbol{\rho}_1(1-s))$ is given by

$$\mathrm{tr}(\boldsymbol{\rho}_0(s)\boldsymbol{\rho}_1(1-s)) = 2^n \frac{\exp\Big[-\frac{1}{2}(\bar{\mathbf{y}}_0 - \bar{\mathbf{y}}_1)^T(\mathbf{V}_0(s) + \mathbf{V}_1(1-s))^{-1}(\bar{\mathbf{y}}_0 - \bar{\mathbf{y}}_1))\Big]}{\sqrt{\det(\mathbf{V}_0(s) + \mathbf{V}_1(1-s))}} \tag{A.265}$$

Then, the error exponent Q_s is given as

$$\begin{aligned} Q_s &= \frac{2^n \prod_{k=1}^{n} G_s(\alpha_k)G_{1-s}(\beta_k)}{\sqrt{\det(\mathbf{V}_0(s) + \mathbf{V}_1(1-s))}} \cdot \exp\Big[-\frac{1}{2}(\bar{\mathbf{y}}_0 - \bar{\mathbf{y}}_1)^T(\mathbf{V}_0(s) + \mathbf{V}_1(1-s))^{-1}(\bar{\mathbf{y}}_0 - \bar{\mathbf{y}}_1))\Big] \\ &\triangleq \bar{Q}_s \cdot \exp\Big[-\frac{1}{2}(\bar{\mathbf{y}}_0 - \bar{\mathbf{y}}_1)^T(\mathbf{V}_0(s) + \mathbf{V}_1(1-s))^{-1}(\bar{\mathbf{y}}_0 - \bar{\mathbf{y}}_1))\Big] \end{aligned} \tag{A.266}$$

Appendix B

Quantum Estimation

B.1 Derivation of Eqs.5.188 and 5.189

B.1.1 Eq.5.188

For $\hat{\mathbf{L}}_{\bar{t}_r}$,

$$\hat{\mathbf{L}}_{\bar{t}_r} = 2 \sum_{n,m;p_n+p_m\neq 0} \frac{\langle f_m|\partial_{\bar{t}_r}\boldsymbol{\rho}_{\rm ri}|f_n\rangle}{p_n+p_m} |f_m\rangle \langle f_n| \tag{B.267}$$

The derivative of the system operator with respect to $\bar{t}_r$ is

$$\partial_{\bar{t}_r}\boldsymbol{\rho}_{\rm ri} = (\partial_{\bar{t}_r}|\psi_{\rm ri}\rangle)\langle\psi_{\rm ri}| + |\psi_{\rm ri}\rangle(\partial_{\bar{t}_r}\langle\psi_{\rm ri}|) \tag{B.268}$$

The term

$$\langle f_1|\partial_{\bar{t}_r}\boldsymbol{\rho}_{\rm ri}|f_1\rangle = \langle\psi_{\rm ri}|[(\partial_{\bar{t}_r}|\psi_{\rm ri}\rangle)\langle\psi_{\rm ri}| + |\psi_{\rm ri}\rangle(\partial_{\bar{t}_r}\langle\psi_{\rm ri}|)]|\psi_{\rm ri}\rangle = \langle\psi_{\rm ri}|\partial_{\bar{t}_r}\psi_{\rm ri}\rangle + \langle\partial_{\bar{t}_r}\psi_{\rm ri}|\psi_{\rm ri}\rangle \tag{B.269}$$

$$\begin{aligned}\langle\psi_{\rm ri}|\partial_{\bar{t}_r}\psi_{\rm ri}\rangle &= \left[\int\int \psi_{\rm ri}(t_r,t_i)^*\langle t_r|_r\langle t_i|_i\, dt_r dt_i\right] \\ &\cdot\left[\int\int [i\bar{\omega}_r + 2\sigma_r^2(t_r'-\bar{t}_r) - 2\kappa\sigma_r\sigma_i(t_i'-\bar{t}_i)]\psi_{\rm ri}(t_r',t_i')\,|t_r'\rangle_r\,|t_i'\rangle\, dt_r' dt_i'\right] \\ &= \int\int [i\bar{\omega}_r + 2\sigma_r^2(t_r-\bar{t}_r) - 2\kappa\sigma_r\sigma_i(t_i-\bar{t}_i)]\psi_{\rm ri}(t_r,t_i)^*\psi_{\rm ri}(t_r,t_i)dt_r dt_i \\ &= \int\int [i\bar{\omega}_r + 2\sigma_r^2(t_r-\bar{t}_r) - 2\kappa\sigma_r\sigma_i(t_i-\bar{t}_i)]|\psi_{\rm ri}(t_r,t_i)|^2 dt_r dt_i\end{aligned} \tag{B.270}$$

where $*$ here denotes the complex conjugate. Moreover,

$$\begin{aligned}\langle\psi_{\rm ri}|\partial_{\bar{t}_r}\psi_{\rm ri}\rangle &= \left[\int\int [-i\bar{\omega}_r + 2\sigma_r^2(t_r'-\bar{t}_r) - 2\kappa\sigma_r\sigma_i(t_i'-\bar{t}_i)]\psi_{\rm ri}(t_r,t_i)^*\langle t_r|_r\langle t_i|_i\, dt_r dt_i\right] \\ &\cdot\left[\int\int \psi_{\rm ri}(t_r',t_i')\,|t_r'\rangle_r\,|t_i'\rangle\, dt_r' dt_i'\right] \\ &= \int\int [-i\bar{\omega}_r + 2\sigma_r^2(t_r-\bar{t}_r) - 2\kappa\sigma_r\sigma_i(t_i-\bar{t}_i)]|\psi_{\rm ri}(t_r,t_i)|^2 dt_r dt_i\end{aligned} \tag{B.271}$$

The sum of these two equations becomes

$$\int\int [4\sigma_r^2(t_r-\bar{t}_r) - 4\kappa\sigma_r\sigma_i(t_i-\bar{t}_i)]|\psi_{\rm ri}(t_r,t_i)|^2 dt_r dt_i \tag{B.272}$$

which consists of two parts and the first one is given as

$$\begin{aligned}
&\int\int 2\sigma_s^2(t_r-\bar{t}_r)\exp\Big[-2(t_r-\bar{t}_r)^2\sigma_r^2-2(t_i-\bar{t}_i)^2\sigma_i^2+4\kappa(t_r-\bar{t}_r)(t_i-\bar{t}_i)\sigma_r\sigma_i\Big]dt_r dt_i\\
&=\int\int 2\sigma_r^2 t_r\exp\Big[-2t_r^2\sigma_r^2-2t_i^2\sigma_i^2+4\kappa t_r t_i\sigma_r\sigma_i\Big]dt_r dt_i\\
&=\int\int 2\sigma_r^2 t_r\exp\Big[-2(t_i\sigma_i-\kappa t_r\sigma_r)^2-2(1-\kappa^2)\sigma_r^2 t_r^2\Big]dt_r dt_i\\
&=0
\end{aligned} \tag{B.273}$$

The second line is obtained by replacing $t_i-\bar{t}_i$ with t_i and $t_r-\bar{t}_r$ with t_r. The final result is zero because $t\exp(-at^2)$ is an odd function and the integration of the odd function from $(-\infty)$ to $(+\infty)$ gives 0. Similarly, the term associated with $2\kappa\sigma_r\sigma_i(t_i-\bar{t}_i)$ is also 0. Therefore,

$$\langle f_1|\partial_{\bar{t}_r}\boldsymbol{\rho}_{\mathrm{ri}}|f_1\rangle=0 \tag{B.274}$$

The second term in $\hat{\mathbf{L}}_{\bar{t}_r}$ is

$$\langle f_2|\partial_{\bar{t}_r}\boldsymbol{\rho}_{\mathrm{ri}}|f_1\rangle=\langle f_2|[(\partial_{\bar{t}_r}|\psi_{\mathrm{ri}}\rangle)\langle\psi_{\mathrm{ri}}|+|\psi_{\mathrm{ri}}\rangle(\partial_{\bar{t}_r}\langle\psi_{\mathrm{ri}}|)]|\psi_{\mathrm{ri}}\rangle=\langle f_2|\partial_{\bar{t}_r}\psi_{\mathrm{ri}}\rangle+\langle f_2|\psi_{\mathrm{ri}}\rangle\langle\partial_{\bar{t}_r}\psi_{\mathrm{ri}}|\psi_{\mathrm{ri}}\rangle \tag{B.275}$$

The term $\langle f_2|\psi_{\text{ri}}\rangle$ is

$$\begin{aligned}\langle f_2|\psi_{\text{ri}}\rangle &= \int\int \sqrt{2(1-\kappa)}[\sigma_r(t_r-\bar{t}_r)+\sigma_i(t_i-\bar{t}_i)]\psi^*_{ri}(t_r,t_i)\,\langle t_r|_r\,\langle t_i|\,dt_r dt_i \\ &\cdot \int\int \psi_{\text{ri}}(t'_r,t'_i)\,|t'_r\rangle_r\,|t'_i\rangle_i\,dt'_r dt'_i \\ &= \int\int \sqrt{2(1-\kappa)}[\sigma_r(t_r-\bar{t}_r)+\sigma_i(t_i-\bar{t}_i)]|\psi_{\text{ri}}(t_r,t_i)|^2 dt_r dt_i \\ &= 0\end{aligned} \tag{B.276}$$

The term $\langle f_2|\partial_{\bar{t}_r}\psi_{\text{ri}}\rangle$ is

$$\begin{aligned}&\langle f_2|\partial_{\bar{t}_r}\psi_{\text{ri}}\rangle = \int\int \sqrt{2(1-\kappa)}[\sigma_r(t_r-\bar{t}_r)+\sigma_i(t_i-\bar{t}_i)]\psi_{ri}(t_r,t_i)\,\langle t_r|_r\,\langle t_i|\,dt_r dt_i \\ &\cdot \int\int [i\bar{\omega}_r + 2\sigma_r^2(t'_r-\bar{t}_r) - 2\kappa\sigma_r\sigma_i(t'_i-\bar{t}_i)]\psi_{\text{ri}}(t'_r,t'_i)\,|t'_r\rangle_r\,|t'_i\rangle\,dt'_r dt'_i \\ &= \int\int \sqrt{2(1-\kappa)}[\sigma_r(t_r-\bar{t}_r)+\sigma_i(t_i-\bar{t}_i)][i\bar{\omega}_r + 2\sigma_r^2(t_r-\bar{t}_r) - 2\kappa\sigma_r\sigma_i(t_i-\bar{t}_i)]|\psi_{\text{ri}}(t_r,t_i)|^2 dt_r dt_i\end{aligned} \tag{B.277}$$

The non-zero terms are

$$\begin{aligned}\langle f_2|\partial_{\bar{t}_r}\psi_{\text{ri}}\rangle &= \int\int \sqrt{2(1-\kappa)}[2\sigma_r^3(t_r-\bar{t}_r)^2 + 2\sigma_r^2\sigma_i(1-\kappa)(t_r-\bar{t}_r)(t_i\bar{t}_i) - 2\kappa\sigma_r\sigma_i^2(t_i-\bar{t}_i)^2]|\psi_{\text{ri}}(t_r,t_i)| \\ &= \sigma_r\sqrt{2(1-\kappa)}\end{aligned} \tag{B.278}$$

Hence,

$$\langle f_2|\partial_{\bar{t}_r}\boldsymbol{\rho}_{\text{ri}}|f_1\rangle = \sigma_r\sqrt{2(1-\kappa)} \tag{B.279}$$

Applying the similar steps, other three elements can be obtained

$$\langle f_3|\partial_{\bar{t}_r}\boldsymbol{\rho}_{\rm ri}|f_1\rangle = \sigma_r\sqrt{2(1+\kappa)} \tag{B.280a}$$

$$\langle f_1|\partial_{\bar{t}_r}\boldsymbol{\rho}_{\rm ri}|f_2\rangle = \sigma_r\sqrt{2(1-\kappa)} \tag{B.280b}$$

$$\langle f_1|\partial_{\bar{t}_r}\boldsymbol{\rho}_{\rm ri}|f_3\rangle = \sigma_r\sqrt{2(1+\kappa)} \tag{B.280c}$$

$$\tag{B.280d}$$

B.1.2 Eq.5.189

$$\begin{aligned}\hat{\mathbf{L}}_{\bar{\omega}_r} = 2\Bigg[&\frac{\langle f_1|\partial_{\bar{\omega}_r}\boldsymbol{\rho}_{\rm ri}|f_1\rangle}{2}|f_1\rangle\langle f_1| + \langle f_2|\partial_{\bar{\omega}_r}\boldsymbol{\rho}_{\rm ri}|f_1\rangle|f_2\rangle\langle f_1| + \langle f_3|\partial_{\bar{\omega}_r}\boldsymbol{\rho}_{\rm ri}|f_1\rangle|f_3\rangle\langle f_1| \\ &+ \langle f_1|\partial_{\bar{\omega}_r}\boldsymbol{\rho}_{\rm ri}|f_2\rangle|f_1\rangle\langle f_2| + \langle f_1|\partial_{\bar{\omega}_r}\boldsymbol{\rho}_{\rm ri}|f_3\rangle|f_1\rangle\langle f_3|\Bigg]\end{aligned} \tag{B.281}$$

The first term is

$$\langle f_1|\partial_{\bar{\omega}_r}\boldsymbol{\rho}_{\rm ri}|f_1\rangle = \langle\psi_{\rm ri}|[(\partial_{\bar{\omega}_r}|\psi_{\rm ri}\rangle)\langle\psi_{\rm ri}| + |\psi_{\rm ri}\rangle(\partial_{\bar{\omega}_r}\langle\psi_{\rm ri}|)]|\psi_{\rm ri}\rangle = \langle\psi_{\rm ri}|\partial_{\bar{\omega}_r}\psi_{\rm ri}\rangle + \langle\partial_{\bar{\omega}_r}\psi_{\rm ri}|\psi_{\rm ri}\rangle \tag{B.282}$$

In this equation, the first and second elements are a complex conjugate pair. The first element is

$$\begin{aligned}\langle\psi_{\rm ri}|\partial_{\bar{\omega}_r}\psi_{\rm ri}\rangle &= \left[\int\int\psi_{\rm ri}(t_r,t_i)^*\langle t_r|_r\langle t_i|_i\,dt_r dt_i\right]\left[\int\int[-i(t_r-\bar{t}_r)]\psi_{\rm ri}(t_r',t_i')|t_r'\rangle_r|t_i'\rangle\,dt_r' dt_i'\right] \\ &= \int\int[-i(t_r-\bar{t}_r)]|\psi_{\rm ri}(t_r,t_i)|^2 dt_r dt_i \\ &= 0\end{aligned} \tag{B.283}$$

The second term is

$$\begin{aligned}\langle f_2|\partial_{\bar{\omega}_r}\boldsymbol{\rho}_{\mathrm{ri}}|f_1\rangle &= \langle f_2|[(\partial_{\bar{\omega}_r}|\psi_{\mathrm{ri}}\rangle)\langle\psi_{\mathrm{ri}}| + |\psi_{\mathrm{ri}}\rangle(\partial_{\bar{\omega}_r}\langle\psi_{\mathrm{ri}}|)]|\psi_{\mathrm{ri}}\rangle = \langle f_2|\partial_{\bar{\omega}_r}\psi_{\mathrm{ri}}\rangle + \langle f_2|\psi_{\mathrm{ri}}\rangle\langle\partial_{\bar{\omega}_r}\psi_{\mathrm{ri}}|\psi_{\mathrm{ri}}\rangle \\ &= \langle f_2|\partial_{\bar{\omega}_r}\psi_{\mathrm{ri}}\rangle \end{aligned} \tag{B.284}$$

$$\begin{aligned}\langle f_2|\partial_{\bar{\omega}_r}\psi_{\mathrm{ri}}\rangle &= \int\int\sqrt{2(1-\kappa)}[\sigma_r(t_r-\bar{t}_r)+\sigma_i(t_i-\bar{t}_i)]\psi_{ri}(t_r,t_i)\langle t_r|_r\langle t_i|\,dt_r dt_i \\ &\cdot\int\int[-i(t_r-\bar{t}_r)]\psi_{\mathrm{ri}}(t'_r,t'_i)\,|t'_r\rangle_r|t'_i\rangle\,dt'_r dt'_i \\ &= \int\int\sqrt{2(1-\kappa)}[\sigma_r(t_r-\bar{t}_r)+\sigma_i(t_i-\bar{t}_i)][-i(t_r-\bar{t}_r)]|\psi_{\mathrm{ri}}(t_r,t_i)|^2 dt_r dt_i \\ &= \int\int-i\sqrt{2(1-\kappa)}[\sigma_r(t_r-\bar{t}_r)^2+\sigma_i(t_i-\bar{t}_i)(t_r-\bar{t}_r)]|\psi_{\mathrm{ri}}(t_r,t_i)|^2 dt_r dt_i \\ &= \frac{i}{\sigma_r\sqrt{2(1-\kappa)}}\end{aligned} \tag{B.285}$$

Replacing $t_r-\bar{t}_r$ with t_r and $t_i-\bar{t}_i$ with t_i gives

$$\begin{aligned}\langle f_2|\partial_{\bar{\omega}_r}\psi_{\mathrm{ri}}\rangle &= \frac{4(1-\kappa^2)\sigma_r^2\sigma_i^2}{\pi^2}\int\int-i\sqrt{2(1-\kappa)}[\sigma_r t_r^2+\sigma_i t_i t_r]\exp[-2\sigma_s^2 t_r^2-2\sigma_i^2 t_i^2+4\kappa\sigma_r\sigma_i t_r t_i]dt_r dt_i \\ &= \frac{-i4(1-\kappa^2)\sqrt{1-\kappa}\sigma_r^2\sigma_i^2}{\pi^2}\int\int[\sigma_r t_r^2+\sigma_i t_i t_r]\exp[-2(1-\kappa^2)\sigma_r^2 t_r^2-2(\sigma_i t_i-\kappa\sigma_r t_r)^2]dt_r d\end{aligned} \tag{B.286}$$

Replacing $\sigma_i t_i-\kappa\sigma_r t_r$ with t'_i gives

$$\frac{dt'_i}{dt_i}=\sigma_i, t_i=\frac{t'_i+\kappa\sigma_r t_r}{\sigma_i}$$

Then, the integral becomes

$$\begin{aligned}
\langle f_2|\partial_{\bar{\omega}_r}\psi_{\text{ri}}\rangle &= \frac{1}{\sigma_i}\frac{-i4\sqrt{1-\kappa^2}\sqrt{1-\kappa}\sigma_r\sigma_i}{\pi}\int\int[\sigma_r t_r^2+(t_i'+\kappa\sigma_r t_r)t_r]\exp[-2(1-\kappa^2)\sigma_r^2t_r^2-2t_i'^2]dt_r dt_i' \\
&= \frac{-i4(1-\kappa)\sqrt{1+\kappa}\sigma_r}{\pi}\int\int[(1+\kappa)\sigma_r t_r^2+t_i't_r]\exp[-2(1-\kappa^2)\sigma_r^2t_r^2-2t_i'^2]dt_r dt_i' \\
&= \frac{-i4(1-\kappa)\sqrt{1+\kappa}\sigma_r}{\pi}\int\int(1+\kappa)\sigma_r t_r^2\exp[-2(1-\kappa^2)\sigma_r^2t_r^2-2t_i'^2]dt_r dt_i' \\
&= \frac{-i4(1-\kappa^2)\sqrt{1+\kappa}\sigma_r}{\pi}\frac{\sqrt{\pi}}{\sqrt{2}}\int\sigma_r t_r^2\exp[-2(1-\kappa^2)\sigma_r^2t_r^2]dt_r \\
&= \frac{-i4(1-\kappa^2)\sqrt{1+\kappa}\sigma_r}{\pi}\frac{\sqrt{\pi}}{\sqrt{2}}\cdot\frac{\sqrt{\pi}\sigma_r}{4\sqrt{2}(1-\kappa^2)\sqrt{1-\kappa^2}\sigma_r^3} = \frac{i}{\sigma_r\sqrt{2(1-\kappa)}}
\end{aligned} \tag{B.287}$$

Applying the similar steps, other three elements can be obtained

$$\langle f_3|\partial_{\bar{\omega}_r}\boldsymbol{\rho}_{\text{ri}}|f_1\rangle = \frac{i}{\sigma_r\sqrt{2(1+\kappa)}} \tag{B.288a}$$

$$\langle f_1|\partial_{\bar{\omega}_r}\boldsymbol{\rho}_{\text{ri}}|f_2\rangle = -\frac{i}{\sigma_r\sqrt{2(1-\kappa)}} \tag{B.288b}$$

$$\langle f_1|\partial_{\bar{\omega}_r}\boldsymbol{\rho}_{\text{ri}}|f_3\rangle = -\frac{i}{\sigma_r\sqrt{2(1+\kappa)}} \tag{B.288c}$$

(B.288d)